# Improving Time-Domain Prediction of Vortex-Induced Vibration for Marine Risers

by

©Boyang Zhang, B.Eng.

A Thesis submitted to the School of Graduate Studies in partial fulfillment of the requirements for the degree of

**Master of Engineering**

**Faculty of Engineering and Applied Science**

Memorial University of Newfoundland

**October 2017**

St. John's                                                                 Newfoundland

# Abstract

As offshore exploration and production is moving into deepwaters, the prediction of the Vortex-Induced Vibration (VIV) of marine risers becomes a critical issue in the design process. VIV can lead to a reduced fatigue life and even the structural failure of the riser. Currently, frequency-domain models are widely used in the offshore industry to predict riser VIV. However, the nonlinearities encountered in complex deepwater environments make linear approaches unreliable. In contrast, time-domain models can capture the nonlinearities in a straightforward manner.

In this thesis, a time-domain model was further developed to predict the VIV of both rigid and flexible risers. Through a zero up-crossing analysis of the cross-flow displacement, the two state variables, amplitude-to-diameter ratio and reduced velocity, were determined to interpolate the database of hydrodynamic coefficients obtained from forced oscillation tests at high Reynolds numbers. The hydrodynamic forces were then calculated and incorporated into an enhanced global-coordinate-based finite element method program, MAPS-Mooring, to investigate riser behaviours in the time domain.

The enhanced program, MAPS-Mooring, comprises a two-stage computation: the riser profile under static equilibrium is first obtained based on a Newton iterative method, and the dynamic profile and tension of the riser are then solved by the second-order semi-implicit Adams method in the time domain.

The enhanced program was first validated by using experimental results of mooring line tests in the literature to prove its reliability and robustness. Validation studies were then carried out to the enhanced time-domain VIV model for a rigid riser in a uniform flow and a flexible riser in a step current. Good agreement was observed between the numerical results and the experimental measurements.

# Acknowledgements

as the industrial internship opportunities during my studies.

Lastly, I wish to express my deepest gratitude to my parents for their love, understanding, and support, without which I would never accomplish this long journey.

# Table of Contents

# List of Tables

# List of Figures

# Nomenclature

**Abbreviations**

| | |
|---|---|
| 1-DOF | One-degree-of-freedom |
| 2-D | Two-dimensional |
| 2-DOF | Two-degrees-of-freedom |
| 2S | Two single vortex are formed in one vortex-shedding cycle |
| 2P | Two pairs of vortices are formed in one vortex-shedding cycle |
| 3-D | Three-dimensional |
| CFD | Computational fluid dynamics |
| FEM | Finite element method |
| JIP | Joint industry project |
| LHS | Left-hand-side |
| m | Meter (the unit of length) |
| m/s | Meter per second (the unit of both speed and velocity) |
| MARIN | Maritime Research Institute Netherlands |
| MIT | Massachusetts Institute of Technology |
| NURBS | Non-Uniform Rational B-Spline |
| OTRC | Offshore Technology Research Center |
| $Re$ | Reynolds number |
| RHS | Right-hand-side |

| RMS | Root-mean-square |
|---|---|
| sec | Second (the unit of time) |
| SCR | Steel catenary riser |
| $S_G$ | Scruton number, also known as response parameter or stability parameter |
| $St$ | Strouhal number |
| TDP | Touch-down point |
| TTR | Top-tensioned riser |
| TU Delft | Delft University of Technology |
| USNA | United States Naval Academy |
| VIV | Vortex-induced vibration |
| WEC | Wave energy converter |
| WIO | Wake-induced oscillation |

**Symbols**

| $A$ | Amplitude of vibration |
|---|---|
| $A_k$ | Interpolation function |
| $A_z$ | Cross-flow motion amplitude |
| $A^*$ | Cross-flow amplitude ratio |
| **B** | Buoyancy force per unit length of a slender rod |
| $C_A$ | Added mass per unit length |
| $C_d$ | In-line drag coefficient |
| $C_D$ | Drag force per unit length per unit normal velocity |
| $C_{d0}$ | Mean in-line drag coefficient |
| $C_{lv}$ | Cross-flow lift coefficient |

| | |
|---|---|
| $C_{lv0}$ | Initial guess of the cross-flow lift coefficient in numerical simulation |
| $C_m$ | Added mass coefficient |
| $C_M$ | Inertia force per unit length per unit normal acceleration |
| $C_{m0}$ | Initial guess of the added mass coefficient in numerical simulation |
| $C_V$ | Tolerance of the tangent velocity of a slender rod |
| $D$ | Diameter of the cylinder |
| $EA$ | Axial stiffness |
| $EI$ | Bending stiffness |
| $\hat{f}$ | Nondimensional oscillation frequency |
| $f_{nw}$ | Natural frequency in still water |
| $f_{osc}$ | Oscillation frequency |
| $f_{vs}$ | Vortex-shedding frequency |
| $\mathbf{F}$ | Resultant force acting on a slender rod |
| $\mathbf{F}^d$ | Hydrodynamic load per unit length |
| $F_D$ | In-line drag force amplitude |
| $F_{D0}$ | Mean in-line drag force |
| $F_L$ | Cross-flow lift force amplitude |
| $\mathbf{F}^s$ | Hydrostatic load per unit length |
| $F_x$ | Total in-line drag force |
| $F_z$ | Total cross-flow lift force |
| $F_{\dot{z}}$ | Cross-flow lift force in phase with velocity |
| $F_{\ddot{z}}$ | Cross-flow lift force in phase with acceleration |
| $H$ | Torque |
| $L$ | Length of the cylinder |

| | |
|---|---|
| **m** | Applied moment per unit length on a slender rod |
| $m$ | Mass of the cylinder |
| $m'$ | Added mass of the cylinder |
| **M** | Resultant moment acting along the centerline of a slender rod |
| $k$ | Spring stiffness |
| $k_s$ | Surface roughness |
| $k_x$ | Structural stiffness in the in-line direction |
| $k_z$ | Structural stiffness in the cross-flow direction |
| $P_m$ | Interpolation function |
| $P_s$ | Hydrostatic pressure at rod position **r** |
| **q** | Applied force per unit length on a slender rod |
| $q^{spring}$ | Distributed spring support force of the sea bottom in the vertical direction |
| **r** | Position vector of a slender rod |
| **r'** | Unit tangent vector of a slender rod |
| **r''** | Principal normal vector of a slender rod |
| **r̈** | Acceleration vector of a slender rod |
| $\dot{\mathbf{r}}^n$ | The normal velocity of a slender rod |
| $\ddot{\mathbf{r}}^n$ | The normal acceleration of a slender rod |
| $r_i$ | Component of **r** in $i$th direction |
| $s$ | Arc length along a slender rod |
| $t$ | Time |
| $T$ | Tension in a slender rod |
| $\tilde{T}$ | Effective tension in a slender rod |
| $T_{app}$ | Apparent period of motion |
| $U$ | Incoming flow velocity |

| | |
|---|---|
| $U_{ik}$ | Coefficients in the interpolation function |
| $U^*$ | Nominal reduced velocity |
| $\mathbf{V}$ | Absolute velocity of water particles |
| $V$ | Relative normal velocity between the incoming current and the structure |
| $\dot{\mathbf{V}}$ | Absolute acceleration of water particles |
| $\dot{\mathbf{V}}^n$ | Fluid acceleration normal to the centerline of a slender rod |
| $\mathbf{V}^n_{rel}$ | Relative fluid velocity normal to the centerline of a slender rod |
| $V_r$ | Reduced velocity |
| $V_t$ | Tangent velocity of a slender rod |
| $V_{tow}$ | Carriage towing speed |
| $\mathbf{w}$ | Rod weight per unit length |
| $\tilde{\mathbf{w}}$ | Effective rod weight per unit length |
| $x$ | In-line displacement |
| $\ddot{x}$ | In-line acceleration |
| $z$ | Cross-flow displacement |
| $\dot{z}$ | Cross-flow velocity |
| $\ddot{z}$ | Cross-flow acceleration |
| $Z_{max}$ | Maximum transverse displacement in a motion cycle |
| $Z_{min}$ | Minimum transverse displacement in a motion cycle |
| $Z_{btm}$ | Vertical coordinate of the sea bottom in the global coordinate system |
| $\delta_{ij}$ | Kronecker delta function |
| $\Delta t$ | Incremental time step size |
| $\epsilon$ | Strain in a slender rod |
| $\zeta_s$ | Structural damping factor |

| | |
|---|---|
| $\kappa$ | Curvature of the centerline of a slender rod |
| $\lambda$ | Lagrangian multiplier |
| $\tilde{\lambda}_m$ | Coefficients in the interpolation function |
| $\mu_f$ | Dynamic friction coefficient of the sea bottom |
| $\nu$ | Kinematic viscosity |
| $\xi$ | Nondimensional arc length |
| $\pi$ | The ratio of a circle's circumference to its diameter |
| $\rho_f$ | Density of fluid |
| $\rho$ | Mass per unit length of a slender rod |
| $\sigma$ | Root-mean-square operator |
| $\omega$ | Cross-flow motion angular frequency |

# Chapter 1

# Introduction

## 1.1  Background

Offshore exploration and production activities are expanding into deepwater and ultra-deepwater regions. It is important to design marine risers for safe and reliable operations in these complex ocean environments.

Marine risers connect the sea surface structures and the sea bottom wellheads. Subjected to an ocean current, a riser undergoes vibration caused by vortex shedding from both sides of its cylindrical surface. This nonlinear, near-periodic vibration, termed as *vortex-induced vibration* (VIV), leads to an increased drag load on and a reduced fatigue life of the riser. If the vortex-shedding frequency is in the proximity of the riser's natural frequencies, the riser will vibrate at an amplitude comparable to the riser diameter. This phenomenon is known as *lock-in*, and it will become even more difficult to be predicted when the riser is operating in the deepwater and ultra-deepwater environments, where the incoming current varies both spatially and temporally along the riser span. If multiple risers are operating in sufficient vicinity, VIV interaction and wake-induced oscillations (WIO) would occur, resulting in

clashing and even structural failure of adjacent risers.

A background introduction to the VIV of marine risers is presented in the following sections.

### 1.1.1 Marine Risers

Following the classification of Chakrabarti (2005), marine risers can be categorized into four groups pertaining to functionality: drilling riser, production riser, import riser, and export riser. They are used for drilling or producing individual wells or for importing and exporting well stream products.

Based on whether they are dominated by tension or bending, risers can also be distinguished into rigid risers and flexible risers. The most common rigid risers are top-tensioned risers (TTRs), which are employed in moderate water depths. TTRs stand vertically in water columns with initial tensions applied at their connection joints to the surface vessel. The top end of a TTR is subject to the horizontal motion of the vessel. Therefore, the vessel connected with TTRs requires good station keeping ability. In addition, buoyancy modules can be installed along a TTR to reduce its self-weight.

On the other hand, flexible risers possess curved geometries and are dominated by bending. Steel catenary risers (SCRs) and free-hanging risers are two typical types of flexible risers. The riser curvature sustained by the self-weight, buoyancy, and environmental loads enables SCRs to withstand moderate vessel planar motions. However, as the water depth increases, the length and the associated cost of SCRs increase tremendously, and the increased self-weight of SCRs leads to a risk of structural failure. To tackle this issue, free-hanging risers are introduced with buoyancy modules or buoys attached at the intermediate spans. The wave-shaped configurations can compensate large vessel motions as well as the frequent soil-structure contact near the touch-down

point (TDP). Though requiring less material, free-hanging risers require higher costs for fabrication and installation. A schematic of different free-hanging riser types is illustrated in Figure 1.1.
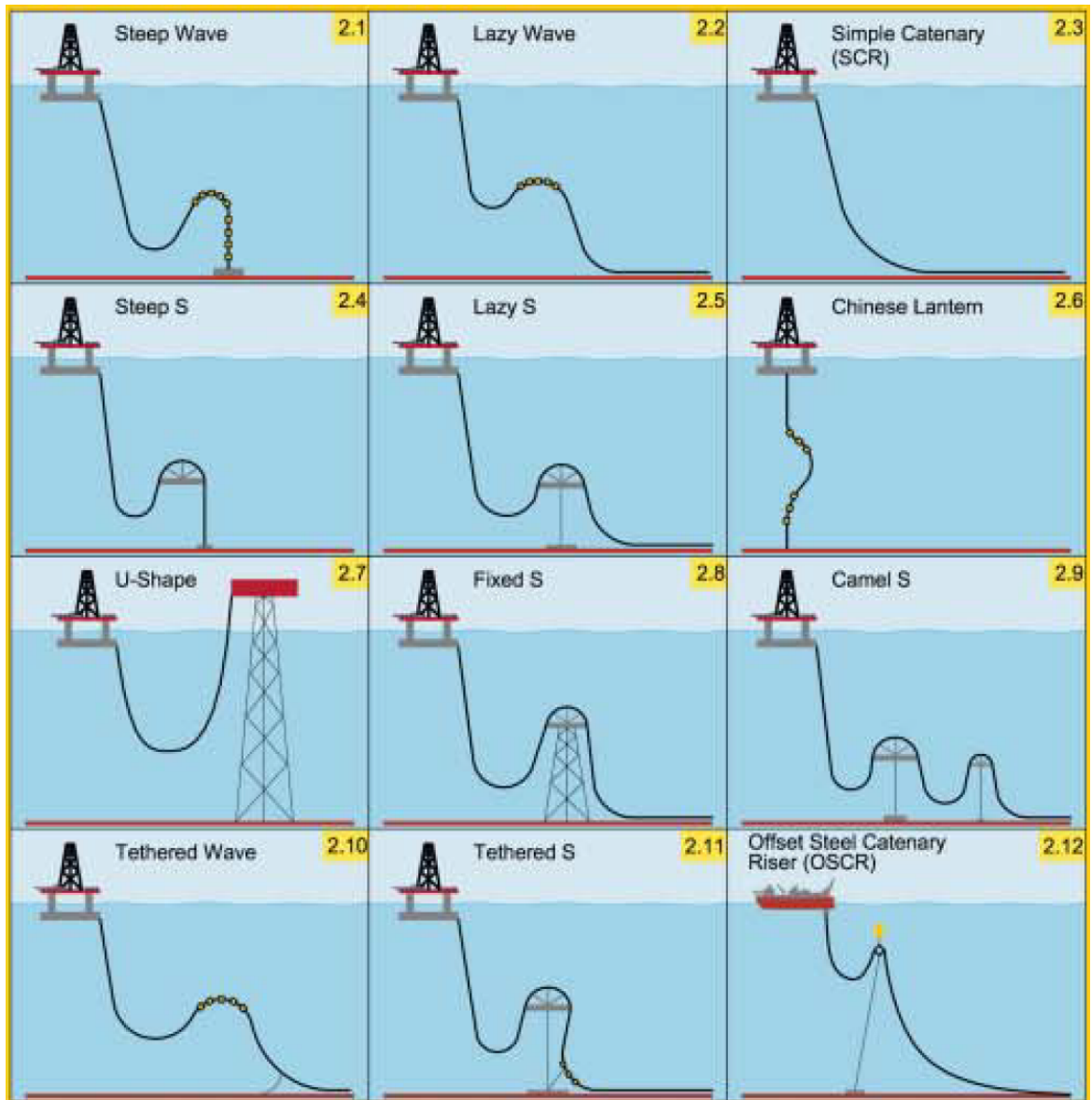


Figure 1.1: Configurations of free-hanging risers (from Shu et al. (2010))

## 1.1.2 Flow Regimes for A Stationary Cylinder in Steady Current

One of the most important dimensionless parameters in describing flow behaviour is the *Reynolds number*, which measures the ratio of inertia forces to friction forces in a flow. The Reynolds number ($Re$) is defined as:

$$Re = \frac{UD}{\nu} \qquad (1.1)$$

where $U$ is the velocity of the incoming flow, $D$ is the characteristic length of the bluff body, and $\nu$ is the kinematic viscosity.

Figure 1.2 illustrates different patterns of a steady and uniform flow around a fixed, smooth, and circular cylinder as the $Re$ increases. The flow regimes are classified with respect to $Re$ according to the work of Sumer and Fredsøe (1997).

The flow around the cylinder is symmetric and no separation occurs near the aft body when $Re \lessapprox 5$ (Figure 1.2a).

As $Re$ increases, the streamlines begin to separate from the body surface and the separation points approach the fore stagnation point from its aft counterpart. Meanwhile, two still eddies are formed symmetrically in the near wake (Figure 1.2b). The span of the pair of vortices grows linearly with $Re$, until reaching a maximum length of approximately three cylinder diameters (Blevins, 1990).

In the regime, $40 \lessapprox Re \lessapprox 200$, the two laminar eddies no longer remain still and start to travel alternately downstream to the far wake (Figure 1.2c). This asymmetric, repeating vortical structure is called *von Kármán vortex street*. No correlation along the cylinder axis is observed in this $Re$ regime.

As $Re$ further increases, the transition of laminar vortices to turbulence advances towards the cylinder from the far wake until the vortex street becomes completely
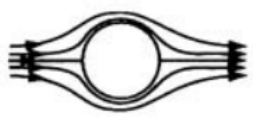
| | | |
|---|---|---|
| a) | No separation. Creeping flow | Re < 5 |
| b) | A fixed pair of symmetric vortices | 5 < Re < 40 |
| c) | Laminar vortex street | 40 < Re < 200 |
| d) | Transition to turbulence in the wake | 200 < Re < 300 |
| e) | Wake completely turbulent. A: Laminar boundary layer separation | $300 < Re < 3 \times 10^5$ Subcritical |
| f) | A: Laminar boundary layer separation B: Turbulent boundary layer separation; but boundary layer laminar | $3 \times 10^5 < Re < 3.5 \times 10^5$ Critical (Lower transition) |
| g) | B: Turbulent boundary layer separation; the boundary layer partly laminar partly turbulent | $3.5 \times 10^5 < Re < 1.5 \times 10^6$ Supercritical |
| h) | C: Boundary layer completely turbulent at one side | $1.5 \times 10^6 < Re < 4 \times 10^6$ Upper transition |
| i) | C: Boundary layer completely turbulent at two sides | $4 \times 10^6 < Re$ Transcritical |
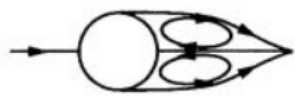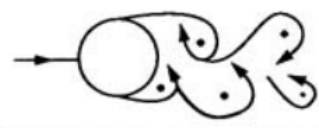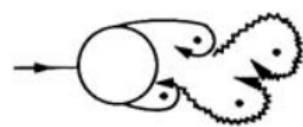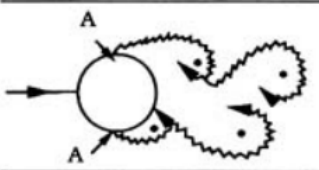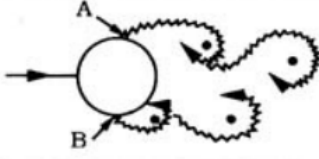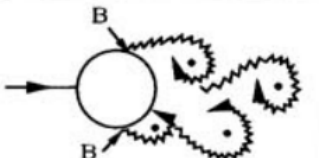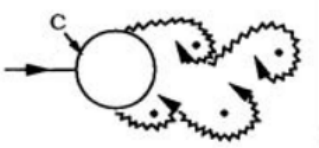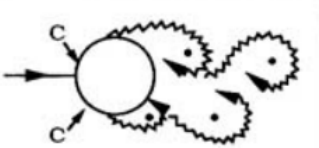
Figure 1.2: Regimes of flow around a smooth, circular cylinder in steady current (from Sumer and Fredsøe (1997))

turbulent, when $Re \approx 300$ (Figure 1.2d).

The vortex shedding of the fully-developed turbulent wake remains stable over a large range of $300 \lesssim Re \lesssim 3 \times 10^5$. Meanwhile, no turbulence is observed before the separation point on the cylinder surface (Figure 1.2e). This regime is known as the *subcritical Re* regime, marked by a strong and periodic vortex shedding.

The laminar shear layer starts transiting to turbulence at one side of the cylinder surface at approximately $3 \times 10^5 < Re < 3.5 \times 10^5$ (Figure 1.2f). This $Re$ regime is named the *critical* flow regime. In this regime, the wake reduces in width, accompanied by a disorganized vortex street. The asymmetric flow about the cylinder results in a non-zero mean force exerting in the cross-flow direction.

As the flow enters the *supercritical* regime where $3.5 \times 10^5 \lesssim Re \lesssim 1.5 \times 10^6$, vortex shedding resumes in an organized manner. The shear layer becomes turbulent after it is first shed from the body, and then re-attaches to the cylinder surface before finally being shed downstream. The boundary layer becomes a mixture of lamina and turbulence on both sides of the cylinder (Figure 1.2g).

With a further growth in $Re$ from approximately $1.5 \times 10^6$ to $4 \times 10^6$, the transition of laminar boundary layer into turbulence is only completed on one side of the cylinder surface (Figure 1.2h). This regime is called the *upper-transition* flow regime.

Finally, as $Re$ enters the *transcritical Re* regime where $Re \gtrsim 4 \times 10^6$, the whole cylinder is covered by turbulence and the flow separation points move towards the fore stagnation point (Figure 1.2i). The wake exhibits a more organized pattern with a near-periodic vortex shedding.

### 1.1.3 Vortex Shedding

The vortices are shed alternately from the surface of a stationary cylinder subject to an incoming flow at $Re \gtrsim 40$. This is termed the *vortex-shedding phenomenon.*

The phenomenon can be observed in multiple engineering applications, such as heat exchangers, bridges, tall buildings, marine cables, and offshore structures. For more than a century, tremendous research efforts have been made in unveiling its fundamental mechanisms as well as in predicting it.

An object subjected to a flow can be categorized as a *bluff body* or a *streamlined body* based on the flow separation on its surface. If the flow separation is profound on the aft body, the object is defined as a bluff body, for example, a circular cylinder; otherwise if the flow separation is marginal, then the body is said to have a streamlined shape, such as a hydrofoil. The following discussion focuses on vortices shed from a bluff body in a uniform fluid flow.

In a real fluid flow, the effect of viscosity is significant in the *boundary layer*, where the flow velocity increases from zero on a stationary body to the free stream velocity. Due to the dissipation of kinetic energy by the internal friction, the fluid particles cannot reach the aft stagnation point and therefore separate from both sides of the cylinder surface, forming two free shear layers before the aft stagnation point. The two points where the fluid particles detach from the body are named the *separation points*.

After separating from one side of the cylinder surface, the eddy increases its strength by absorbing vortices in the free shear layer. When the eddy grows strong enough, it draws the free shear layer of the other side to cross the wake centerline. According to Gerrard (1966), the fluid particles in the shear layer attracted across the wake centerline can be trapped by the growing eddy, transported upstream along the opposite shear layer, or fed into the vortex formation region. The latter vortices will interrupt the circulation in the shear layer from being fed into the growing vortex, which is then shed and carried downstream by the flow.

Once the vortex detaches from the free shear layer, a new vortex will be sprouted

on the same side of the cylinder. Meanwhile, the vortices, transited upstream from the opposite side in the previous shedding process, will grow in size and strength to attract the newly germinated vortex to pass the wake centerline, resulting in the shedding of a vortex at the other side. This process will be repeated once a vortex departs from the free shear layer at one side of the cylinder, leading to an alternate and near-periodic vortex shedding phenomenon.

### 1.1.3.1  Vortex-Shedding Frequency

*Vortex-shedding frequency* is a measure of how fast the wake repeats its pattern in a vortex-shedding phenomenon. Strouhal (1878) first descried the linear proportionality between the vortex-shedding frequency $f_{vs}$ and $U/D$, where $U$ is the incoming flow velocity and $D$ is the characteristic length of the bluff body, when he studied a vibrating string in a wind tunnel test. The nondimensional vortex-shedding frequency named after him, the *Strouhal number* ($St$), is defined as:

$$St = \frac{f_{vs}D}{U} \tag{1.2}$$

$St$ can be affected by many aspects of the body and the flow, such as the surface roughness and the cross-sectional shape, the turbulence and shear in the incoming flow, and $Re$. For a given bluff body subject to a known flow, the $St$ is exclusively a function of $Re$. Figure 1.3 illustrates the $St$ for a fixed smooth circular cylinder in a low-turbulent uniform flow at different $Re$ regimes, while Figure 1.4 presents the power spectra corresponding to the dotted data (Schewe, 1983) plotted in Figure 1.3.

The vortex shedding first occurs at $Re \approx 40$, where $St \approx 0.1$. $St$ reaches to around 0.2 as $Re$ increases from approximately 40 to 300. Over the entire subcritical regime, $300 \lesssim Re \lesssim 3 \times 10^5$, $St$ is roughly constant with an approximate value of

0.18 with a steady vortex street, which is evidenced by the narrow-band spectrum in Figure 1.4a.
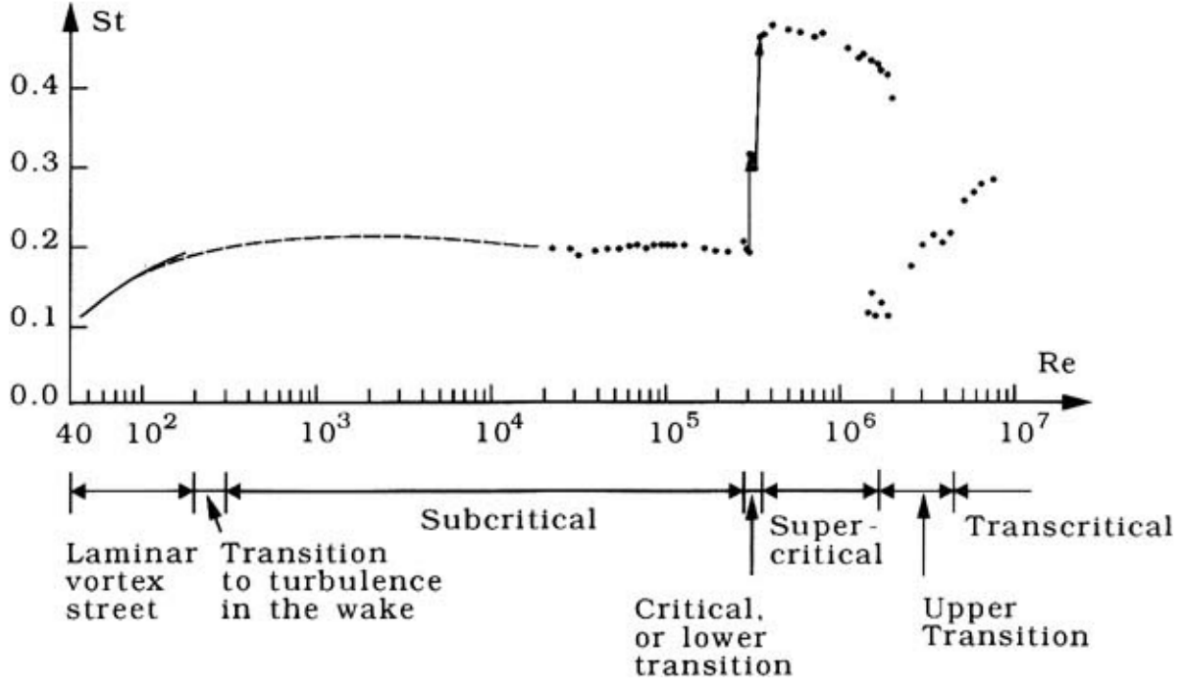


Figure 1.3: Strouhal number for a smooth circular cylinder at different Reynolds regimes (from Sumer and Fredsøe (1997))

When the flow enters the critical regime, $3 \times 10^5 \lesssim Re \lesssim 3.5 \times 10^5$, $St$ jumps from 0.18 to about 0.46 and then gradually reduces to around 0.4 through the supercritical regime, $3.5 \times 10^5 \lesssim Re \lesssim 1.5 \times 10^6$. At the critical and supercritical regimes, the reattachment of the flow takes place beyond the turbulent boundary layer separation at either one or both sides of the cylinder surface, respectively. This results in a smaller distance between the two separation points and therefore a faster interaction between two boundary layers than those at subcritical regime, accounting for the rise of $St$ at such flow regimes.

The power spectrum at the supercritical flow regime (Figure 1.4b) is dominated at a preponderant climax in a narrow band, implying a structured vortex street.

Another distinctive feature of the power spectrum at this regime is the considerable abatement in the lift fluctuations, suggesting a weaker eddy strength than that in subcritical regime.

As $Re$ steps into the upper transition regime, $1.5 \times 10^6 \lesssim Re \lesssim 4 \times 10^6$, the boundary layer becomes fully turbulent on one side and with a combination of lamina and turbulence on the other side of the cylinder surface, generating the *lee-wake vortices*. As a consequence, the two boundary layers are suppressed from interacting with each other and lead to a chaotic vortex street, which can be inferred from the broad-band power spectra at this regime (Figure 1.4c-d).

The repeating vortex street recurs with an approximate $St$ of $0.25 \sim 0.30$ as $Re$ is further increased into the transcritical regime, $Re \gtrsim 4 \times 10^6$, as evidenced from the peak values in the power spectra (Figure 1.4e-f).
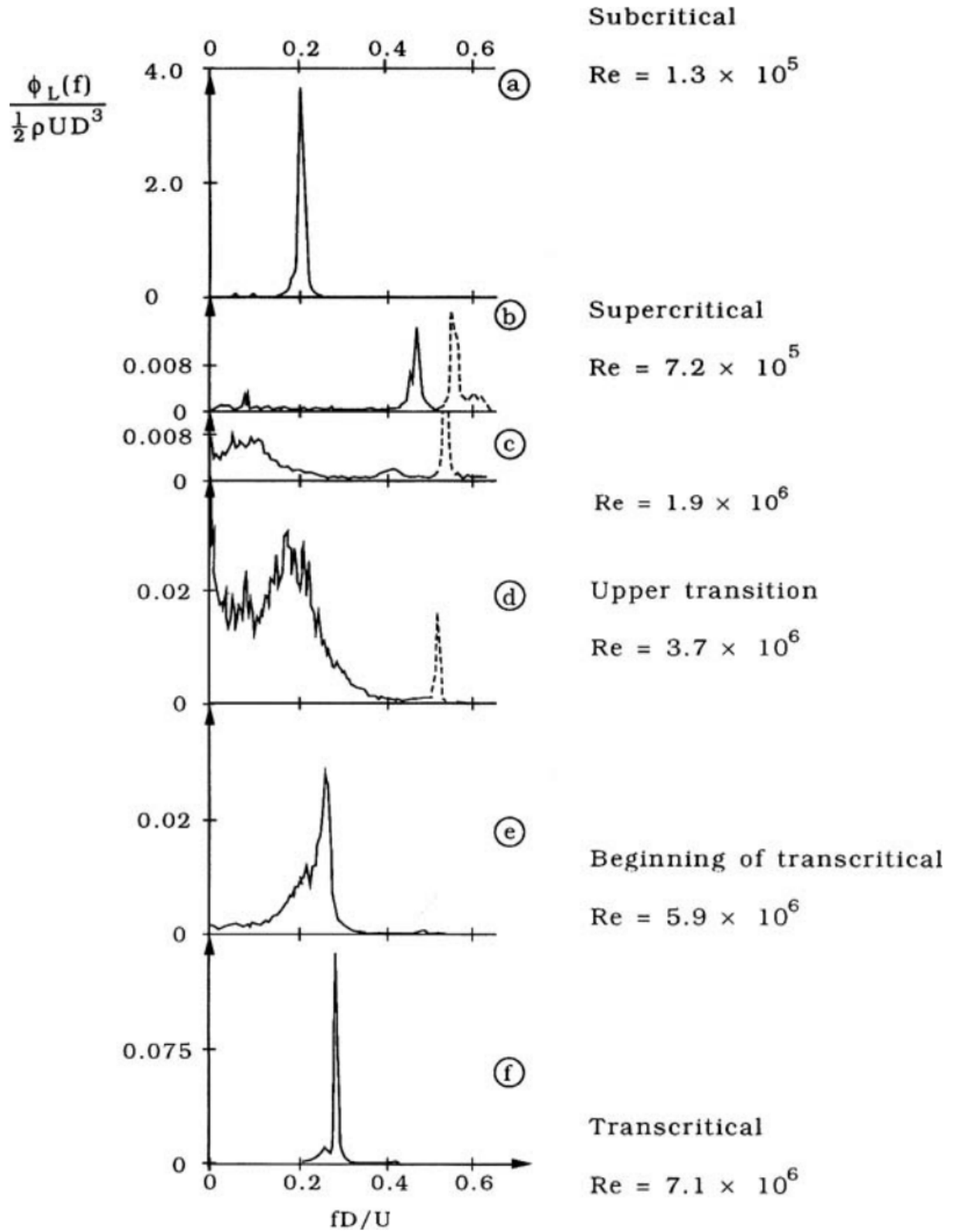
Figure 1.4: Power spectra of the lift oscillations corresponding to the dots in Figure 1.3 (from Sumer and Fredsøe (1997))

### 1.1.4 Vortex-Induced Vibration

If the cylinder subject to a steady current is either elastically supported or flexible, it may be excited by the oscillating force imposed by the periodic vortex shedding. The resultant force can be decomposed into one component in-line with the flow direction and the other one transverse to the flow direction, namely the drag and lift forces, respectively. The lift force oscillates around zero at the vortex-shedding frequency, while the drag force oscillates around a non-zero mean value at a frequency twice the lift force frequency.

The *reduced velocity* describes the ratio of the wave length per cycle to the cylinder width, as defined by:

$$V_r = \frac{U}{f_{osc}D} \tag{1.3}$$

where $U$ is the incoming current speed, $f_{osc}$ is the cylinder oscillation frequency, and $D$ is the diameter.

Figure 1.5 illustrates typical responses of a circular cylinder vibrating under a steady current in the cross-flow direction.

The focus of the review as follows is on the cross-flow VIV. It starts at $V_r \approx 3$ and is governed by the vortex-shedding frequency. Within a range of $6 \lesssim V_r \lesssim 8$, the vortex-shedding frequency is synchronized to the cylinder vibration frequency, which approximates the natural frequency in still water. This phenomenon is named *lock-in*, also referred to as *synchronization*, *resonance*, or *wake capture* in the literature. When lock-in occurs, the VIV amplitude reaches its maximum value, which is usually one diameter. As the reduced velocity is further increased, the vortex-shedding frequency resumes the Strouhal linear relationship and more hydrodynamic damping is introduced into the system, accounting for the self-limited nature of VIV. Furthermore, the cylinder unlocks the still water natural frequency and vibrates at the vortex-shedding
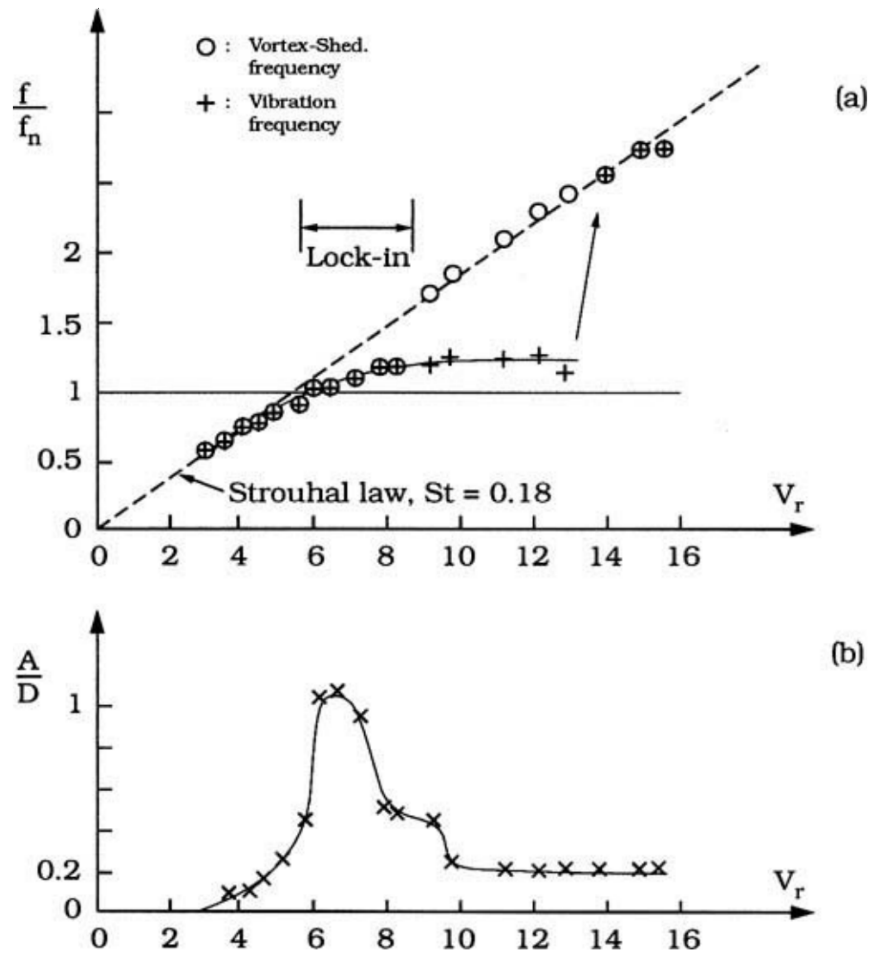
Figure 1.5: Cross-flow response of an elastically-supported circular cylinder subject to steady current in water, $(m/\rho_f D^2) = 5.3$. (from Anand (1985))

frequency at $V_r \gtrapprox 14$.

In VIV, continuous interaction between cylinder oscillation and vortex shedding occurs, resulting in a self-excited-self-limited process. As sketched in Figure 1.6, the vortices start to form when the cylinder travels upwards across the wake centerline for both 2S and 2P wake modes following the terminology introduced in Williamson and Roshko (1988). Therefore, it is reasonable to signal the start of a new VIV cycle when the cylinder crosses up its static equilibrium position. This is later reflected in the formulation of the present VIV prediction model in Chapter 3.
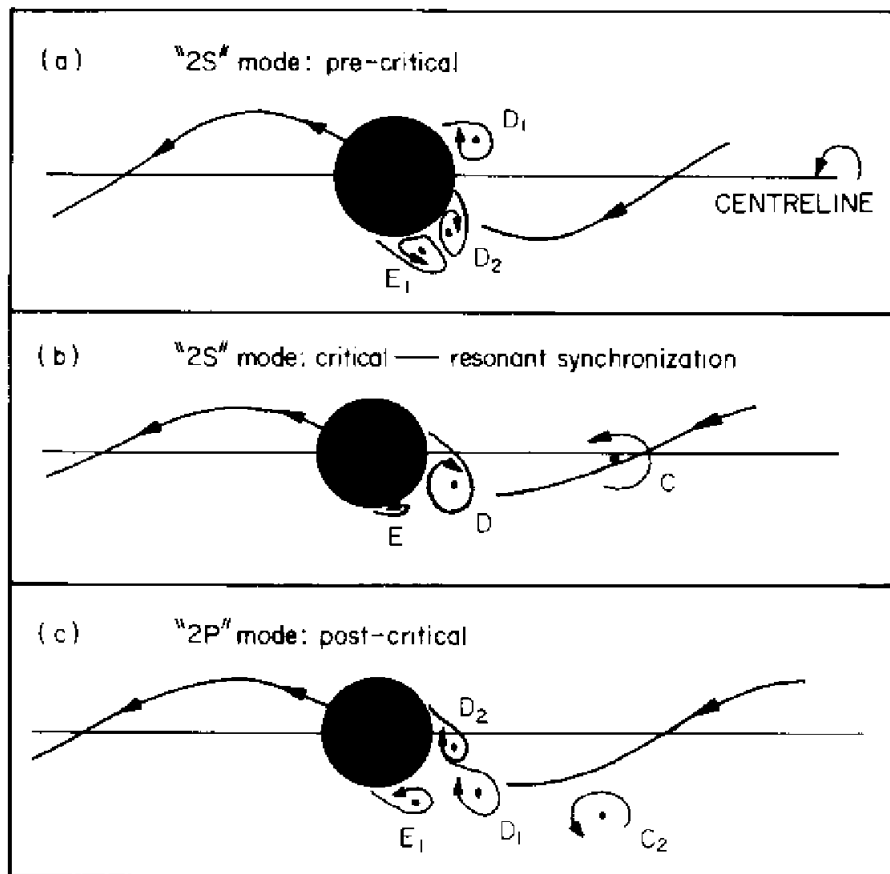


Figure 1.6: Positions of vortex "D" and other near-wake vortices when the cylinder is travelling upwards, and is just crossing the wake centerline; "2S" represents two single vortex are formed in one vortex-shedding cycle, while "2P" stands for two pairs of vortices are shed in one cycle (from Williamson and Roshko (1988))

### 1.1.5   Vortex-Induced Vibration Suppression

Based on its mechanisms, VIV may be suppressed in a number of ways. The most straightforward approach is to increase the reduced damping. The *reduced damping* $S_G$, also known as the *response parameter*, *stability parameter*, or *Scruton number* in the literature, is defined as:

$$S_G = \frac{2\,(m + m')(2\,\pi\,\zeta_s)}{\rho_f\,D^2} \tag{1.4}$$

where $m$ is the structural mass per unit length, $m'$ is the added mass per unit length, $\zeta_s$ is the structural damping factor, $D$ is the diameter, and $\rho_f$ is the fluid density.

An increased reduced damping can be achieved by increasing structural damping or structural mass. According to Blevins (1990), a reduced damping above 64 will minimize the peak VIV amplitude to less than 1% of the diameter. However, it is unlikely to achieve a reduced damping greater than 64 in deepwater and ultradeepwater applications. In addition, an increased structural mass may decrease the natural frequency, thus leading to a lower reduced velocity for the onset of lock-in.

VIV can also be mitigated by changing the structural stiffness or mass so that the natural frequencies are sufficiently away from the vortex-shedding frequency. In practice, this approach is usually employed on smaller structures where the highest vortex-shedding frequency is adjusted to be far less than the fundamental natural frequency. Therefore, the synchronization is avoided.

A third solution to subduing VIV is to fit additional devices to the cylinder. Figure 1.7 illustrates some devices currently adopted by the offshore industry for VIV suppression. These add-on devices can be grouped into two categories by suppression mechanism: one is to destroy the boundary layer on the structure surface (Figure 1.7a, b, c, f, h), and the other is to obstruct the interaction between the two shear layers

(Figure 1.7d, e, g).
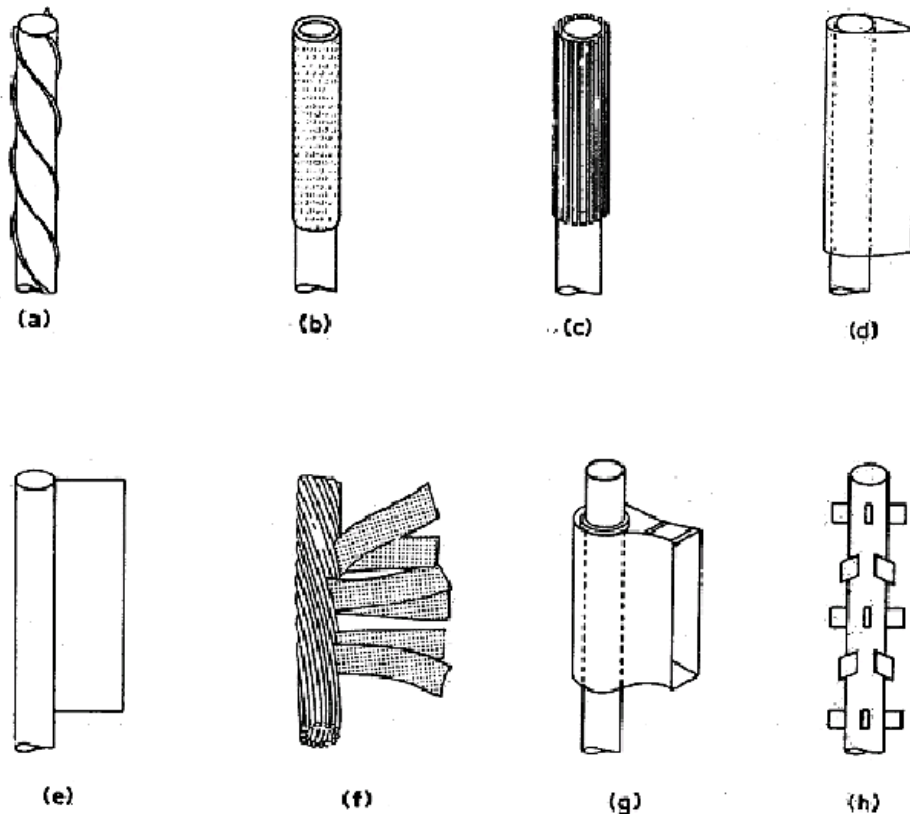


Figure 1.7: VIV suppression devices. (a) helical strakes, (b) perforated shroud, (c) axial slats, (d) streamlined fairing, (e) splitter plate, (f) ribbons, (g) guiding vane, (h) spoiler plates. (from Blevins (1990))

## 1.2   Thesis Outline

The objective of this thesis is the further development of a time-domain VIV prediction model for deepwater marine risers. A time-domain finite element program has been enhanced and validated by simulating the statics and dynamics of slender marine structures. The time-domain VIV prediction model has then been applied to predict the one-degree-of-freedom (1-DOF) VIV of a rigid cylinder and the VIV of a flexible riser model.

Chapter 2 presents a selective review of VIV prediction models as well as the forced and free vibration tests available in the literature.

Chapter 3 describes the enhanced time-domain VIV prediction model in detail. A description of the high-$Re$ hydrodynamic coefficient database, the rationale of the model, and the numerical scheme are discussed.

Chapter 4 and Chapter 5 present the validation results of the enhanced time-domain finite element program. The finite element scheme for mooring line analysis was first validated in Chapter 4, followed by the validation of the improved VIV prediction model in Chapter 5.

Chapter 6 draws the conclusions and some recommendations for future work.

Appendix A gives the detailed mathematical formulation and numerical procedure for the enhanced finite element program.

Bilinear surface interpolation scheme is presented in Appendix B.

# Chapter 2

# Literature Review

## 2.1 General

Numerical simulations and experimental approaches are the two dominant methods in predicting the VIV of marine risers. Experimental methods can reveal the flow and structure behaviours and provide benchmark data for numerical programs. However, experimental approaches are not widely used due to the facility limitations in lab-scale experiments and the intractable environmental factors in field tests.

The computational fluid dynamics (CFD) methods can solve the Navier-Stokes equation at different spatial scales, and could unveil the underlining physics of vortex shedding. However, due to its tremendous computational demand, CFD lacks applicability to industrial practice.

On the contrary, a reliable and robust semi-empirical model can effectively predict VIV under different scenarios by simply changing the input parameters. Currently, the numerical tools widely used by the offshore community for the VIV prediction of marine risers are semi-empirical frequency-domain models, such as SHEAR7 (Vandiver and Li, 1994), VIVA (Triantafyllou et al., 1999), and VIVANA (Larsen, 2000).

Modal analysis was employed in these models to determine the modes likely subject to VIV and the corresponding natural frequencies. For each mode, the reduced velocity is computed based on frequency and flow information. An excitation or damping force is then applied depending on the reduced velocity. Figure 2.1 presents a typical damping model used in SHEAR7 (Venugopal, 1996) where the damping is only defined for reduced velocities lower than 5 and greater than 8. For reduced velocities between 5 and 8, excitation was assumed to occur and a separate model was implemented.
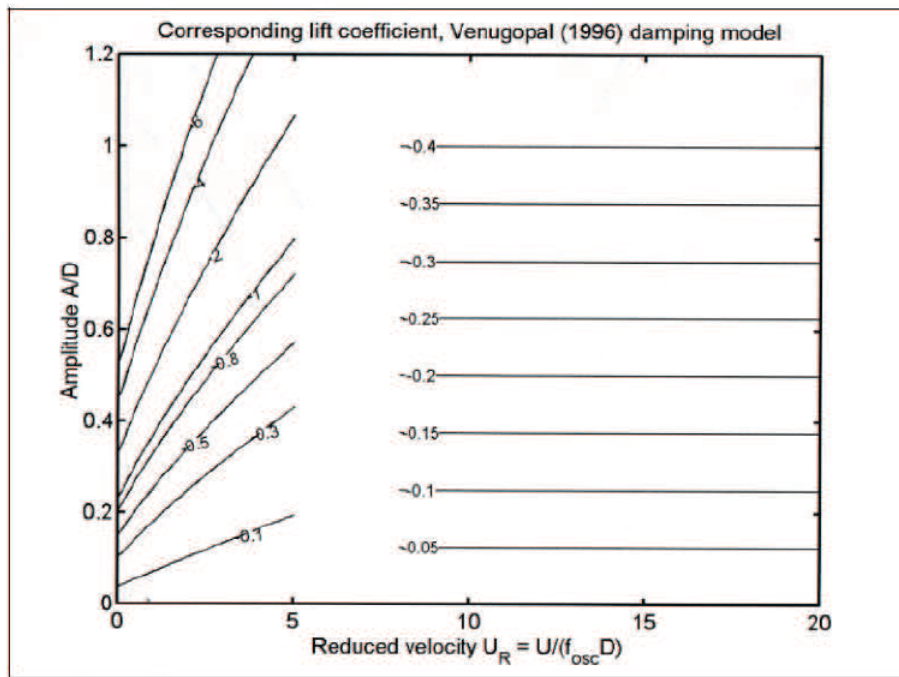


Figure 2.1: Damping model at low and high reduced velocities used in SHEAR7 (from Venugopal (1996))

There are however limitations in the frequency-domain models. They are inadequate to deal with nonlinearities such as temporally and spatially varying currents, dynamic boundary conditions and the coupled in-line and cross-flow VIV. Furthermore, positive and negative lift coefficients coexist in the lock-in region, as shown in the work of Gopalkrishnan (1993) and Oakley and Spencer (2004). This indicates

that hydrodynamic excitation and damping may not be independently considered. Being able to address the aforementioned weaknesses imposed by the frequency-domain methods, time-domain formulations are gaining more popularity in research and development.

Figure 2.2 categorizes the VIV numerical prediction models currently used by industry and researchers. A selective literature review of different semi-empirical VIV prediction approaches is given in the next section.
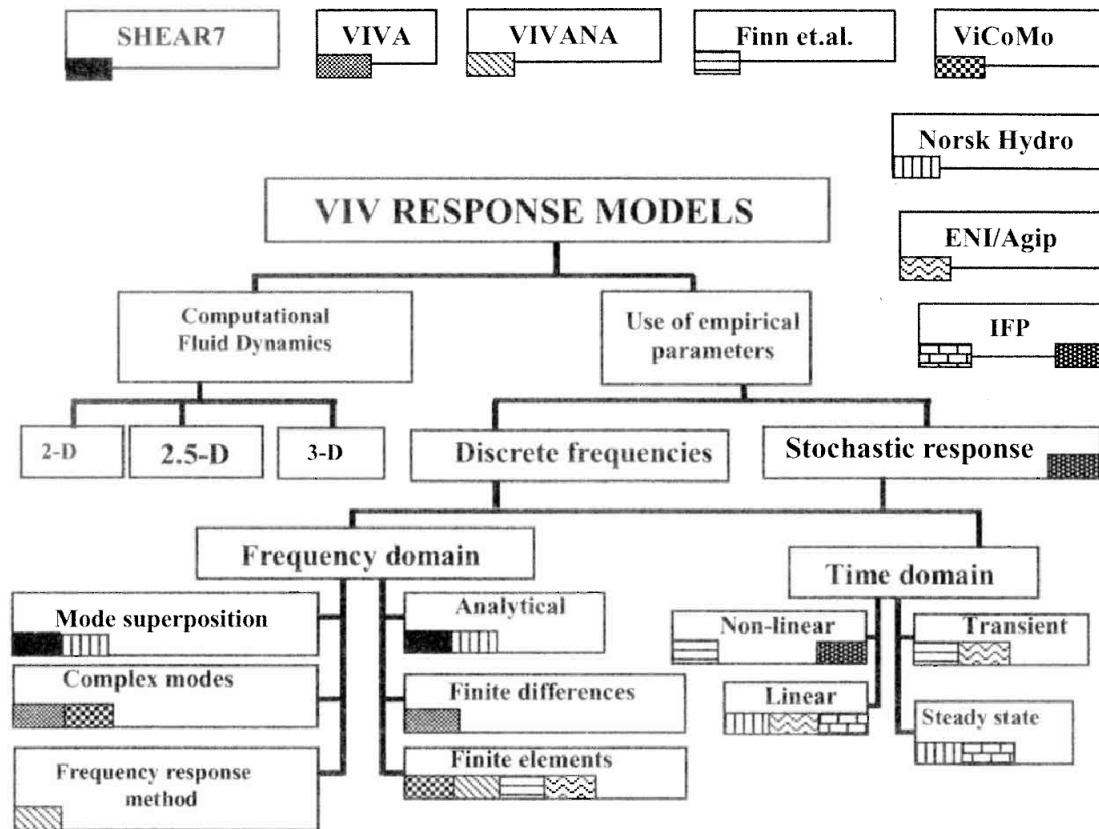


Figure 2.2: Classification of VIV prediction models (from Larsen (2000))

## 2.2 Semi-Empirical VIV Prediction Models

### 2.2.1 Frequency-Domain Models

SHEAR7 (Vandiver and Li, 1994) is a modal superposition frequency-domain program that is currently widely used in the offshore industry for the VIV prediction of marine risers. The lock-in condition is identified by exciting the modes within a predefined power-in region given the flow and structure information. A uniform distribution of the lift force coefficient along the span is employed in the power-in region. Two independent models were assumed for the in-line and cross-flow VIV (Venugopal, 1996).

VIVA models a riser as a tensioned beam and adopts a two-dimensional (2-D) analysis procedure in the frequency domain (Triantafyllou, 1998). The structure motion was linearized based on the assumption that the cross-flow VIV motion is small compared to the total length, while the oscillation frequency and the mode shape remain nonlinear throughout the solution phase of the eigenvalue problem in the frequency domain (Triantafyllou et al., 1999). The forced oscillation tests conducted by Gopalkrishnan (1993) and Dahl (2008) provided the hydrodynamic coefficient databases used in VIVA.

VIVANA (Larsen, 2000) analyzes the statics and dynamics of risers based on a frequency-domain forcing model incorporated with a three-dimensional (3-D) finite element program, RIFLEX (Fylling et al., 1995). The initial eigenfrequencies of the riser in still water were first calculated, and the excitation regions were then determined by comparing the modal frequencies to a predefined lock-in frequency range. The computation was completed by an iterative procedure based on a spanwise-varying added mass coefficient, which is a function of the nondimensional vibration frequency.

### 2.2.2 Time-Domain Numerical Schemes

Lie (1995) developed a finite element model in the time domain to simulate the transverse VIV of a flexible cylinder in a shear flow. The lift forces were approximated by two components, one at the cylinder motion frequency and one at the Strouhal frequency for a stationary cylinder. The cylinder frequency force was obtained from the experimental results of a cylinder with forced harmonic motions. The latter component was assumed to be less important than the cylinder frequency component and was modeled as a sinusoidal lift force by using the lift coefficient from the experimental data for a stationary cylinder.

Finn et al. (1999) developed a time-domain forcing algorithm to model both in-line and cross-flow VIV. The model decomposed the hydrodynamic force on a riser into one in-line component and one cross-flow component. The former component was further decomposed into one drag force and one inertia force, while the latter component was further decomposed into one drag force, one inertia force, and one lift force. The cross-flow lift force, giving rise to VIV, was approximated by a sinusoidal function with time-varying frequency, phase, and amplitude. The onsets of lock-in were determined by three nondimensional parameters, i.e., the ratio of the VIV amplitude to the riser diameter, the ratio of the natural frequency of a particular mode to the shedding frequency, and the ratio of transverse vibration frequency to the shedding frequency. The riser responses were computed with a finite element program, ABAQUS, and a user subroutine in ABAQUS was developed to calculate hydrodynamic forces using riser displacements, velocities and accelerations.

In the work of Finn et al. (1999), the in-line hydrodynamic force was formulated in an expression similar to Morison's equation (Morison et al., 1950). The dependence of the in-line drag on its frequency and the influence of varying reduced velocity were neglected. By adopting the algorithm of Finn et al. (1999) for cross-flow VIV

prediction, Sidarta et al. (2010) proposed a new in-line VIV forcing function and incorporated it into ABAQUS. The enhanced program was named SimVIV, which predicted in-line VIV in three regions: the first instability region, the second instability region, and the coupled in-line and cross-flow VIV region. In the third region, the in-line drag frequency was assumed to be twice the Strouhal frequency. The in-line drag coefficients were obtained from the forced oscillation tests in pure in-line direction and varied in term of amplitude ratio and reduced velocity. These two variables were determined by Prony's method, an exponential modelling technique. A constant added mass coefficient of 1.0 and no in-line mean drag due to current effect were assumed in both the work of Finn et al. (1999) and SimVIV.

Thorsen et al. (2014) proposed a phase synchronization model to predict the the cross-flow VIV in the time domain. The total hydrodynamic force acting on a cylinder was decomposed into three components: lift, damping, and added mass. The experimental excitation coefficient, incorporating both lift and damping, was smoothed to allow only one local maximum value. It was assumed that the excitation coefficient peaked when the phases of lift force and cross-flow velocity synchronized. The initial value and the rate of change of the lift force were used to calculate the instantaneous lift phase. The phase portrait of the time series for the past five Strouhal periods was used to compute the instantaneous phase of the cross-flow velocity. The damping model (Venugopal, 1996) was rewritten to avoid the dependence of the damping coefficient on the oscillation frequency. The revised damping model dissipated approximately the same amount of energy in each cycle to that dissipated by the original model. The phases of lift force and cross-flow velocity at each time step always tended to be synchronized.

Xue et al. (2015) predicted the coupled in-line and cross-flow VIV of marine risers in the time domain. The excitation forces in both directions comprised one compo-

nent in phase with velocity and one in phase with acceleration, respectively. The in-line drag was assumed to be excited at two different regions: the drag fluctuated in a frequency triple that of the Strouhal frequency in the first region, and in a frequency twice that of the Strouhal frequency in the second region. The transverse oscillation frequency was assumed to dominate the cross-flow lift, while the in-line drag frequencies were assumed to be dominated by either natural frequencies or oscillation frequencies. The experimental hydrodynamic coefficients collected from forced vibration tests in pure in-line and pure cross-flow directions were utilized to calculate the excitation forces. The coupling between the two-degrees-of-freedom (2-DOF) VIV was achieved by multiplying the in-line force with a factor, which depended on the transverse amplitude ratio. The mean drag coefficient was excluded in the calculation of the total in-line drag force. The damping model (Venugopal, 1996) was used to approximate the hydrodynamic regions not covered by the experimental data.

Most of the semi-empirical VIV prediction tools formulate VIV loads in a form similar to the Morison's equation and identify hydrodynamic coefficients in terms of dimensionless amplitude and reduced velocity. Mainçon (2011), however, predicted VIV in the time domain by a Wiener-Laguerre model based on strip theory. In this model, the cylinder diameter, fluid density, and kinematic viscosity were chosen as the baseline parameters to scale all the physical quantities. The recent histories of the relative velocity between the cylinder and the undisturbed fluid, defined as "tachogram", were thus scaled into a classic $Re$ expression but distinguished by an instant, local, and relative feature. The fundamental hypothesis of this model was that the "tachogram" alone determined the fluid force. The scaled "tachogram" was estimated by Laguerre polynomials, the coefficients of which were interpolated into a neural network to obtain the hydrodynamic forces on each Gauss point at each time step. These forces were then scaled back to real dimensions and implemented

into a time-domain finite element analysis, where the Newmark-$\beta$ method and Gauss quadrature were employed. The influence of varying the recent time history of velocity on the present force calculation required further investigations.

## 2.3 Forced and Free Cross-Flow VIV Tests

The current industry practice of predicting riser VIV is to make use of the hydrodynamic coefficients obtained from forced vibration tests along with different forcing models. Some experimental results are available at the online *MIT VIV Data Repository* (MIT, 2007). These databases contain lift coefficients, in-line drag coefficients, and added-mass coefficients obtained at different amplitude ratio and reduced velocity. A question remains on how to utilize the hydrodynamic information obtained from forced vibration tests to predict the free vibrations. In addition, most databases available in the literature were conducted at subcritical *Re* regimes. The question is whether these coefficients can be effectively used to predict VIV at critical and supercritical *Re*.

VIV is highly sensitive to the changes on the *Re*, surface roughness, mass ratio, aspect ratio, correlation length, and other governing parameters. Due to the complex nature of VIV phenomena, it is almost impossible to reconstruct a universal database for use under different scenarios. The findings from some representative forced and free VIV tests in the literature are summarized below.

Gopalkrishnan (1993) carried out an extensive forced vibration campaign on a one-inch diameter cylinder under a constant towing speed 0.4 m/s (with $Re \approx 10^4$). The lift coefficients in terms of amplitude ratio and nondimensional oscillation frequency are given in Figure 2.3a. Mukundan (2008) proposed a parametric approach to reconstruct the force and motion behaviours of a riser subject to VIV from exper-

imentally obtained hydrodynamic coefficient database (Gopalkrishnan, 1993).

Hover et al. (1998) compared free and forced vibration test results of a uniform cylinder and a tapered cylinder at MIT using the apparatus based on that of Gopalkrishnan (1993). The uniform rigid cylinder had a diameter of 3.17 cm and a length of 62 cm. The forced oscillation tests were carried out at a $Re = 3800$. No significant deviations in lift coefficient were observed between the current experiments and those of Gopalkrishnan (1993). They also found that forced VIV tests have a much greater spanwise correlation than free VIV tests in a nominal reduced velocity range of approximately 5.0-6.25. The lift coefficients obtained from the free tests together with the contours from forced tests are presented in Figure 2.3b.

In 2003, ExxonMobil conducted both forced and free vibration tests of a 0.22-m diameter, 3.96-m long rigid cylinder with different surface roughnesses at the David Taylor Model Basin. The lift coefficient contour of the large-roughness cylinder ($k_s/D = 0.002$) is shown in Figure 2.3c. The spring configurations, and thus the Reynolds number ranges (spanning the critical $Re$ region), were the same in all cases.

Oakley and Spencer (2004) carried out free and forced oscillation tests on a 0.325-m diameter, 6.02-m long rigid cylinder under both 1-DOF and 2-DOF scenarios as part of the DeepStar Joint Industry Project. The lift coefficient contour obtained from forced vibration tests are given in Figure 2.3d. Also depicted are the data points obtained from the forced vibration tests when the lift coefficient was found to be zero. Figure 2.3d also distinguishes the difference between the shape of zero-lift contour interpolated bilinearly from the database and that from forced oscillation tests. It indicates that the bilinear interpolation of the database can reasonably capture the shape of lift contours.

In 2003, 2H Offshore conducted forced oscillation tests on a riser-scale roughened cylinder with a diameter of 0.2 m and a length of 3.4 m at a constant towing speed of

0.22 m/s ($Re = 3.96 \times 10^4$) at MARIN. The nondimensional lift coefficient in phase with velocity is shown in Figure 2.3e with respect to reduced velocity and amplitude ratio. Bridge et al. (2005) made use of parabolic curve fit to reconstruct the lift and added mass coefficients as functions of amplitude ratio based on the model tests at a given reduced velocity. Each lift curve consists of two parabolas defined by three points: the lift coefficient at zero amplitude, the amplitude ratio at the maximum lift coefficient, and the zero crossing point (the amplitude at which the lift coefficient equals zero).

Note that different parameters were used as $x$-axes in Figures 2.3a to 2.3e: in Figure 2.3a, the $x$-axis represents the nondimensional oscillation frequency $\hat{f}$; in Figure 2.3c, the $x$-axis stands for the nominal reduced velocity $U^*$ based on the natural frequency in still water, $f_{nw}$; in Figures 2.3b, 2.3d, and 2.3e, by contrast, the $x$-axis is the reduced velocity $V_r$ based on forced vibration frequency, and is thus the reciprocal of that in Figure 2.3a.

From Figure 2.3, it can be observed that the lift coefficient contours vary under different test conditions. In subcritical Reynolds regimes, positive lift coefficients comprise two zones, see Figures 2.3a and 2.3b; while in riser-scale $Re$ regimes (critical and supercritical $Re$ regimes), lift coefficients are positive in a single region, and the abscissas of zero-valued contour are shifted from approximately $V_r = 3.2$-$8.3$ to $V_r = 5.3$-$9.0$ comparing those in Figures 2.3a and 2.3d. In spite of the different $x$-axes used in Figures 2.3c and 2.3d, these two contours are quantitatively in reasonable agreement, while Figure 2.3c has a broader $V_r$ range for positive lift coefficient due to the use of the calm water natural frequency in the calculation of reduced velocity.

Figure 2.4 shows the added mass coefficient contour obtained from forced vibration tests in the literature. Also presented in Figures 2.4b and 2.4d are the superimpositions of the free vibration data and the zero-lift contour from forced tests,
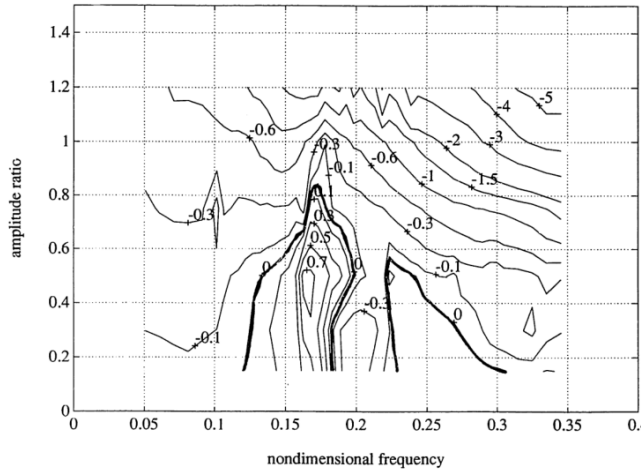
(a) Gopalkrishnan (1993)
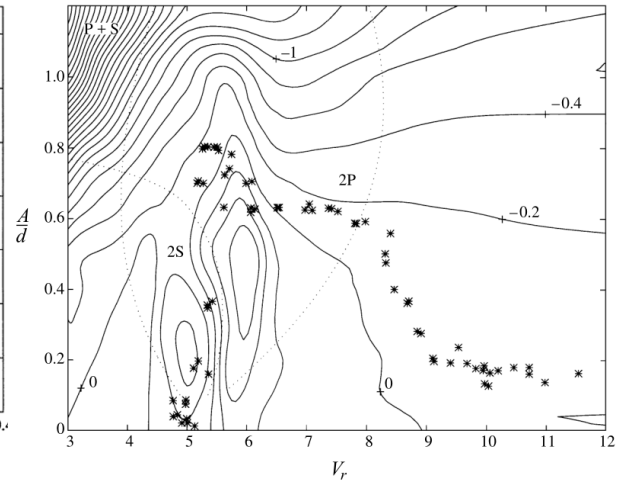
(b) Hover et al. (1998)
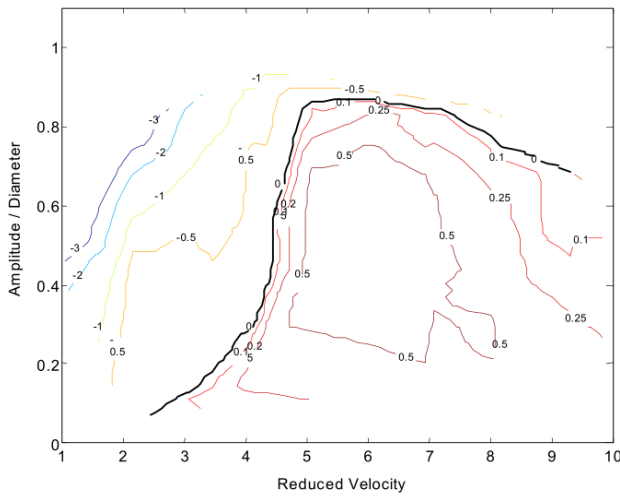
(c) Ding et al. (2004)
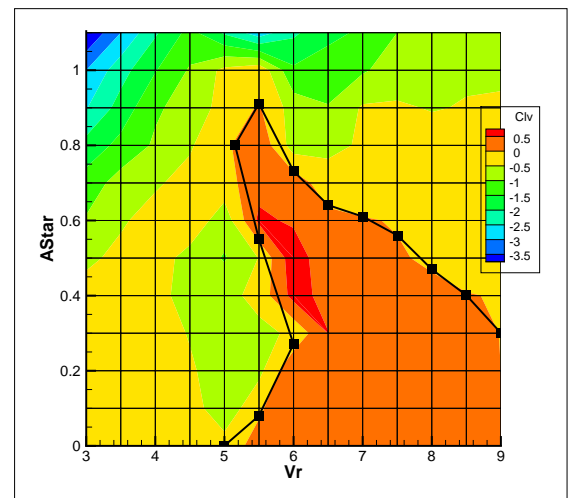
(d) Oakley and Spencer (2004)
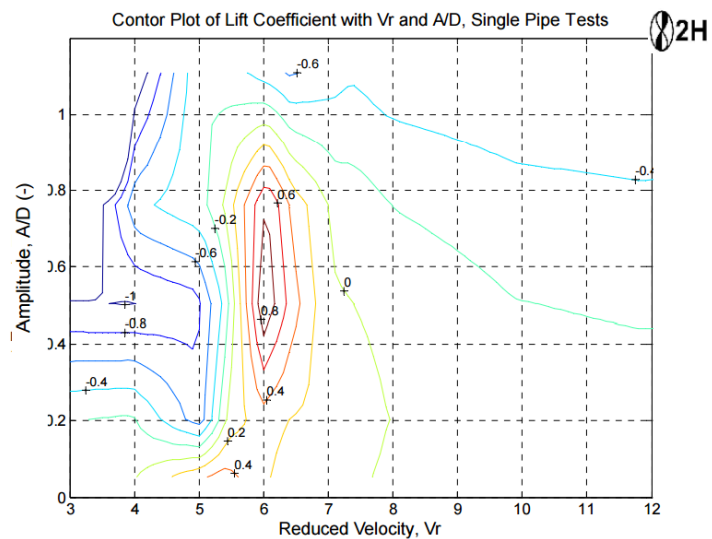
(e) Bridge et al. (2005)

Figure 2.3: Lift coefficient contour obtained from forced vibration tests in the literature

respectively.

The added mass coefficient contours become zero at $V_r \approx 6.0$, while a sudden phase shift was observed under the same reduced velocity in the experiment. At high Reynolds numbers (Oakley and Spencer, 2004), added mass coefficients generally have smaller absolute values than those at low Reynolds numbers under the same amplitude ratios and reduced velocities (Gopalkrishnan, 1993; Hover et al., 1998).
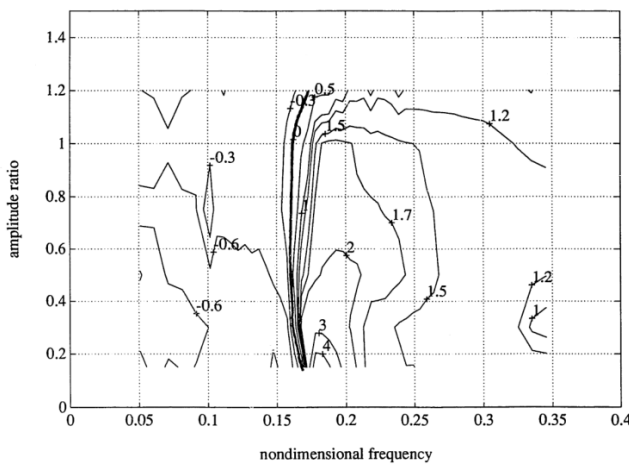


(a) Gopalkrishnan (1993)
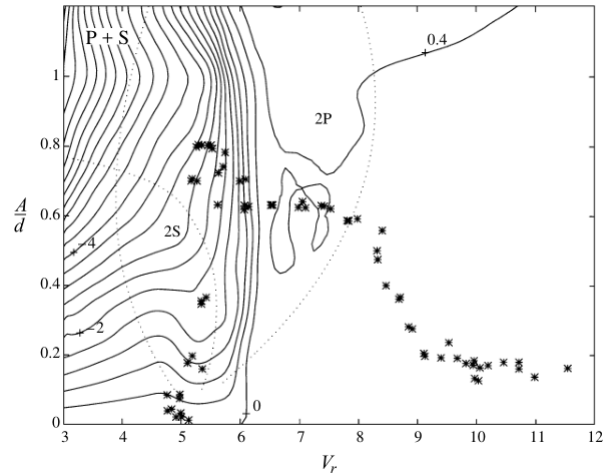
(b) Hover et al. (1998)
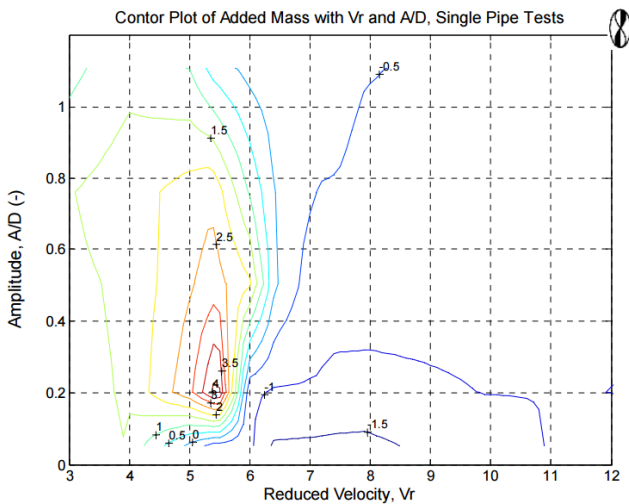
(c) Bridge et al. (2005)
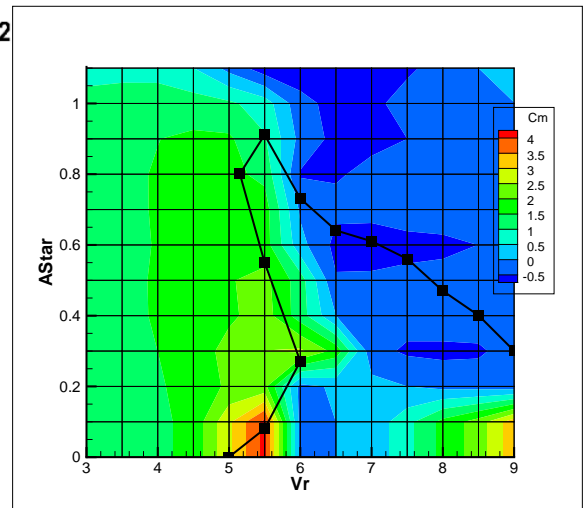
(d) Oakley and Spencer (2004)

Figure 2.4: Added mass coefficient contour obtained from forced vibration tests in the literature

Figure 2.5 presents the added mass coefficient with respect to the nominal reduced velocity for free vibration tests (Oakley and Spencer, 2004). Comparing Figure 2.5 with Figure 2.4d, it can be seen that significant differences exist in the magnitudes of added mass coefficients at low $V_r$ and $U^*$. Added mass coefficients greater than 4.14 were never observed in forced vibration tests; however, as large as $C_m \approx 13$ was obtained in free oscillation tests, indicating again that fundamental difference exists between forced and free vibration tests. In free VIV tests, added mass coefficient $C_m$ was around -1.0 when the nominal reduced velocity $U^* \gtrsim 8$.
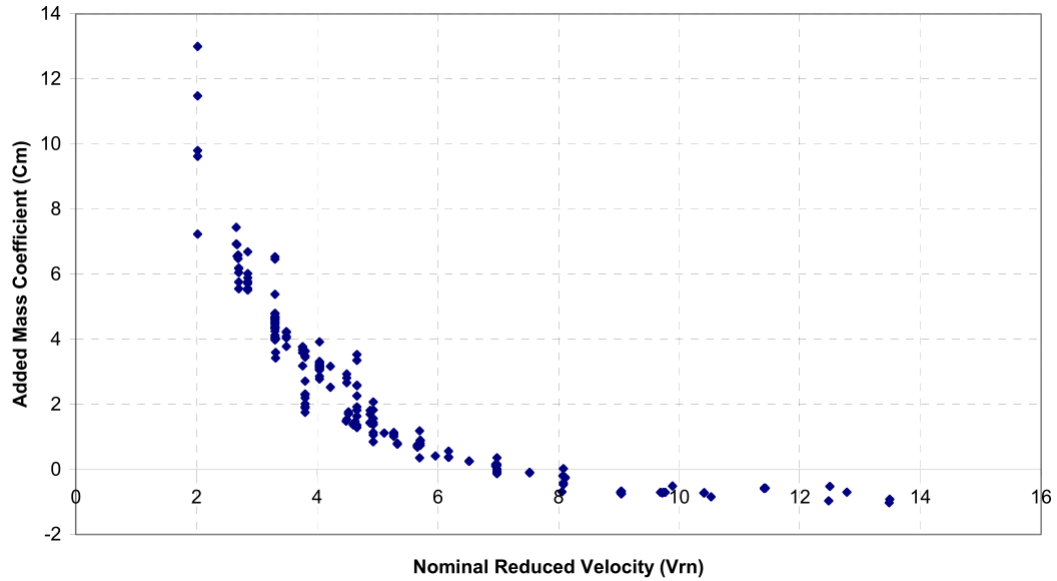


Figure 2.5: Added mass coefficient $C_m$ vs. $V_{rn}$, free VIV, $k/D = 0.0025$ (from Oakley and Spencer (2004))

It is desirable to make full use of the hydrodynamic coefficients database obtained from forced oscillation tests for VIV predictions.

# Chapter 3

# Time-Domain VIV Prediction Model

In this study, a semi-empirical time-domain model was further developed and validated to predict VIV by using the hydrodynamic coefficients collected from forced oscillation tests (Oakley and Spencer, 2004) in the DeepStar Joint Industry Project (JIP). In the DeepStar-JIP, a rigid cylinder was towed at high $Re$ (up to $1.8 \times 10^6$) subject to controlled oscillations in the cross-flow direction. This chapter describes in detail the improvement of the time-domain VIV model based on the work of Spencer et al. (2007) and Ma et al. (2014).

## 3.1  DeepStar High $Re$ VIV Tests

Both forced and free vibration tests were conducted on the same rigid cylinder, with a diameter of 0.325 m and a length of 6.02 m, in the DeepStar JIP (Oakley and Spencer, 2004). In the forced VIV test mode, the cylinder was towed horizontally through water with forced oscillations in the transverse direction. End plates were

31

fitted at both ends to eliminate the 3-D flow effect. The experiment apparatus is illustrated in Figure 3.1.
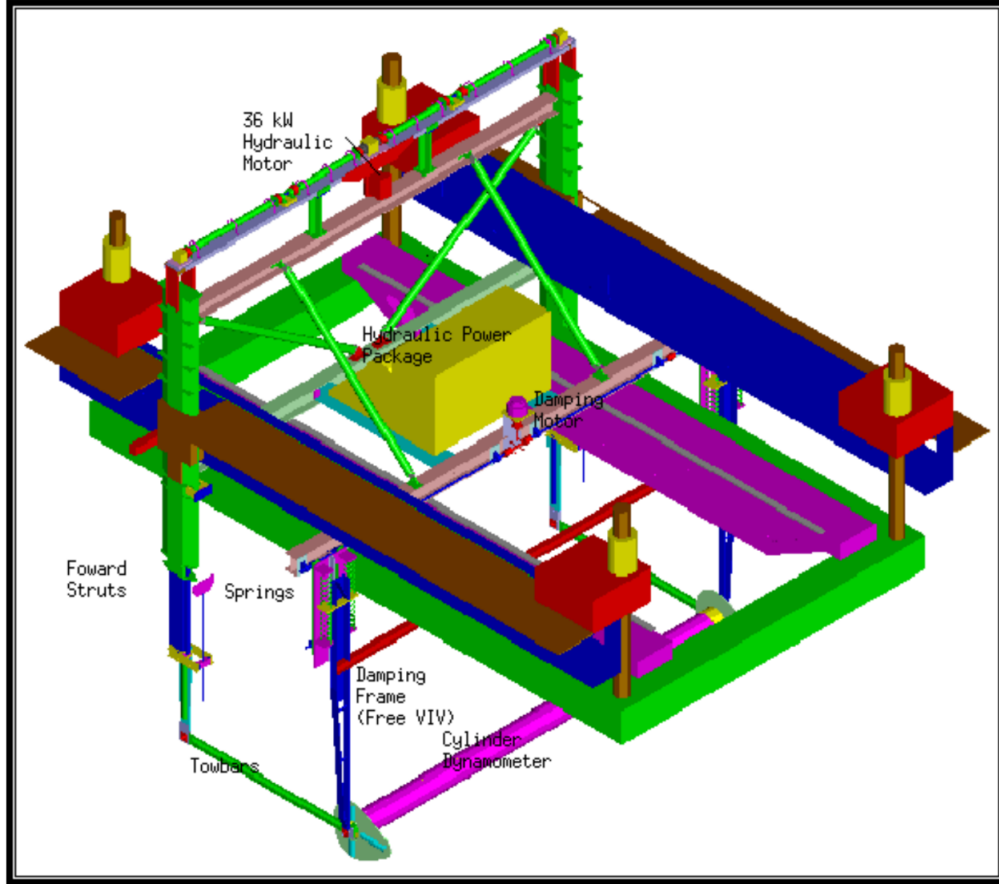


Figure 3.1: DeepStar-JIP VIV test apparatus (from Oakley and Spencer (2004))

In the DeepStar database, the nondimensional hydrodynamic coefficients are presented in terms of two state variables: amplitude-to-diameter ratio, $A^*$, and reduced velocity, $V_r$, which are defined as:

$$A^* = \frac{A}{D}$$
$$V_r = \frac{V_{tow}}{f_{osc}\, D}$$

(3.1)

where $f_{osc}$ is the forced vibration frequency, $A$ is the motion amplitude, $D$ is the

diameter of the cylinder, and $V_{tow}$ is the carriage towing speed.

The measured hydrodynamic forces exerting on the cylinder were decomposed into two orthogonal components with respect to the flow direction, namely, an in-line drag component and a cross-flow lift component. The lift force was further decomposed into one component in phase with velocity and one in phase with acceleration. The nondimensional hydrodynamic coefficients, including the lift coefficient $C_{lv}$, the added mass coefficient $C_m$, and the in-line drag coefficient $C_d$, were deduced from the integrations and normalizations of the two lift components and the drag force over an integer number of full cycles through (Oakley and Spencer, 2004):

$$
\begin{aligned}
C_{lv} &= \frac{F_z \cdot \dot{z}}{\frac{1}{2}\rho_f DLV_{tow}^2 \cdot \frac{1}{\sqrt{2}}\sigma_{\dot{z}}} \\
C_m &= \frac{-F_z \cdot \ddot{z}}{\frac{\pi}{4}\rho_f D^2 L \cdot \sigma_{\ddot{z}}^2} \\
C_d &= \frac{F_x \cdot \dot{z}}{\frac{1}{2}\rho_f DLV_{tow}^2 \cdot \frac{1}{\sqrt{2}}\sigma_{\dot{z}}}
\end{aligned}
\tag{3.2}
$$

where $D$ is the diameter, $L$ is the segment length, $\rho_f$ is the fluid density, $V_{tow}$ is the carriage towing speed, $z$ is the cross-flow displacement, the overdots denote the differentiation with respect to time, $F_z$ is the total cross-flow lift force, $\dot{z}$ is the cross-flow velocity, $\ddot{z}$ is the cross-flow acceleration, $F_x$ is the total in-line drag force, and $\sigma$ represents the root-mean-square (RMS) operation of the subscripted quantities.

Figures 3.2 to 3.7 illustrate the 2-D and 3-D contour plots of $C_{lv}$, $C_m$, and $C_d$, respectively, (Oakley and Spencer, 2004).

In the cross-flow direction, $C_{lv}$ alone determines the energy exchange between the structure and the ambient fluid field. When $C_{lv}$ is positive, energy is input into the structure and therefore the VIV motion is excited, while when $C_{lv}$ is negative, energy is extracted from the structure and hence the VIV motion is dampened. It should be noted that positive and negative values of $C_{lv}$ coexist in the range of $5 < V_r < 8$.

On the other hand, $C_m$ can also be either positive or negative. This indicates changes in the apparent mass and therefore the natural frequency of the system. When the apparent mass decreases, the natural frequency of the system will increase.

The in-line drag force oscillates around a non-zero mean value at a frequency twice that of the lift force, which oscillates around zero. Therefore, $C_d$ includes one mean part and an oscillating component.
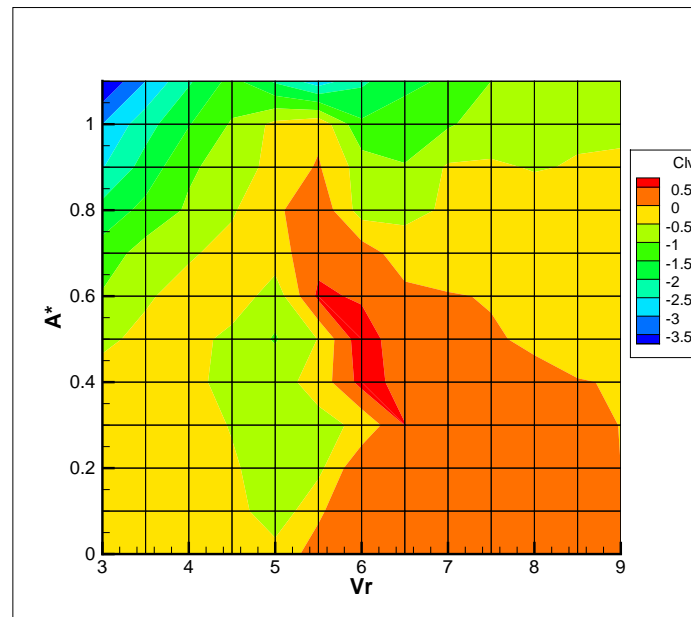
Figure 3.2: 2-D contours of lift coefficient in terms of $(A^*, V_r)$
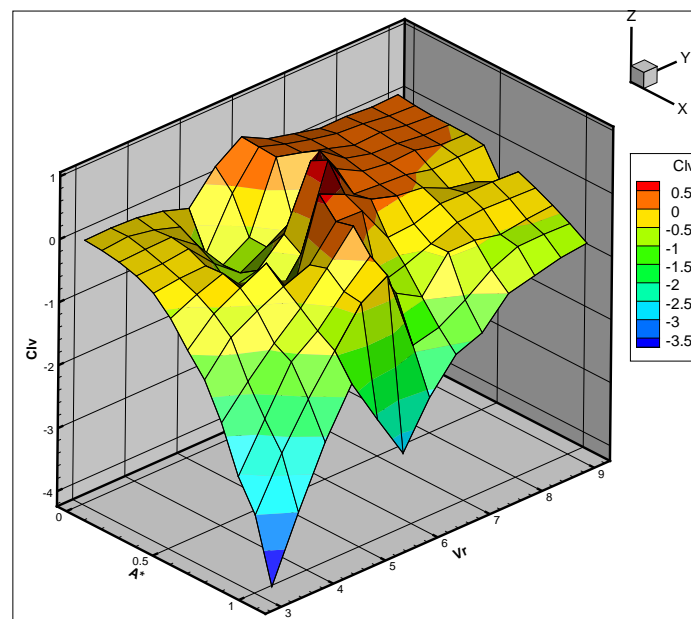


Figure 3.3: 3-D contours of lift coefficient in terms of $(A^*, V_r)$
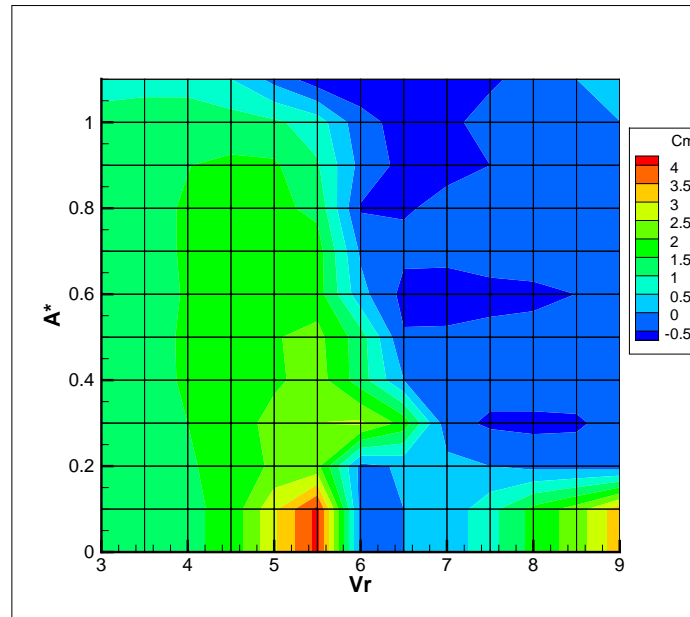
Figure 3.4: 2-D contours of added mass coefficient in terms of $(A^*, V_r)$
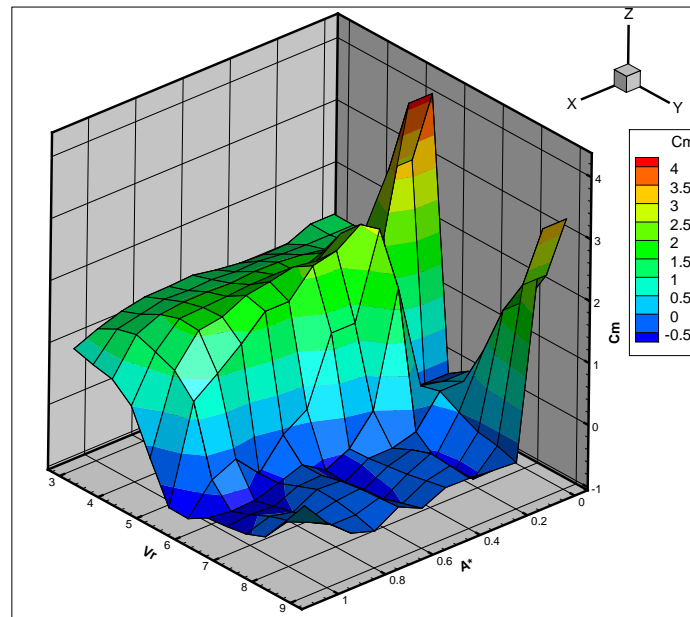


Figure 3.5: 3-D contours of added mass coefficient in terms of $(A^*, V_r)$
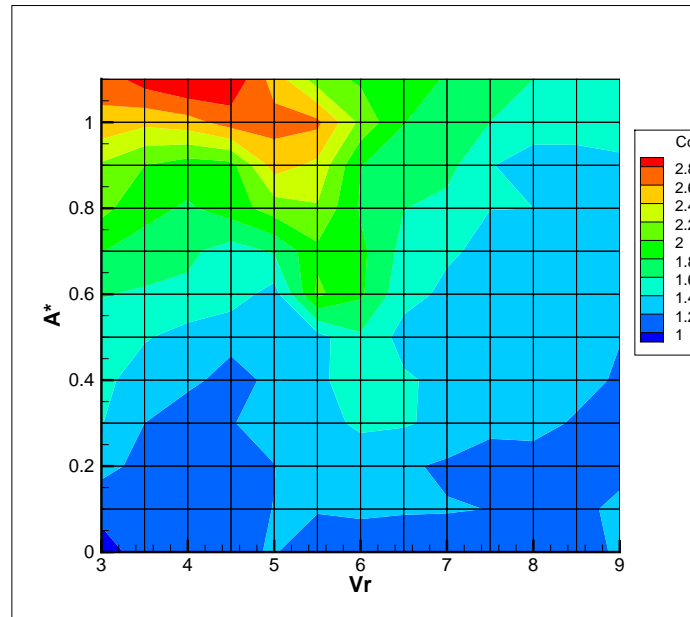
Figure 3.6: 2-D contours of drag coefficient in terms of $(A^*, V_r)$
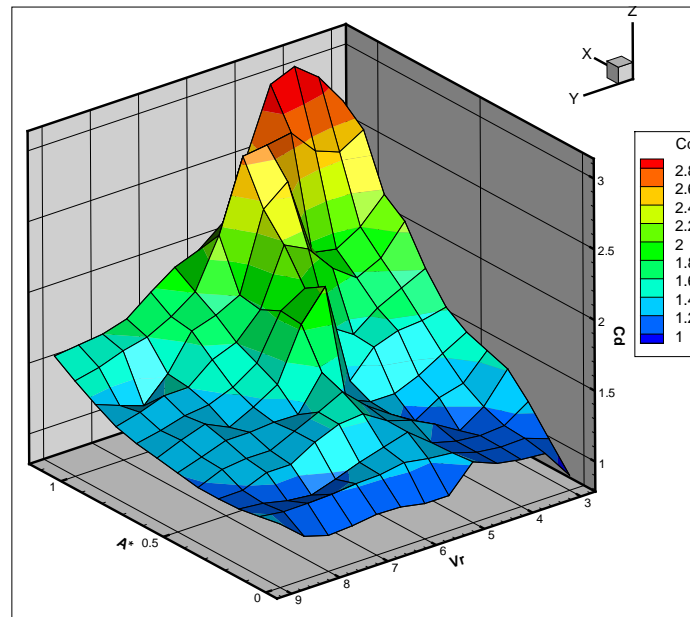


Figure 3.7: 3-D contours of drag coefficient in terms of $(A^*, V_r)$

## 3.2 Time-Domain VIV Prediction Model

Spencer et al. (2007) and Ma et al. (2014) predicted the hydrodynamic forces on a cylinder in the current VIV cycle by utilizing the state variables, $A^*$ and $V_r$, calculated from the last cycle. The underlining assumption was that the cylinder experiences negligible motion variations from cycle to cycle. In their models, the state variables were determined in a progressive manner by a zero up-crossing analysis of the transverse velocity. Once the last state variables had been calculated, hydrodynamic coefficients $C_{lv}$, $C_m$, $C_d$ were determined from the database by interpolations. These coefficients were further used to calculate the forces on the cylinder at the current cycle.

In the present model, the zero up-crossing analysis is applied to the cross-flow displacement. Within the previous cycle, the maximum and minimum displacements, $Z_{max}$ and $Z_{min}$, as well as the apparent period, $T_{app}$, are identified and used to calculate the current state variables, $A^*$ and $V_r$, as below:

$$
\begin{aligned}
A^* &= \frac{Z_{max} - Z_{min}}{2\,D} \\
V_r &= \frac{V\,T_{app}}{D}
\end{aligned}
\tag{3.3}
$$

where $V$ is the relative normal velocity between the incoming current and the structure, and $Z_{max}$, $Z_{min}$, and $T_{app}$ are illustrated in Figure 3.8.

The equation of motion for a typical 1-DOF mass-spring-damper system is:

$$
m\ddot{z} + c\dot{z} + kz = F_z(t)
\tag{3.4}
$$

where $m$ is the mass, $c$ is the structural damping coefficient, $k$ is the spring stiffness, and $F_z(t)$ is the external force varied with time $t$.

Based on the zero up-crossing analysis of displacement, $z(t) = A_z \sin(\omega t)$ is
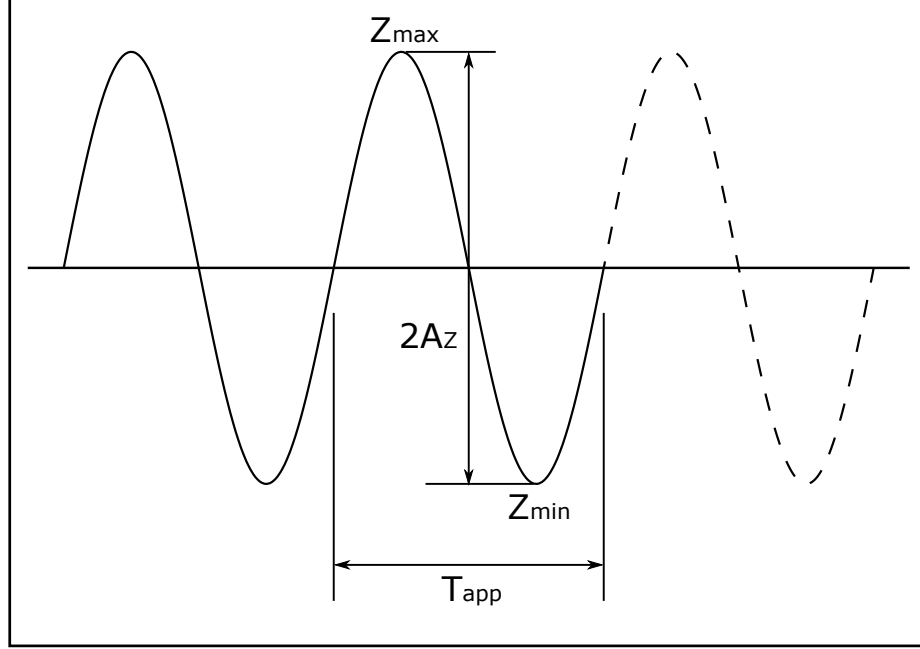
Figure 3.8: Zero up-crossing analysis of transverse displacement

assumed to be a steady-state solution to Equation 3.4. Hence, velocity is $\dot{z} = \omega A_z \cos(\omega t)$ and acceleration is $\ddot{z} = -\omega^2 A_z \sin(\omega t)$, where $A_z$ and $\omega$ are the amplitude and angular frequency of the cross-flow motion, respectively. The overdots denote the differentiation with respect to time.

In an 1-DOF VIV, assuming that the angular frequency of the transverse lift force, $F_z(t)$, equals that of the transverse motion. According to the data reduction procedure in Equation 3.2, $F_z(t)$ can be decomposed into one component in phase with velocity, $F_{\dot{z}}(t)$, and one in phase with acceleration, $F_{\ddot{z}}(t)$ within each motion cycle:

$$F_z(t) = F_{\dot{z}}(t) + F_{\ddot{z}}(t) \tag{3.5}$$

where

$$
\begin{aligned}
F_{\dot{z}}(t) &= C_{lv} \cdot \frac{1}{2}\rho_f D L V^2 \cdot [\cos(\omega t)] \\
F_{\ddot{z}}(t) &= C_m \cdot \frac{\pi}{4}\rho_f D^2 L \cdot \left[-\omega^2 A_z \sin(\omega t)\right]
\end{aligned}
\tag{3.6}
$$

in which $V$ is again the relative normal velocity between the incoming current and the oscillating riser.

To avoid assuming the acceleration, $F_{\ddot{z}}(t)$ is moved to the left-hand-side (LHS) of Equation 3.4 and combined with the term $m\ddot{z}$, leading to:

$$(m + m')\ddot{z} + c\dot{z} + kz = F_{\ddot{z}}(t) \tag{3.7}$$

where $m' = C_m \cdot \frac{\pi}{4}\rho_f D^2 L$ is the added mass.

Assuming that the structural damping is small in comparison with the hydrodynamic damping, the structural damping term, $c\dot{z}$, in Equation 3.4 was neglected in the current model. Note that the hydrodynamic excitation and damping are considered based on the sign of $C_{lv}$ interpolated from the database.

By substituting Equation 3.6 into 3.7 and neglecting the structural damping term, $c\dot{z}$, the equation of motion in the cross-flow direction is given as:

$$[m + m'(A^*, V_r)]\ddot{z} + k_z z = F_L(A^*, V_r)\cos[\omega (t - t_0)] \tag{3.8}$$

where $z$ is the cross-flow displacement, $\ddot{z}$ is the cross-flow acceleration, $m$ is the structural mass, $m'(A^*, V_r)$ is the added mass in the cross-flow direction in terms of $A^*$ and $V_r$, $k_z$ is the structural stiffness in the cross-flow direction, $F_L$ is the lift force amplitude, $t_0$ is the time instant when the last VIV cycle ends, and

$$\omega = \frac{2\pi}{T_{app}}$$
$$F_L(A^*, V_r) = C_{lv}(A^*, V_r) \cdot \frac{1}{2}\rho_f DLV^2 \tag{3.9}$$
$$m'(A^*, V_r) = C_m(A^*, V_r) \cdot \frac{\pi}{4}\rho_f D^2 L$$

By assuming that the added mass coefficient in the in-line direction equals that

in the cross-flow direction, the equation of motion in the in-line direction is described as:

$$[m + m'(A^*, V_r)]\ddot{x} + k_x x = F_{D0} + [F_D(A^*, V_r) - F_{D0}]\cos[2\,\omega\,(t - t_0)] \qquad (3.10)$$

where $x$ is the in-line displacement, $\ddot{x}$ is the in-line acceleration, $k_x$ is the structural stiffness in the in-line direction, $F_{D0}$ is the mean drag force, $F_D$ is the drag force amplitude, and

$$
\begin{aligned}
F_{D0} &= C_{d0} \cdot \frac{1}{2}\rho_f DLV^2 \\
F_D(A^*, V_r) &= C_d(A^*, V_r) \cdot \frac{1}{2}\rho_f DLV^2
\end{aligned}
\qquad (3.11)
$$

in which $C_{d0} = 1.0$ is the mean drag coefficient used in this study. Note that the in-line drag force oscillates at a frequency twice that of the cross-flow lift force.

Note that both the lift component in phase with velocity and the added mass were put on the right-hand-side (RHS) of the equation of motion in the work of Spencer et al. (2007) and Ma et al. (2014).

The proposed forcing model does not explicitly consider the correlation along the span. Instead, the correlation is considered by automatically sharing the motion and forcing information at the common node of adjacent elements in a finite element method. In other words, the zero up-crossing analysis and the progressive calculation in the time domain at both end nodes determine the lock-in or out of lock-in for each element.

As for the initial conditions, the initial hydrodynamic coefficients were set as $C_{m0} = 1.0$ and $C_{lv0} = 1.0$, in the first cycle. Since the nondimensional vortex-shedding frequency is approximately 0.18 over a large range of the subcritical $Re$ regime, the initial forcing frequency was set according to $\omega_f = 2\pi \cdot \frac{V}{5.5 \cdot D}$, where an initial reduced velocity of $V_r = 5.5$, or equivalently an initial Strouhal number of $St = 0.18$, was

chosen. The initial displacement and velocity in the VIV simulations were set as their static equilibrium values.

### 3.2.1 Surface Reconstruction of The DeepStar Database

The hydrodynamic coefficients used in the time-domain simulations were interpolated from the scattered data points in the DeepStar database. In order to achieve this, the SURF routine from the IMSL Numerical Library was utilized by Spencer et al. (2007). The SURF routine is based on Akima (1978), which interpolates a 2-D scattered data by locally quintic polynomials. However, this fifth-order approach would invalidate near the edges or the steep slopes of a surface.

To overcome the drawbacks of the high-order interpolation method, a bilinear scheme was developed by Ma et al. (2014) to interpolate the hydrodynamic coefficients. The effect of the surface reconstruction on the time-domain VIV prediction model was further investigated in this work. The hydrodynamic coefficient surfaces were modelled using bilinear interpolation, bicubic interpolation, and Non-Uniform Rational B-Spline (NURBS) surface. It turned out no significant differences when using higher-order methods compared to that of using bilinear interpolation. In addition, higher-order descriptions of the experimental data would distort the accuracy and fidelity of the interpolated values. Therefore, a bilinear interpolation approach equivalent to that by Ma et al. (2014) is adopted in this study. The detailed surface interpolation scheme is given in Appendix B.

## 3.3 Finite Element Numerical Scheme

The finite element method (FEM) is a numerical tool widely used in almost all branches of engineering. It approximates a continuum by an assemblage of discrete

elements, therefore turning the governing differential equations into a system of algebraic equations. The adjacent elements are interrelated by the common nodes, with each element satisfying its essential and natural boundary conditions.

In deepwater applications, slender marine structures, such as mooring lines and risers, have large length-to-diameter ratios and are hence modelled by Euler-Bernoulli beam elements, which neglect shear deformation and rotary inertia. Following the work of Garrett (1982) and Ran (2000), an in-house finite element program, MAPS-Mooring, was developed (Yin, 2007). MAPS-Mooring was employed in the present studies for the structural analysis of risers. The FEM was formulated in the 3-D global coordinate system. The riser was assumed stretchable in a small and linear manner.

Two-stage computation is performed in MAPS-Mooring: the riser profile under static equilibrium is first obtained based on a Newton iterative method, and the dynamic response and tension of the riser are then integrated by a second-order semi-implicit Adams method in the time domain. The detailed mathematical derivation and numerical procedure of MAPS-Mooring are given in Appendix A.

The present time-domain VIV model was incorporated into MAPS-Mooring to predict the statics and dynamics of slender marine structures. In the present studies, different time integration schemes, other than the second-order semi-implicit Adams method, were investigated. It was indicated that other numerical schemes did not lead to significant improvements in the predictions. Therefore, the original numerical structure in the work of Yin (2007) was adopted.

In the work of Ma et al. (2014), uniform hydrodynamic coefficients were applied on each element which were determined from the state variables by using the velocity of the second node of a finite element. In the present computations, the state variables at the two end nodes of each element were utilized in the zero up-crossing analysis

of the nodal displacements. This resulted in a more continuous hydrodynamic force distribution along the riser span. In addition, the global maximum and minimum nodal displacements were used by Ma et al. (2014) to compute state variables for all elements, while the local motion characteristics were analyzed for each element during the present simulations.

# Chapter 4

# Further Validations of MAPS-Mooring

This chapter presents the validation results of the enhanced MAPS-Mooring, an in-house finite element program originally developed by Yin (2007) that predicts the statics and dynamics of mooring lines. To validate MAPS-Mooring, both static and dynamic simulations were carried out for mooring lines.

A list of cases in the validation studies is given below:

- Static Responses

    - Riser Model Tests at the USNA (Santillan and Virgin, 2011)

        * Catenary Riser

        * Lazy-S and Steep-S Risers

    - Mooring Line of A Wave Energy Converter (Johanning et al., 2007)

- Dynamic Results

    - ISSC Full-Scale Mooring Line Benchmark Case (ISSC, 1997)

&ndash; Light-Weighted Mooring Line Tests at the OTRC (Chen, 2002)

&ndash; Mooring Line Tests at the TU Delft (Raaijmakers and Battjes, 1997)

## 4.1 Static Results

### 4.1.1 Riser Model Tests at the USNA

The statics of riser models were experimentally investigated by Santillan and Virgin (2011) at the United States Naval Academy (USNA). Three types of risers were tested, including catenary riser, lazy-S riser, and steep-S riser. The model test particulars are given in Table 4.1.

Table 4.1: Parameters in the USNA experiments (Santillan and Virgin, 2011)

| Parameter | Value |
|---|---|
| Water depth (m) | 1.53 |
| Diameter (m) | 0.014 |
| Total length (m) | 4.57 |
| Mass per unit length (kg/m) | 63.74 |
| Wet weight per unit length (N/m) | 334.5 |
| EA (kN) | 12.87 |
| EI (kN-m$^2$) | 0.268 |
| Boundary conditions | both ends hinged |

The results presented below include the comparisons of the static profiles between the experimental data and the MAPS-Mooring simulations for different types of riser models. The horizontal offsets and the vertical distances were normalized by the water depth.

**4.1.1.1  Catenary Riser**

The model riser was hinged at both ends and displaced in still water with a segment laid on the tank bottom. The measured riser profile was compared with numerical results using different numbers of elements in Figure 4.1.
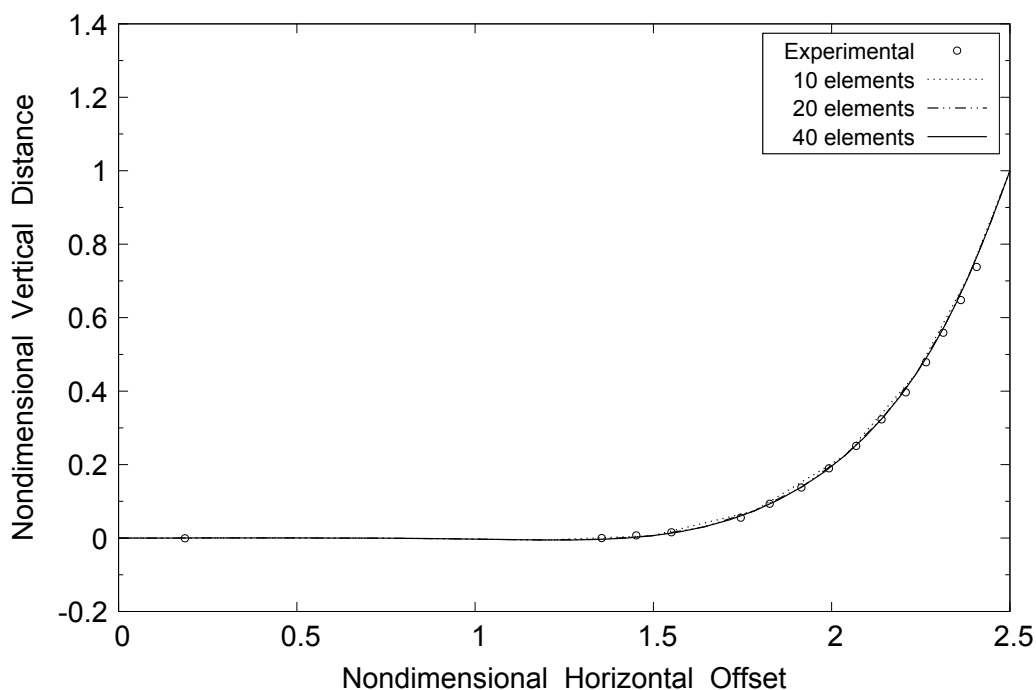


Figure 4.1: Catenary riser static profile

It can be observed that the numerical results are in good agreement with the experimental data, and that the numerical solutions are not very sensitive to the number of elements.

**4.1.1.2  Lazy-S and Steep-S Risers**

In the model test, a buoy was attached at a point along the model riser and led to different lazy-S and steep-S shapes. The numerical static equilibrium profiles compared to the experimental data are presented in Figures 4.2 to 4.5.

It can be seen from Figures 4.2 to 4.5 that the numerical results are in good
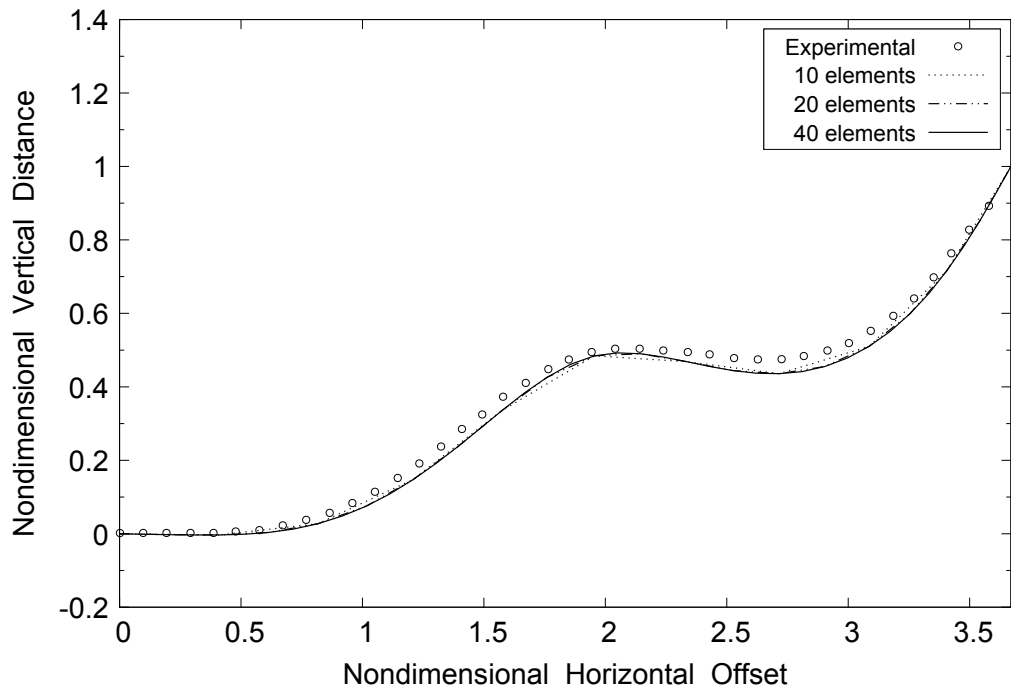
Figure 4.2: Lazy-S riser: configuration A
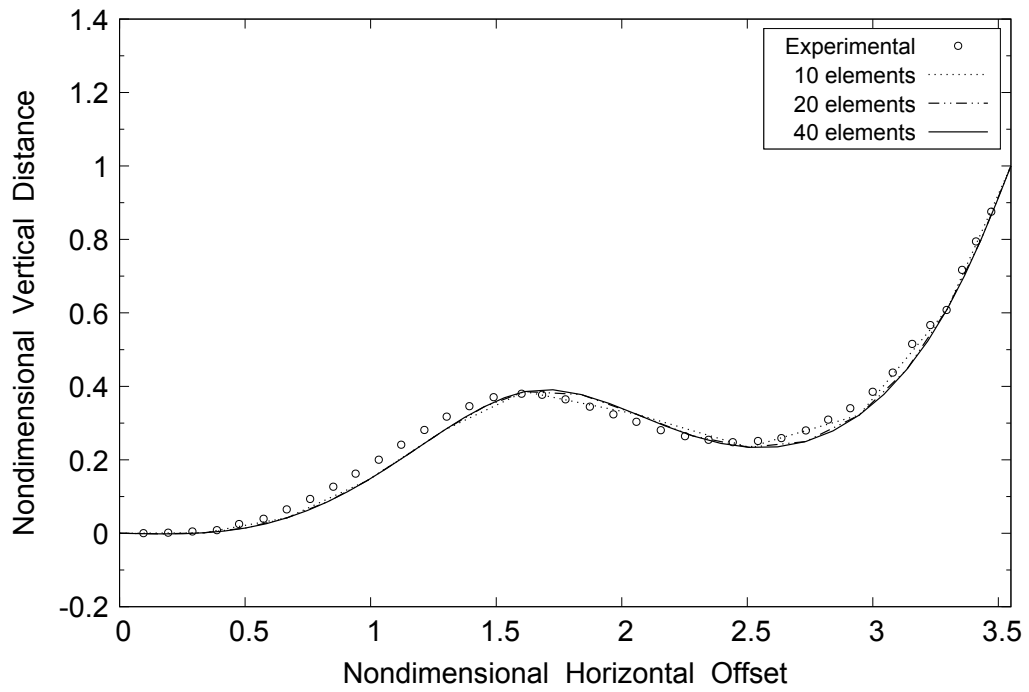


Figure 4.3: Lazy-S riser: configuration B
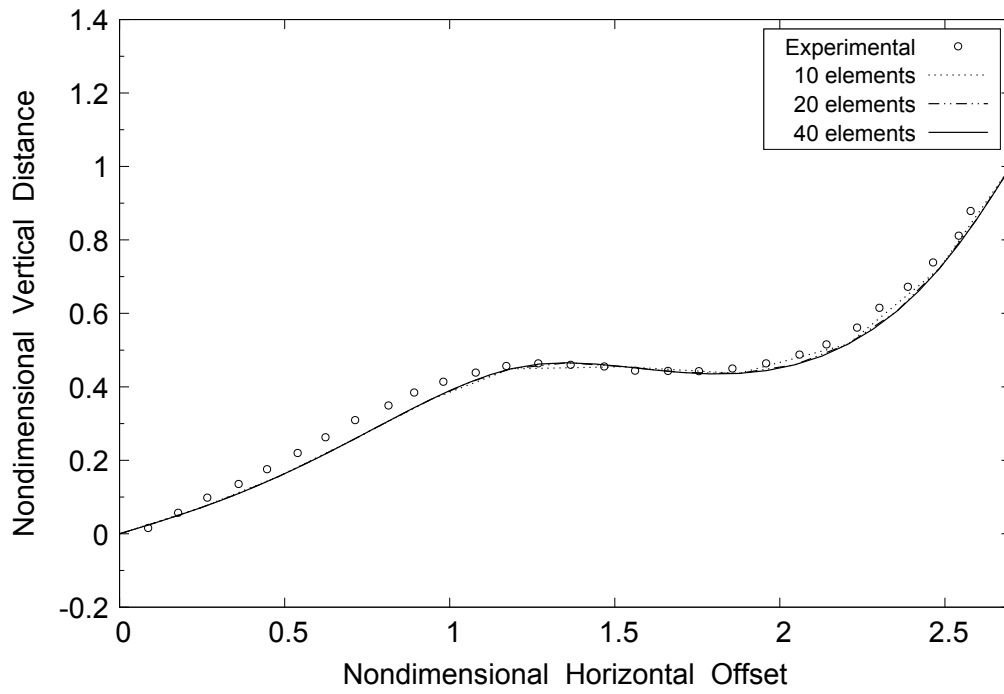
Figure 4.4: Steep-S riser: configuration A
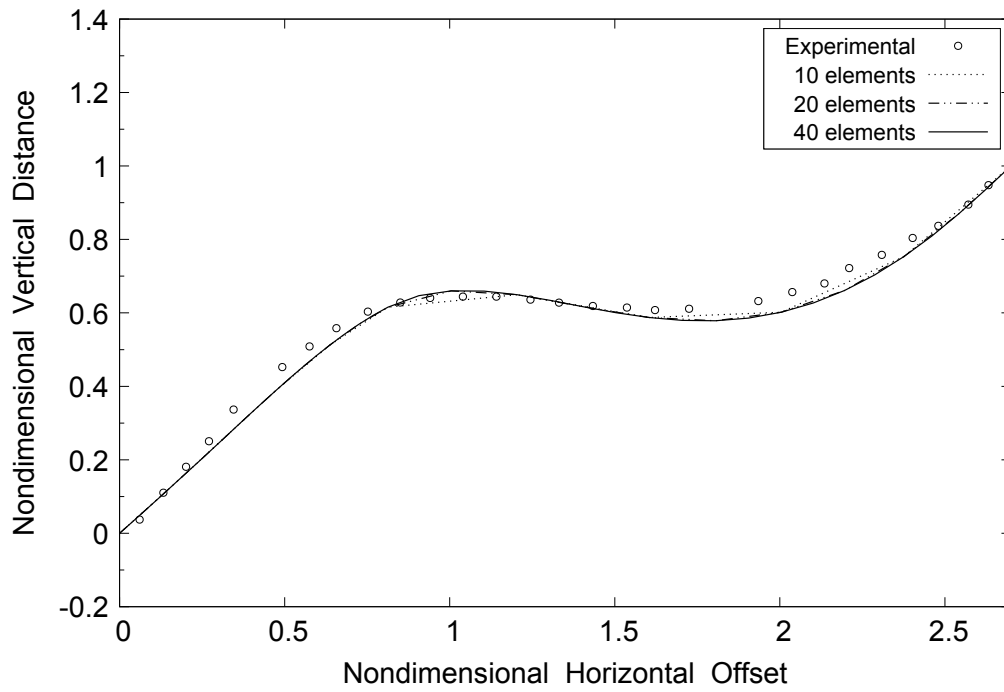


Figure 4.5: Steep-S riser: configuration B

agreement with the experimental measurements, and the numerical result converges as the number of elements increases.

## 4.1.2 Mooring Line of A Wave Energy Converter

A model of shallow-water wave energy converter (WEC) was experimentally examined by Johanning et al. (2007) at Heriot-Watt University. The schematic of the experiment set-up is illustrated in Figure 4.6, and the model test parameters are listed in Table 4.2.
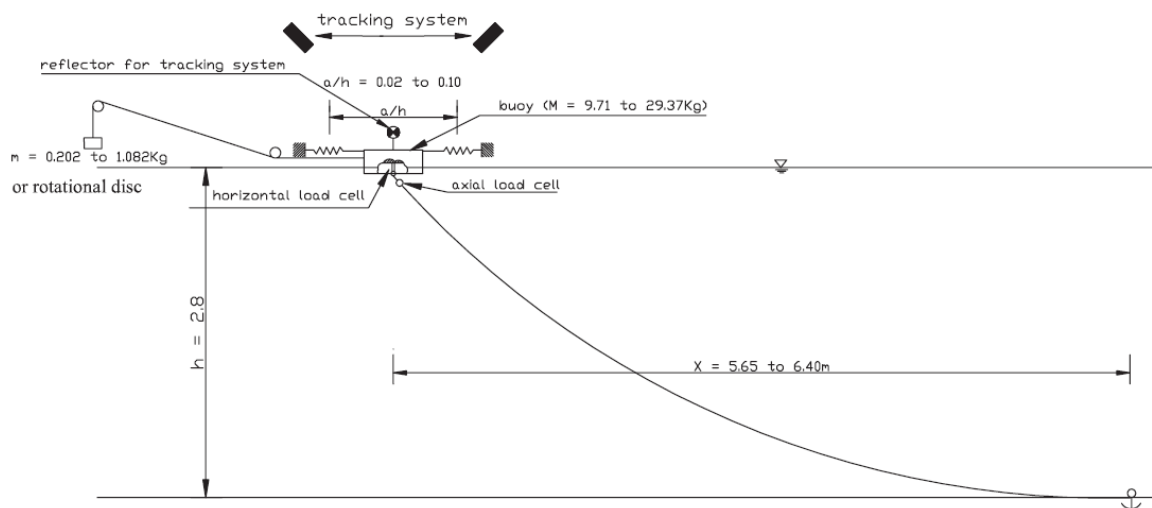


Figure 4.6: Schematic of the experimental set-up (from Johanning et al. (2007))

Table 4.2: Parameters in the moored WEC experiments (Johanning et al., 2007)

| Parameter | Value |
|---|---|
| Water depth (m) | 2.8 |
| Diameter (mm) | 2.5 |
| Total length (m) | 6.98 |
| Wet weight per unit length (N/m) | 1.036 |
| EA (kN) | 560 |
| Boundary conditions | both ends hinged |

The predicted top end pre-tensions under static equilibrium for different fairlead horizontal offsets are compared with the experimental data in Figure 4.7.
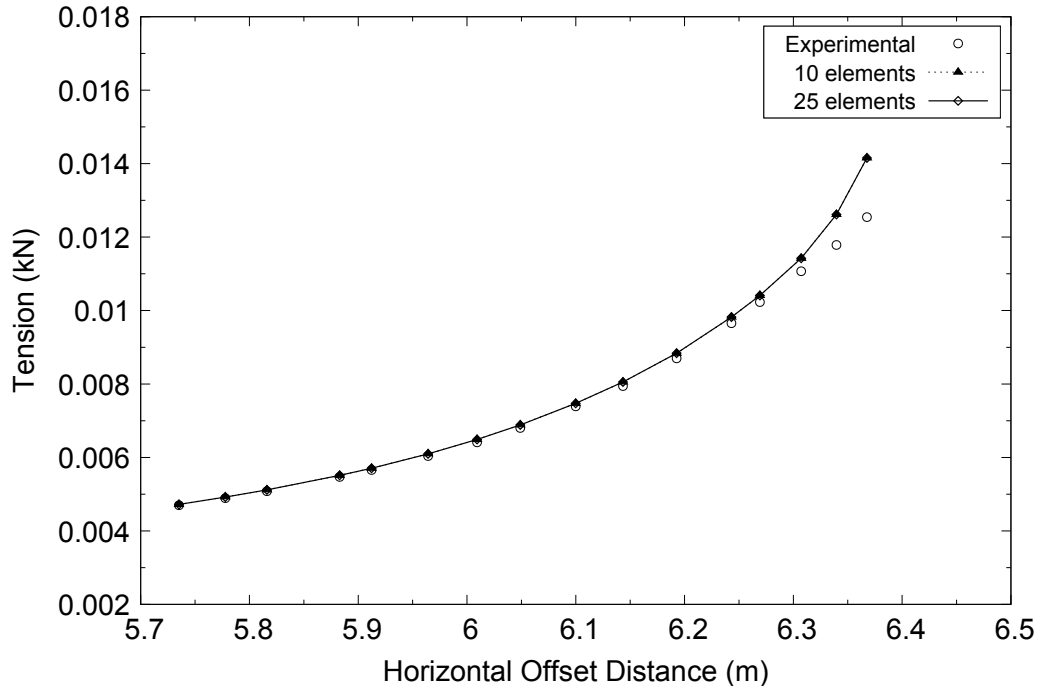
Figure 4.7: Top end static pre-tensions versus different fairlead horizontal offsets

Note that the fourth-to-last data point in Figure 4.7 represents the critical condition under which the mooring line was tangent to the bottom at the anchor point. From Figure 4.7, it can be observed that both numerical results agree quite well with the experimental measurements right before the mooring was immediately lifted up at the anchor point. After the mooring line lost the contact with the bottom and became tauter as the fairlead was moved further away from the anchor, discrepancies in pre-tensions between the model test and numerical simulations start to increase. This may be explained by the fact that the mooring was significantly stretched during the static test, while the axial elongation of the mooring line was assumed linear and small in the mathematical formulation of MAPS-Mooring.

## 4.2   Dynamic Results

### 4.2.1   ISSC Full-Scale Mooring Line Benchmark Case

The 13th International Ship and Offshore Structure Congress Committee (ISSC) initiated a comparative study on the mooring line damping with 15 participants involved (ISSC, 1997). The model parameters in this study are given in Table 4.3.

Table 4.3: Parameters of the ISSC full-scale mooring line (ISSC, 1997)

| Parameter | Value |
|---|---|
| Water depth (m) | 82.5 |
| Diameter (m) | 0.14 |
| Total length (m) | 711.3 |
| Line weight in air (N/m) | 3586.5 |
| Line weight in water (N/m) | 3202.0 |
| EA (kN) | $1.69 \times 10^6$ |
| Line top tension at equilibrium position (kN) | 549.9 |
| Boundary conditions | both ends hinged |

The motion amplitude was normalized by the water depth. In the convergence investigations of the number of elements and the time step, a nondimensional fairlead oscillation amplitude of 0.05 was used. In the convergence study, the number of elements, 20, 40, 80 and 160 elements were employed with a fixed time step of 0.05 sec. In the convergence study of the time step, 0.2 sec, 0.1 sec, 0.05 sec, and 0.025 sec were examined using 80 elements. As shown in Figures 4.8 to 4.9, the numerical results converge as the number of elements increases or the time step decreases.
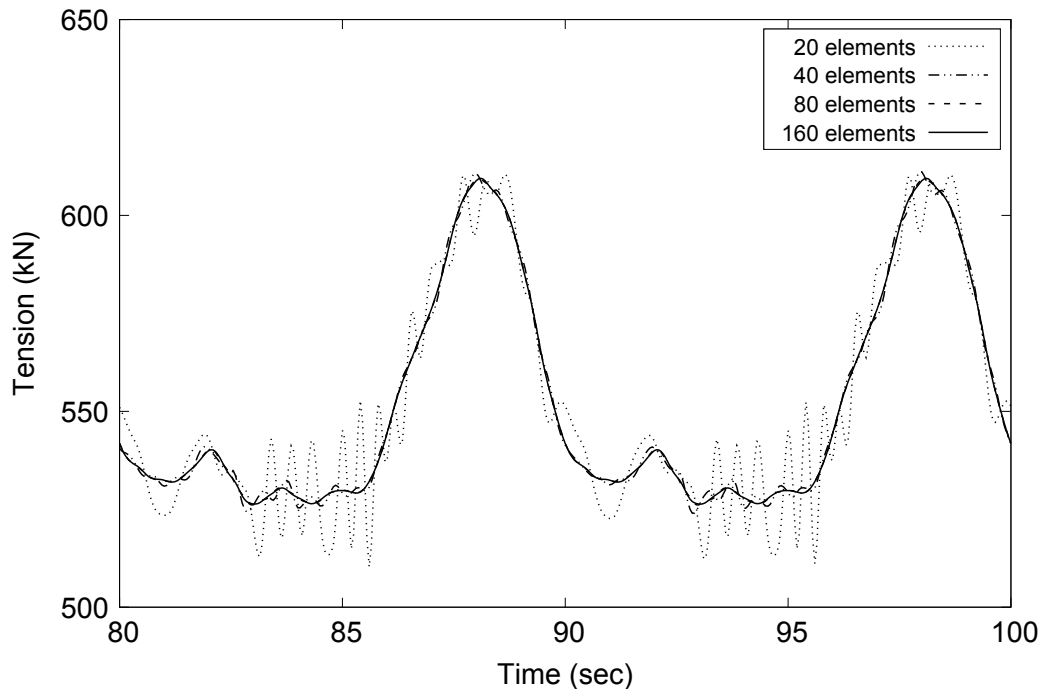
Figure 4.8: Sensitivity to the number of elements
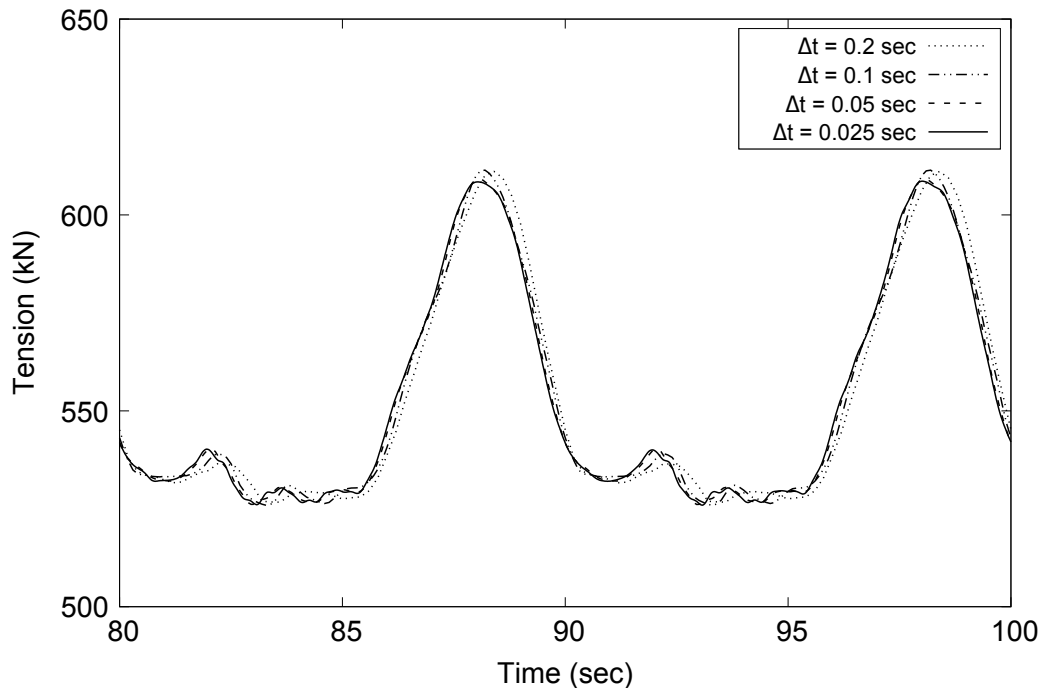


Figure 4.9: Sensitivity to the time step

## 4.2.2 Light-Weighted Mooring Line Tests at the OTRC

Tests of a uniform light-weighted chain model were performed by Chen (2002) at the Offshore Technology Research Center (OTRC) in College Station, Texas. The particulars and results given herein are in prototype scale following the Froude scaling law. The model test set-up is illustrated in Figure 4.10, and the characteristics of the uniform light-weighted chain in full-scale is listed in Table 4.4.
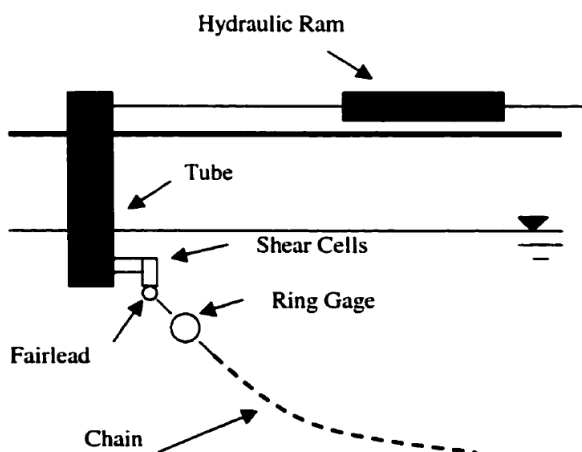


Figure 4.10: Model test set-up at the OTRC (from Chen (2002))

Table 4.4: Parameters in the OTRC model tests (Chen, 2002)

| Parameter | Value |
|---|---|
| Water depth (m) | 223.5 |
| Diameter (m) | 0.14 |
| Total length (m) | 762.0 |
| Mass per unit length (kg/m) | 235.2 |
| Wet weight per unit length (N/m) | 2013.4 |
| EA (kN) | $2.21 \times 10^6$ |
| Normal drag coefficient | 3.2 |
| Tangential drag coefficient | 0.6 |
| Line top tension at equilibrium position (kN) | 1558.8 |
| Boundary conditions | both ends hinged |

The time series of the top tension are compared between the numerical simulations

and the experimental measurements under different fairlead oscillation periods in Figures 4.11, 4.12, and 4.13.

Good agreements between the MAPS-Mooring simulations and the measurements can be observed from Figures 4.11, 4.12, and 4.13.
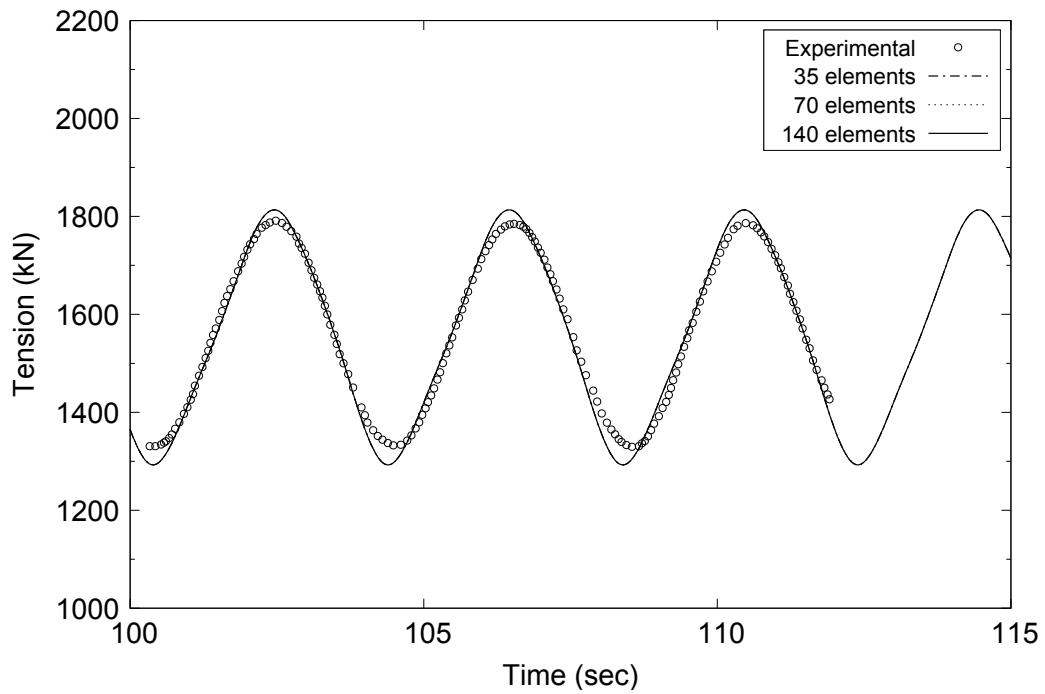
(a) Sensitivity to the number of elements
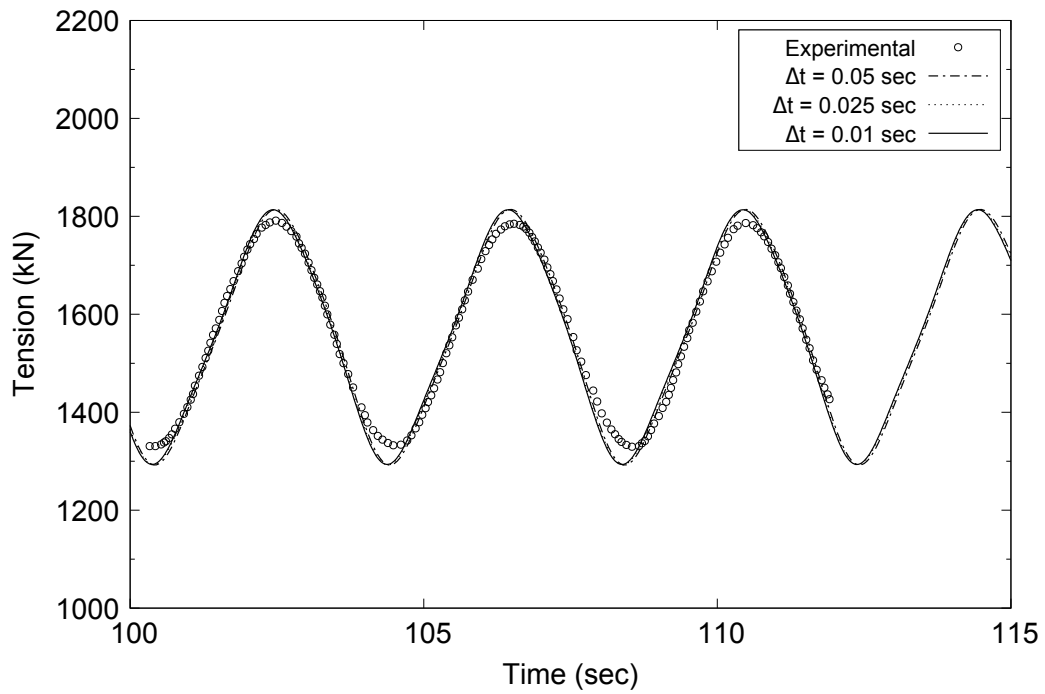


(b) Sensitivity to the time step

Figure 4.11: Time series of the top-end tension, with a fairlead oscillation period of 4 sec and an amplitude of 0.4572 m
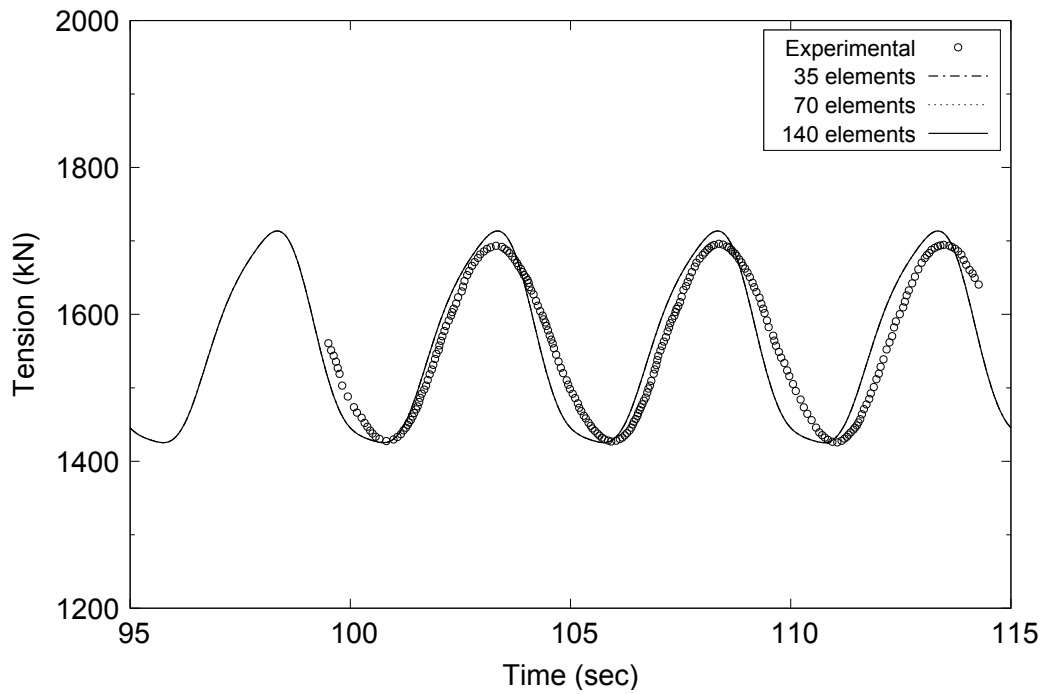
(a) Sensitivity to the number of elements
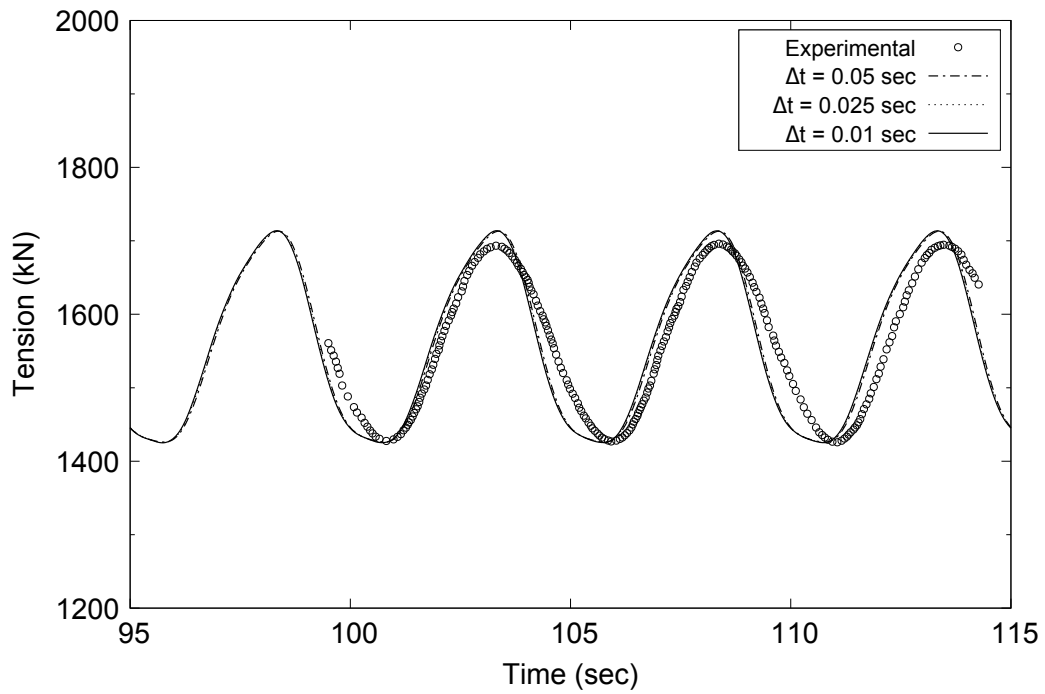


(b) Sensitivity to the time step

Figure 4.12: Time series of the top-end tension, with a fairlead oscillation period of 5 sec and an amplitude of 0.4572 m
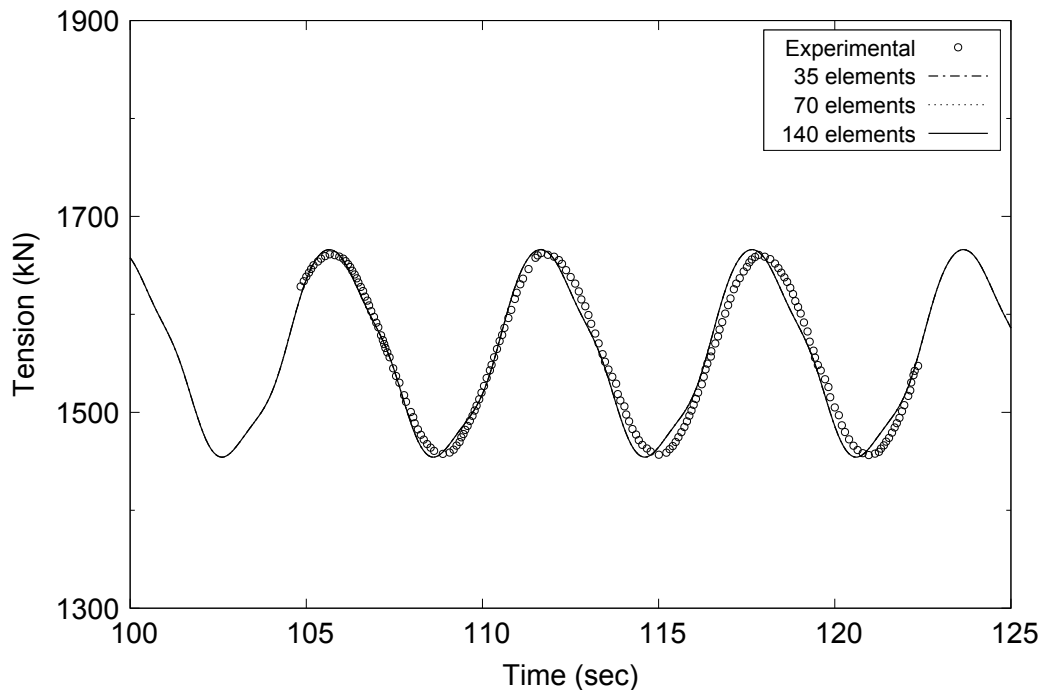
(a) Sensitivity to the number of elements
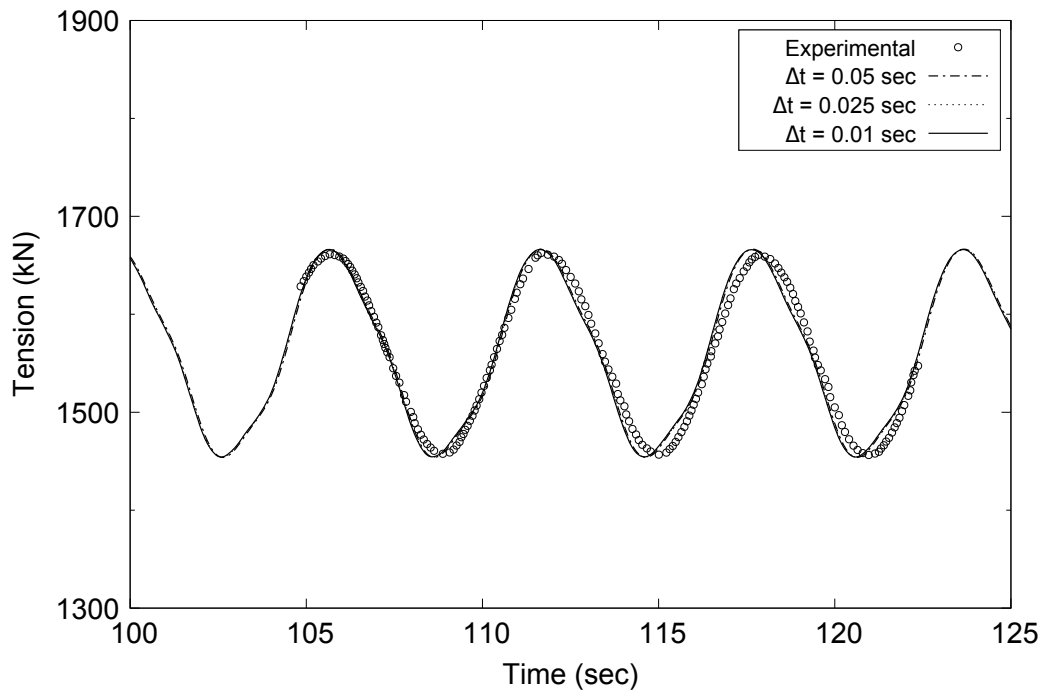


(b) Sensitivity to the time step

Figure 4.13: Time series of the top-end tension, with a fairlead oscillation period of 6 sec and an amplitude of 0.4572 m

### 4.2.3   Mooring Line Tests at the TU Delft

A large number of mooring line model tests were carried out by Raaijmakers and Battjes (1997) at the Delft University of Technology (TU Delft). The mooring line configurations in the model tests are referred to by the fairlead position number and the line (e.g. "position 5, line-A"). The experimental set-up is schematized in Figure 4.14, and the characteristics of the experiment are listed in Table 4.5.
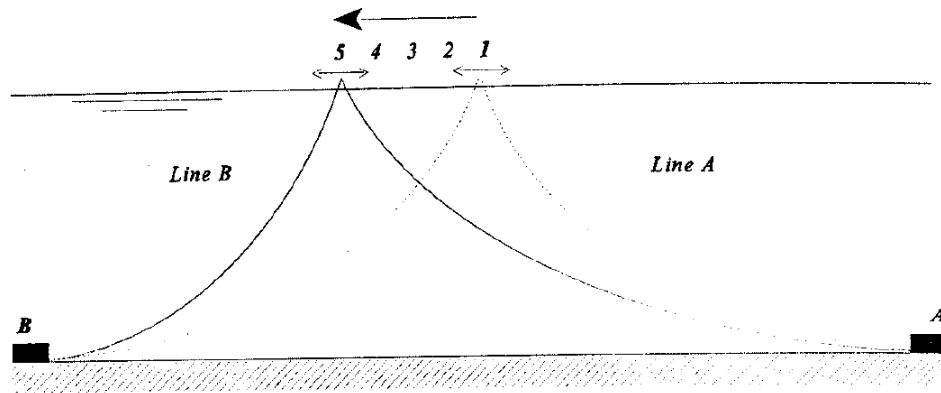


Figure 4.14: Schematic set-up of the Delft mooring tests (from Raaijmakers and Battjes (1997))

Table 4.5: Parameters in the Delft mooring tests (Raaijmakers and Battjes, 1997)

| Parameter | Value |
|---|---|
| Water depth (m) | 1.37 |
| Diameter (mm) | 6.0 |
| Total length (m) | 7.0 |
| Mooring chain density (ton/m$^3$) | 7.9 |
| Wet weight per unit length (N/m) | 6.446 |
| EA (kN) | 3230 |
| Boundary conditions | both ends hinged |

One experimental time series of horizontal tension at the fairlead was compared against MAPS-Mooring simulation results. The top end was oscillated at a period of 1.6 sec with a 0.1-m amplitude. The experimental time series was obtained at a
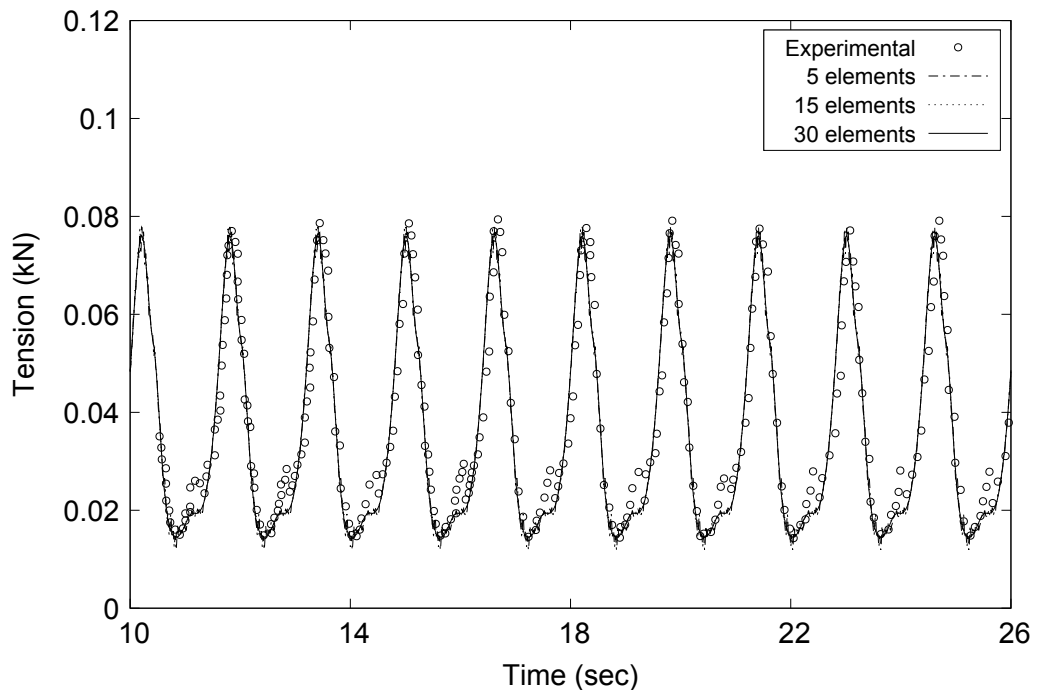
(a) Sensitivity to the number of elements
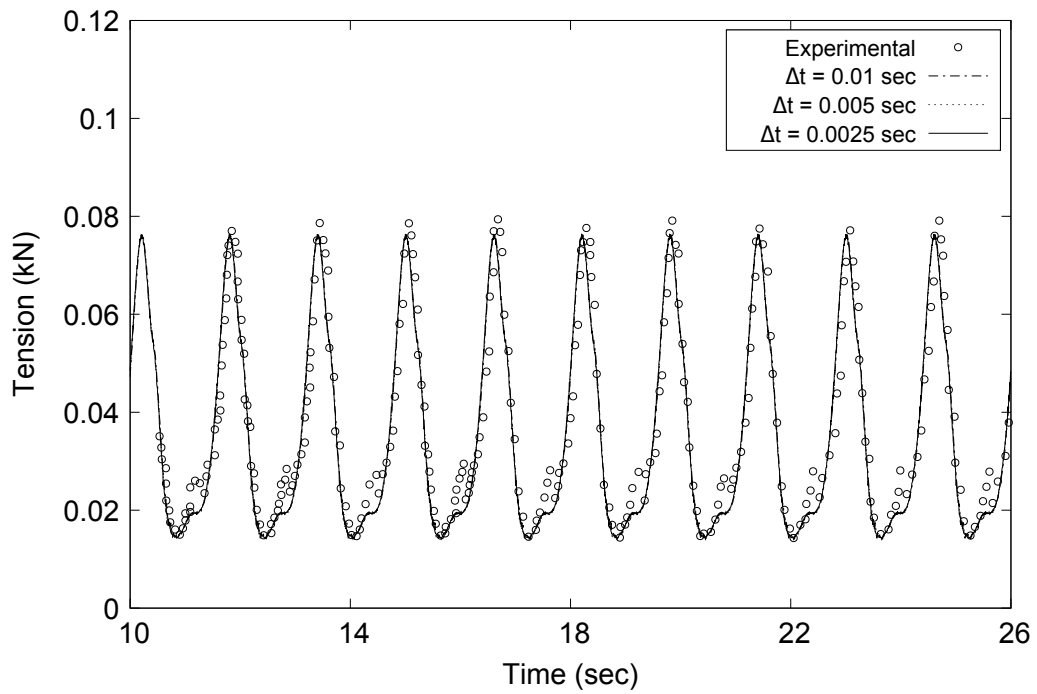


(b) Sensitivity to the time step

Figure 4.15: Horizontal fairlead tension time series, with a fairlead oscillation period of 1.6 sec and an amplitude of 0.1 m

sampling time interval of 0.032 sec. The convergences to the number of elements and the time step in dynamic analysis are investigated and presented in Figure 4.15. The predicted time series of the horizontal tension at the fairlead are in good agreement with the measured ones.

# Chapter 5

# Validations for the VIV Prediction Model

The proposed time-domain VIV prediction model was incorporated with MAPS-Mooring and was used to predict the VIV of rigid and flexible risers. In this chapter, the present model was first examined by simulating the 1-DOF free VIV of a rigid cylinder in a uniform flow on which the hydrodynamic coefficients were collected. The proposed model was then validated by carrying out VIV analysis for a flexible riser model subject to a step current. The numerical results and the discussions on the results are given in the following sections.

## 5.1   Rigid Cylinder Single-Mode VIV

In the free VIV tests of the DeepStar-JIP, the same rigid cylinder was elastically supported on a spring frame while being towed at a constant speed in water (Oakley and Spencer, 2004). External damping was introduced by connecting the cylinder-frame system to a servomotor, which exerted a force proportional to the cylinder VIV

velocity. The particulars of the test segment are given in Table 5.1.

Table 5.1: Parameters in the DeepStar-JIP free VIV tests (Oakley and Spencer, 2004)

| Input | Value |
|---|---|
| Water depth (m) | 7 |
| Diameter (m) | 0.325 |
| Total length (m) | 6.02 |
| Total mass (kg) | 800 |
| Mass ratio | 1.56 |
| Support stiffness (kN/m) | 40 |
| Boundary conditions | both ends spring-supported |

All the numerical results given hereafter started from static equilibrium and were based on one element simulation, with a time step of 0.005 sec. The time series of the nondimensional transverse motion under different nominal reduced velocities are presented in Figures 5.1 to 5.6, where the nominal reduced velocity is defined as:

$$U^* = \frac{U}{f_{nw} D} \tag{5.1}$$

in which $U$ is the incoming current speed, $f_{nw}$ is the natural frequency in still water, and $D$ is the diameter of the cylinder.

Figures 5.1, 5.2, and 5.3 illustrate the time series of the nondimensional cross-flow motion at the fairlead under uniform current speeds of 0.8, 1.2, and 1.6 m/s, respectively. The figures demonstrate that the steady-state response magnitude of the transverse VIV increases as the current speed starts from zero. Those sinusoidal motions correspond to the initial and the upper branches, at which the wake roughly possesses a 2S vortex pattern (Williamson and Roshko, 1988).

As the nominal reduced velocity further increases, the time series of motion exhibit a "beat"-like pattern, as can be observed in Figures 5.4, 5.5, and 5.6. This indicates
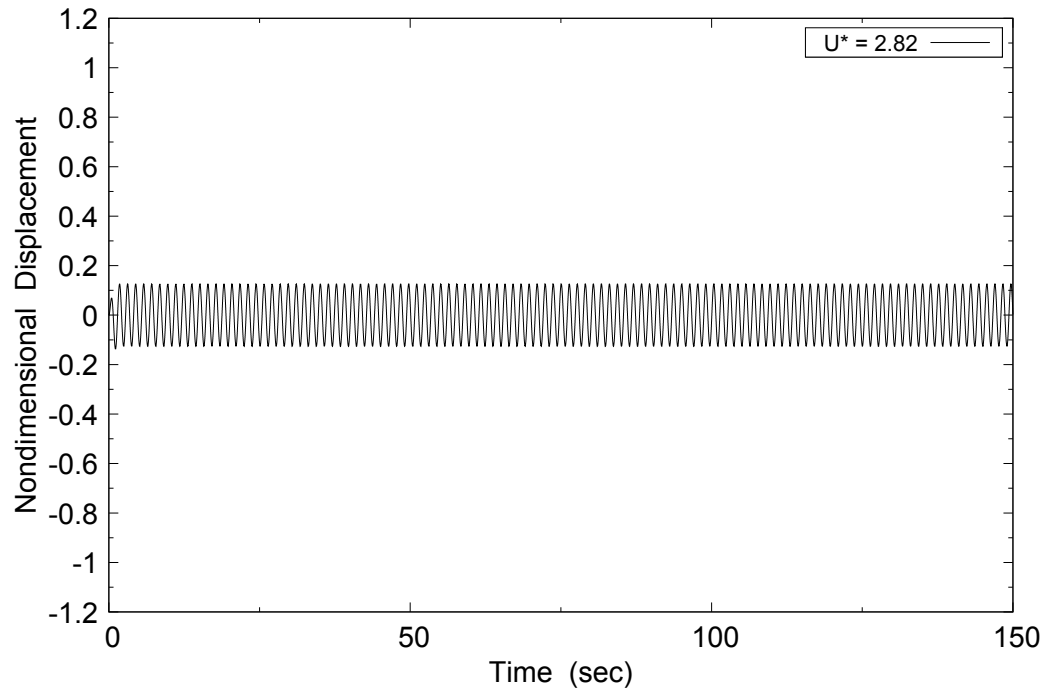
Figure 5.1: Rigid riser 1-DOF VIV under current speed of 0.8 m/s
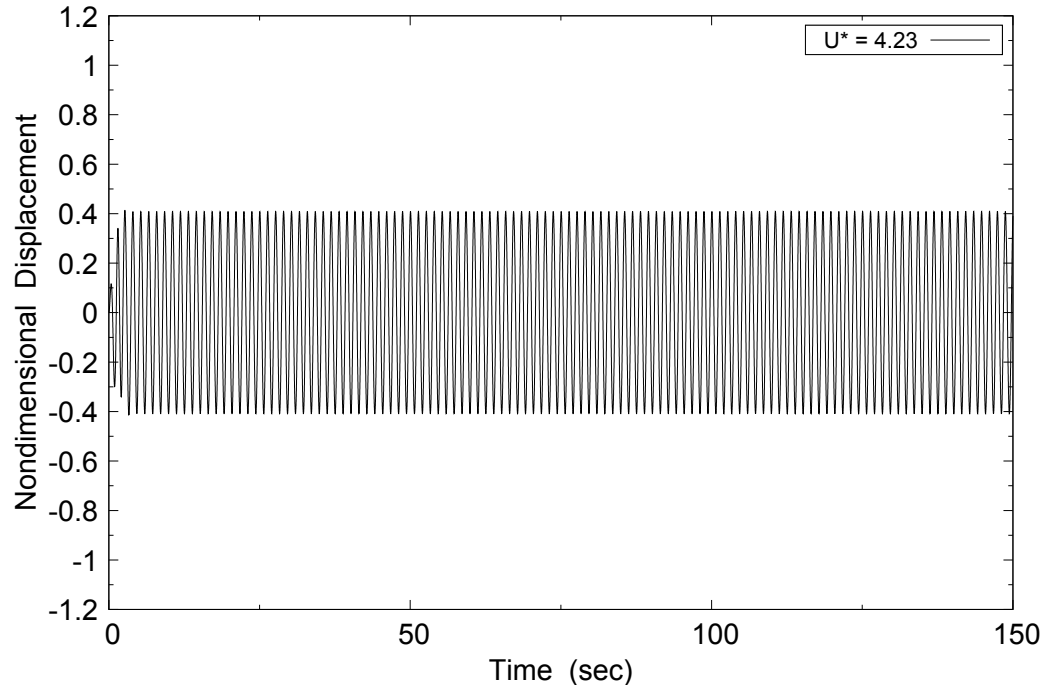


Figure 5.2: Rigid riser 1-DOF VIV under current speed of 1.2 m/s
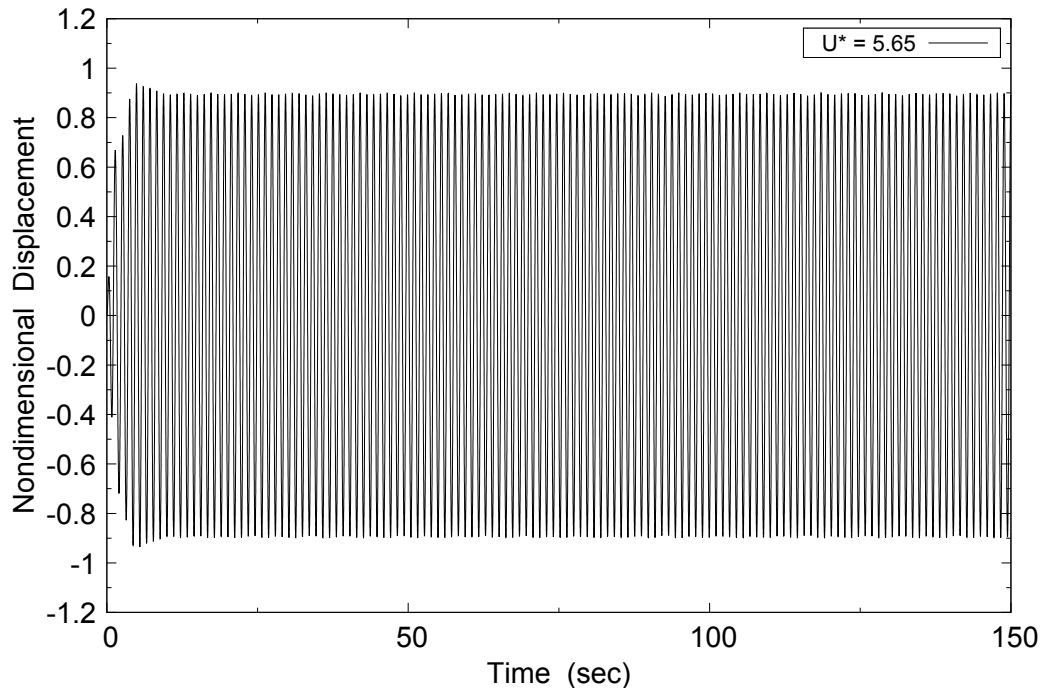
Figure 5.3: Rigid riser 1-DOF VIV under current speed of 1.6 m/s

the competition between the still water natural frequency and the vortex shedding frequency. The nominal reduced velocities in Figures 5.4, 5.5, and 5.6 correspond to 2P vortex mode (Williamson and Roshko, 1988).

Figure 5.7 presents the RMS motion amplitude ratios in terms of the nominal reduced velocity and their comparison with the experimental data as well as those predicted in the work of Ma et al. (2014). The RMS amplitude ratio for each nominal reduced velocity was obtained using the displacement amplitudes in a duration of 150 sec. It can be observed in Figure 5.7 that the present method improved the predictions, especially at the low nominal reduced velocities.
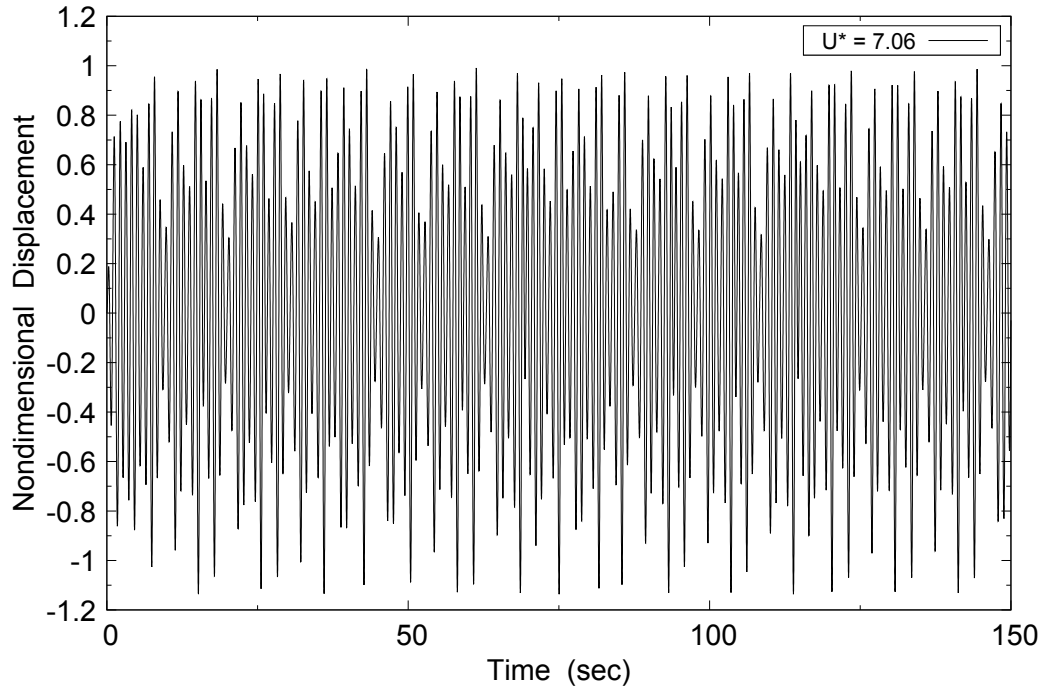
Figure 5.4: Rigid riser 1-DOF VIV under current speed of 2.0 m/s
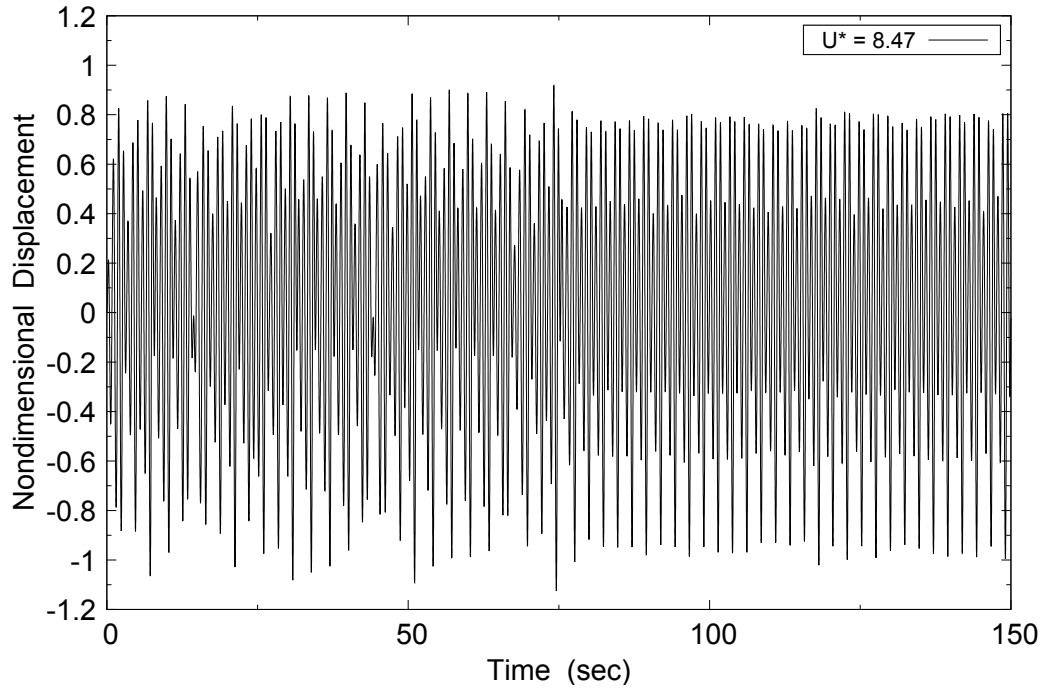


Figure 5.5: Rigid riser 1-DOF VIV under current speed of 2.4 m/s
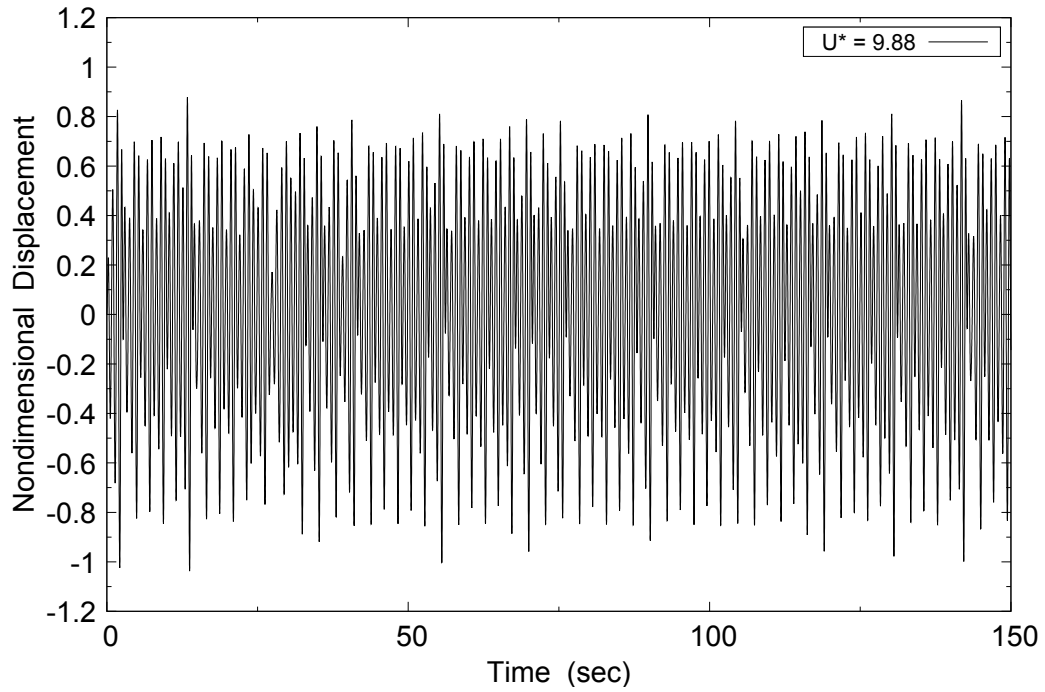
Figure 5.6: Rigid riser 1-DOF VIV under current speed of 2.8 m/s
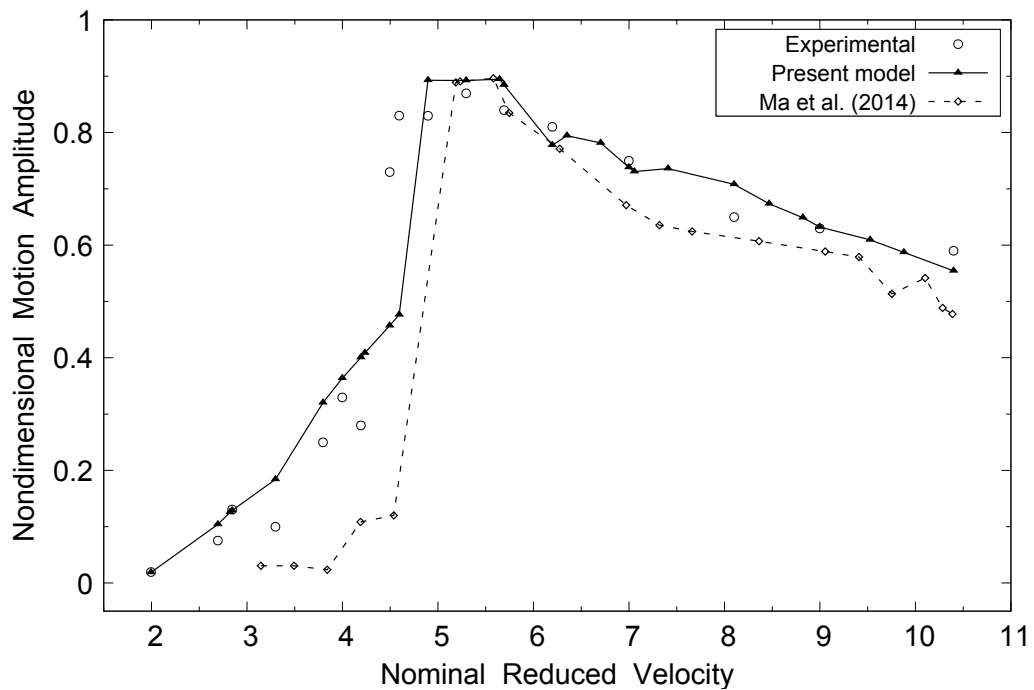


Figure 5.7: Rigid riser 1-DOF VIV amplitude ratio as a function of nominal reduced velocity

## 5.2 Flexible Cylinder Multi-Mode VIV

Tests of a top-tensioned riser model under VIV were conducted by Chaplin et al. (2005b) at the Delft Hydraulics Laboratory. In the test campaign, the riser model, with the upper 55% submerged in a vacuum tank filled with water, was installed on the carriage and was towed through the water. The test apparatus hence simulated a step current, with a uniform flow past the lower part of the riser and no flow elsewhere. The particulars of the riser model and the experimental set-up are given in Table 5.2 and Figure 5.8, respectively.

Table 5.2: Particulars in the Delft VIV tests (Chaplin et al., 2005b)

| Parameter | Value |
|---|---|
| Diameter (mm) | 28 |
| Total length (m) | 13.12 |
| Dry weight per unit length (kg/m) | 1.47 |
| Wet weight per unit length (N/m) | 12.1 |
| Mass ratio | 3 |
| EI (N-m$^2$) | 29.88 |
| $Re$ range | $2,500 - 25,000$ |
| Boundary conditions | both ends hinged |

In the model tests, the riser was hinged by universal joints at both ends. Additionally, a tensioning system was connected to the top end to change the initial tension in order to achieve different still water fundamental nature frequencies. In the present simulation, the pre-tension was attained by stretching the riser into the bottom before applying an incoming flow in the static analysis. The numerical model and the global coordinate system are schematized in Figure 5.9. $z$ is defined as the vertical coordinate with positive values above the calm water surface in the global Cartesian system, and $L$ is the overall length of the riser. Nondimensional vertical distance was obtained by dividing $z$ with the water depth.
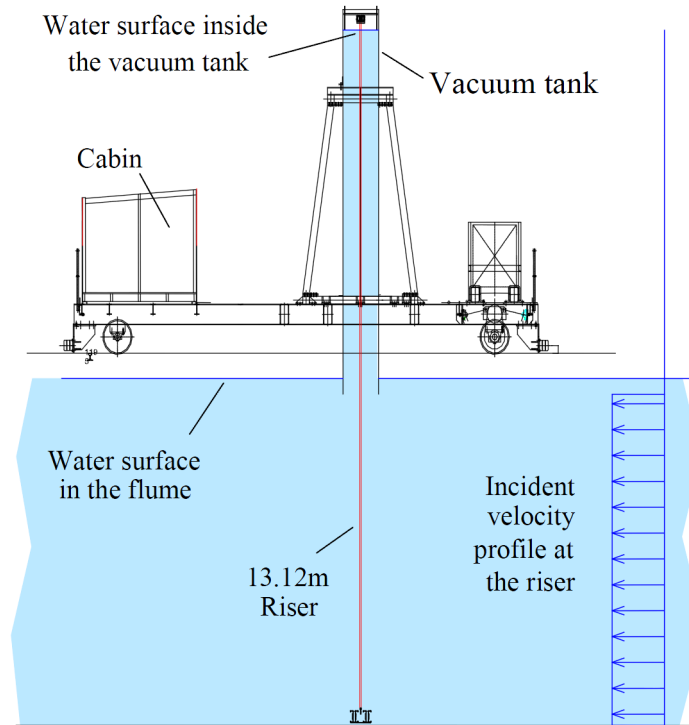
Figure 5.8: Set-up of the Delft VIV tests (from Chaplin et al. (2005a))
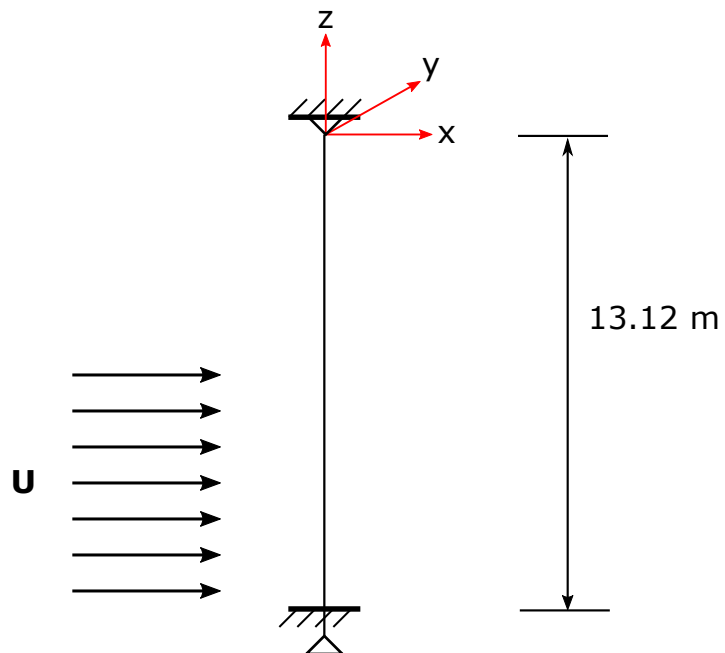


Figure 5.9: Numerical model set-up for the Delft VIV tests (Chaplin et al., 2005a)

Four cases were examined, which are corresponding to four current speeds and four initial top tensions as given in Table 5.3. All the simulations given by the present model started from the static equilibrium positions with zero initial velocities.

Table 5.3: Simulation scenarios for the Delft VIV tests (Chaplin et al., 2005a)

| Case no. | Current speed (m/s) | Initial top tension (N) |
|----------|---------------------|-------------------------|
| 1        | 0.16                | 405                     |
| 3        | 0.31                | 457                     |
| 6        | 0.60                | 670                     |
| 9        | 0.95                | 1002                    |

For each case, time series of the transverse motions at $z = -0.25L$, $z = -0.5L$ and $z = -0.75L$ ($z = 0$ is at the calm water surface), the riser profiles at different time instants, and the cross-flow vibration envelope are presented. The vibration envelopes were obtained by using the maximum and minimum displacements at each node over the simulation duration (300 sec). Note that all the presented displacements were nondimensionalized with respect to the diameter of the riser.

The predicted envelopes were compared to the experimental results (Chaplin et al., 2005b) and the numerical solutions by SHEAR7, Norsk Hydro, and Ma et al. (2014). Note that Norsk Hydro predicts VIV by coupling the computation of the hydrodynamic forces on 2-D planes using CFD with a finite element structural code (Herfjord et al., 1999). In the work of Ma et al. (2014), all the results were obtained using 200 elements and a time step of 0.0025 sec. The results by SHEAR7 and Norsk Hydro were taken from the work by Chaplin et al. (2005a).

## 5.2.1 Results for Case 1

Convergence studies have been carried out for Case 1 by using various numbers of elements, 12, 24, 48, 60 and 72 and a number of time steps (0.0002 sec, 0.0001 sec

and 0.00005 sec). Figure 5.10 presents the convergence of predicted envelope to the number of elements using the time step of 0.0001 sec for a current velocity of 0.16 m/s. It can be observed that the solutions converge as the number of elements was increased. Figure 5.11 presents the convergence of the predicted envelope for the same current velocity with respect to the time step using 24 elements. It can be seen that the numerical prediction is insensitive to the time step. In the following figures, the results were based on 72 elements and the time step of 0.0001 sec.
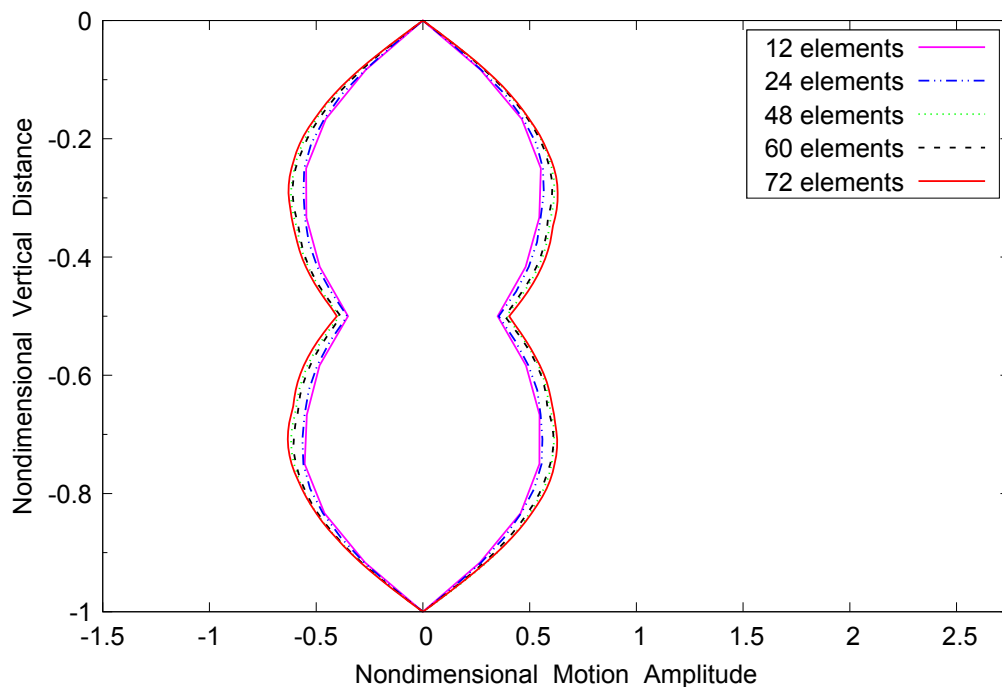


Figure 5.10: Case 1 – Convergence of predicted riser envelope to the number of elements

Figures 5.12, 5.13, and 5.14 present the time series of the transverse displacements at the midpoint, $z = -0.25L$, and $z = -0.75L$, respectively. From these figures, it can be seen that the motions include different frequency components. The steady state was reached after a transient period. The corresponding riser profiles at different time instants are presented in Figure 5.15.
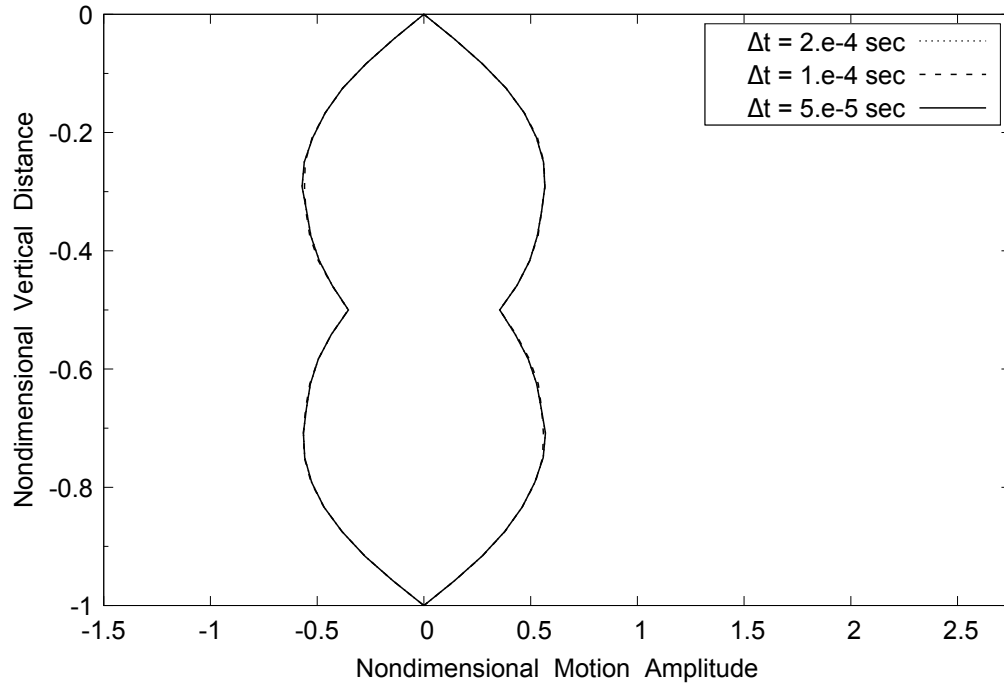
Figure 5.11: Case 1 – Convergence of predicted riser envelope to the time step
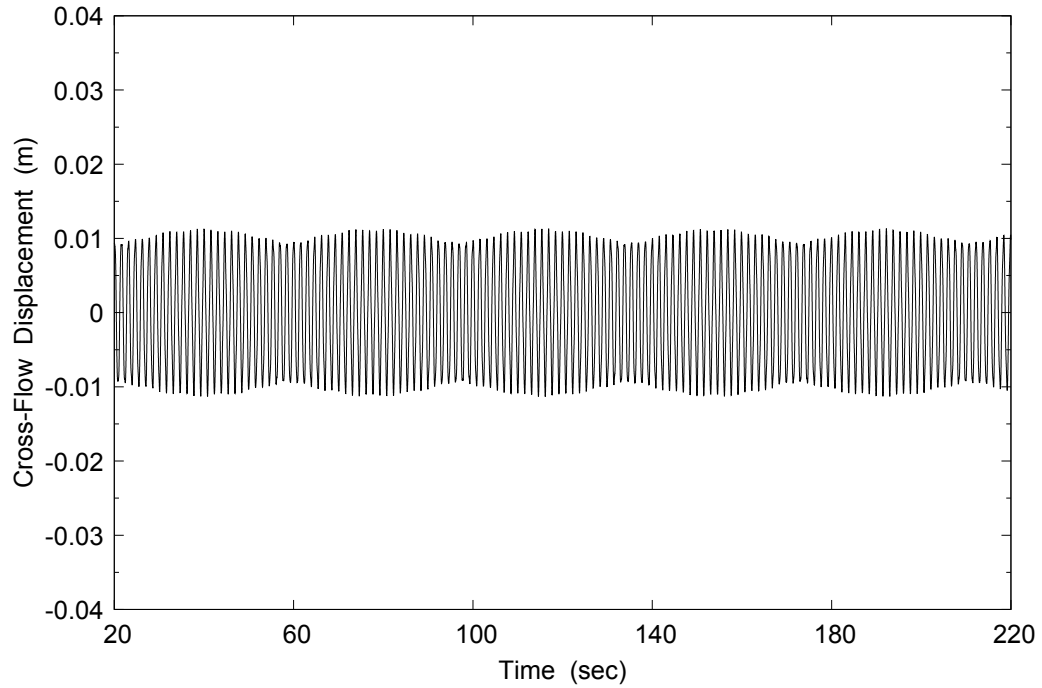


Figure 5.12: Case 1 – Time series of cross-flow motion at the midpoint
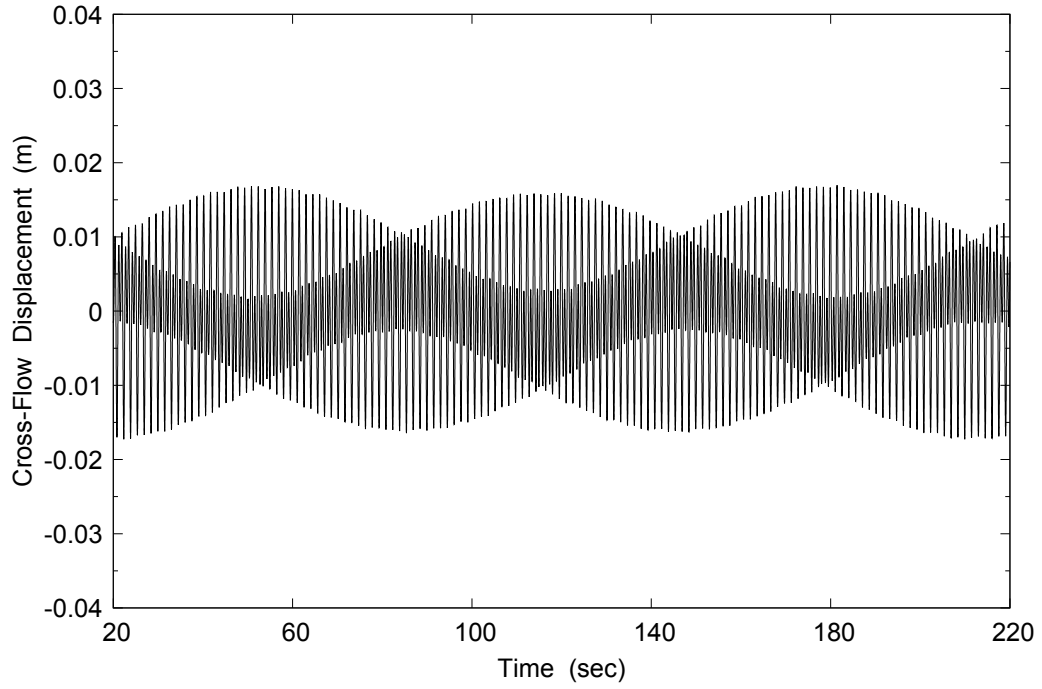
Figure 5.13: Case 1 – Time series of cross-flow motion at $z = -0.25L$
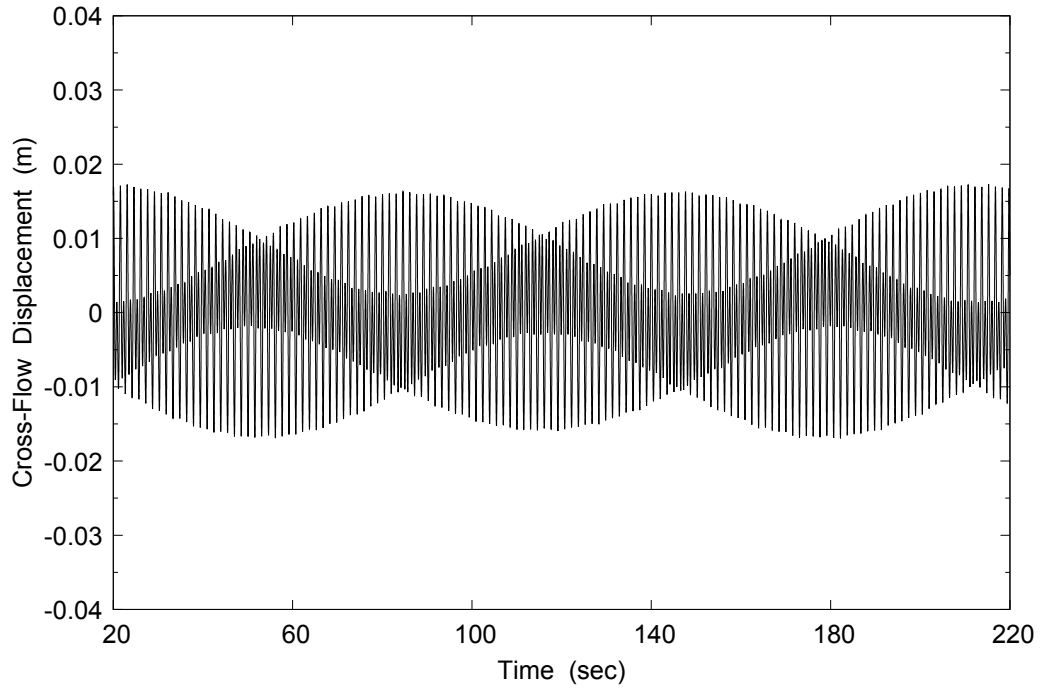


Figure 5.14: Case 1 – Time series of cross-flow motion at $z = -0.75L$
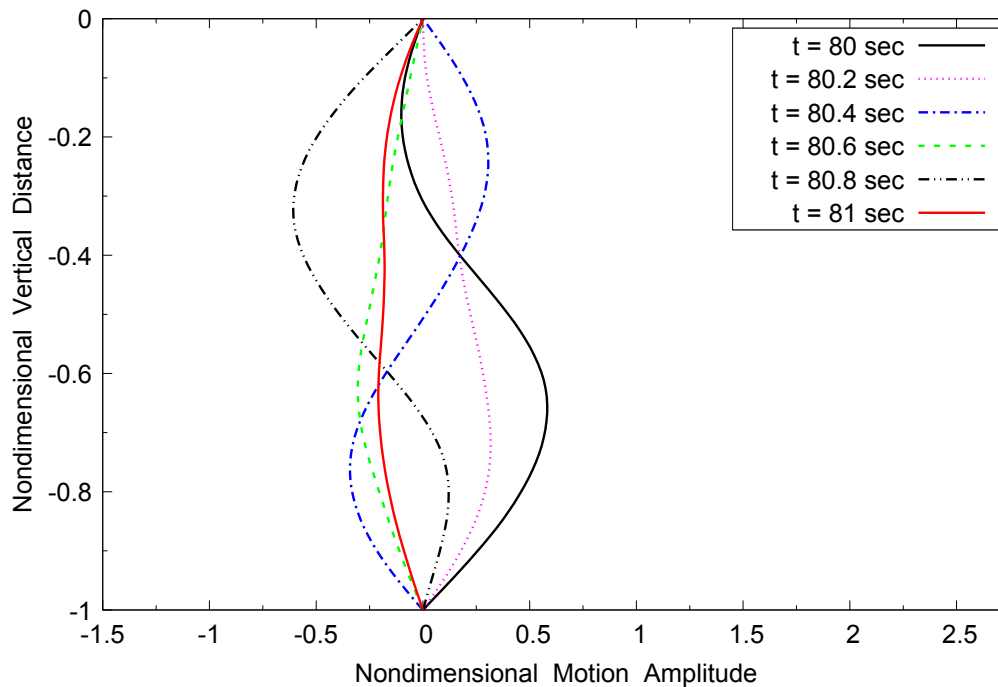
Figure 5.15: Case 1 – Riser profiles at different time instants

The comparison of the envelope predicted by the present model, the experimental measurement, and those by SHEAR7, Norsk Hydro, and by Ma et al. (2014) is given in Figure 5.16. The modal shapes were not captured in the work by Ma et al. (2014) and by Norsk Hydro. The prediction by the present model is in a reasonable agreement with the experimental measurement.
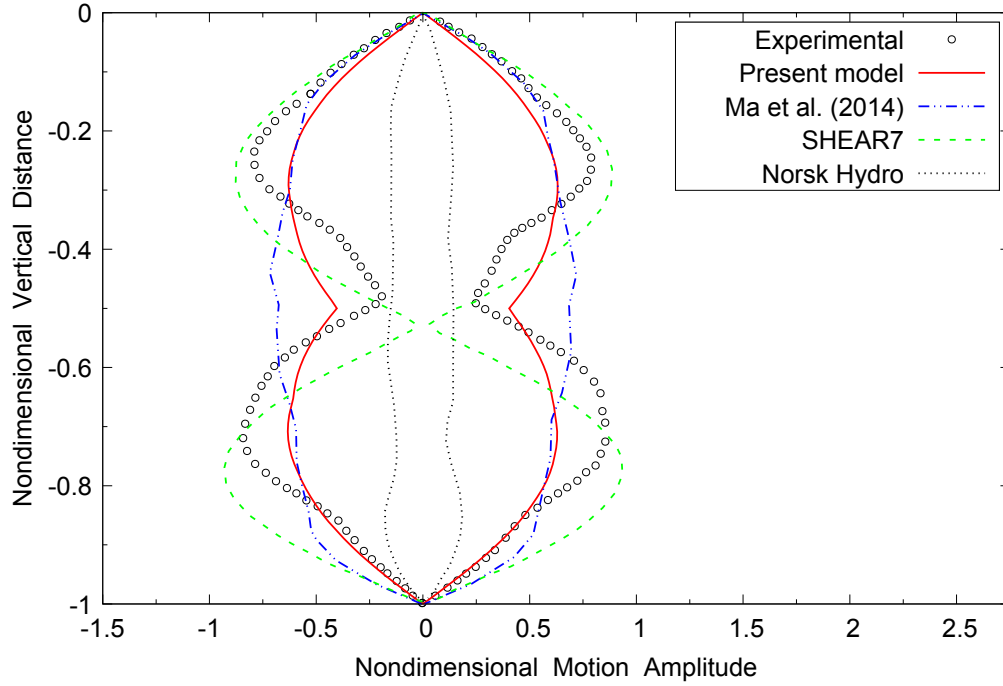
Figure 5.16: Case 1 – Comparison of cross-flow vibration envelope

## 5.2.2 Results for Case 3

Convergence studies have been carried out for Case 3 by using various numbers of elements, 12, 24, 48, 60 and 72 and a number of time steps (0.0002 sec, 0.0001 sec and 0.00005 sec). Figure 5.17 presents the convergence of predicted envelope to the number of elements using the time step of 0.0001 sec for a current velocity of 0.31 m/s. It can be observed that the solutions converge as the number of elements was increased. Figure 5.18 presents the convergence of the predicted envelope for the same current velocity with respect to the time step using 24 elements. It can be seen that the numerical prediction is insensitive to the time step. In the following figures, the results were based on 72 elements and the time step of 0.0001 sec.

Figures 5.19, 5.20, and 5.21 present the time series of the transverse displacements at the midpoint, $z = -0.25L$, and $z = -0.75L$, respectively. The riser profiles at
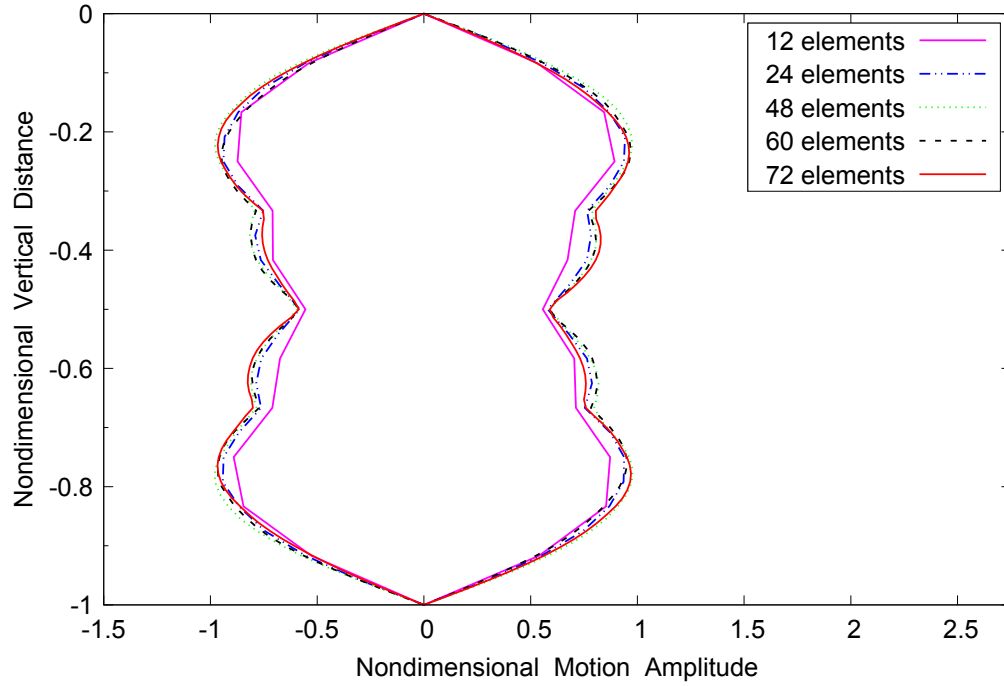
Figure 5.17: Case 3 – Convergence of predicted riser envelope to the number of elements
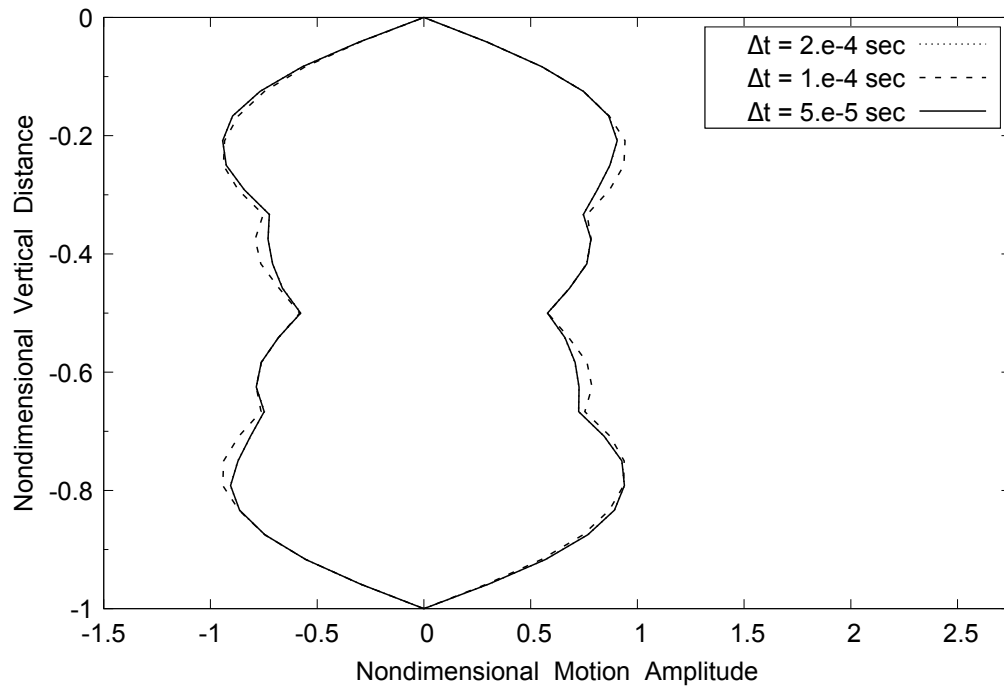


Figure 5.18: Case 3 – Convergence of predicted riser envelope to the time step

different time instants are presented in Figure 5.22.
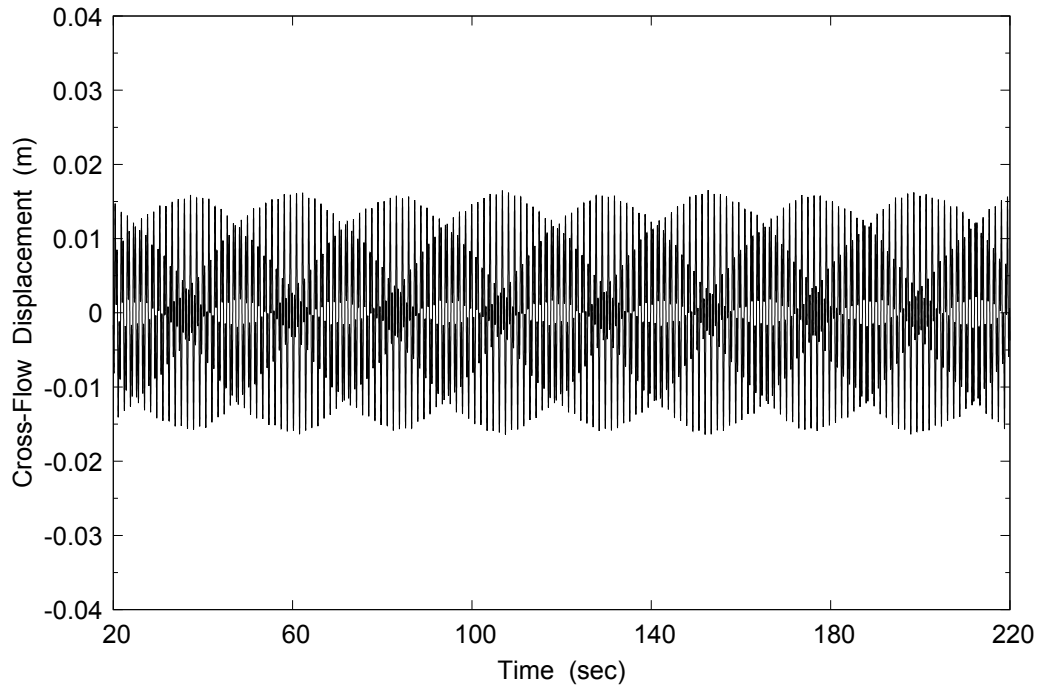


Figure 5.19: Case 3 – Time series of cross-flow motion at the midpoint

The comparison of the predicted and experimental envelopes is given in Figure 5.23. The present model overpredicted the responses. It is likely due to the fact that the hydrodynamic coefficient database used in the computations corresponds to the high Reynolds number, while the riser was subjected to a low Reynolds number in the tests. As discussed in Chapter 2, the hydrodynamic coefficients differ in many characteristics across different $Re$ regimes.
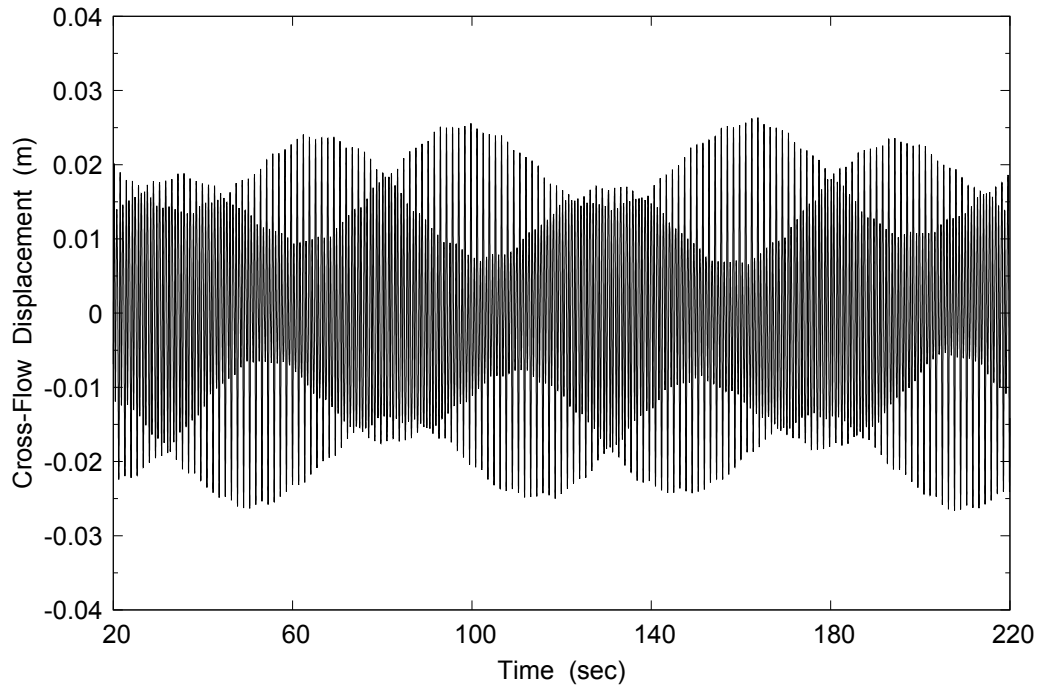
Figure 5.20: Case 3 – Time series of cross-flow motion at $z = -0.25L$
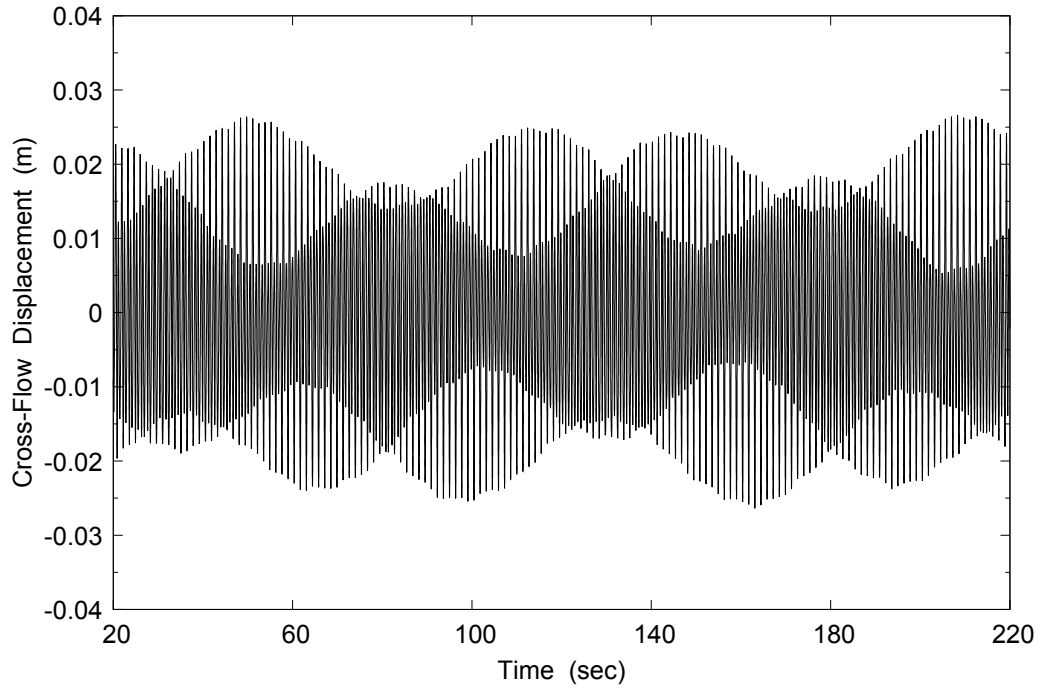


Figure 5.21: Case 3 – Time series of cross-flow motion at $z = -0.75L$
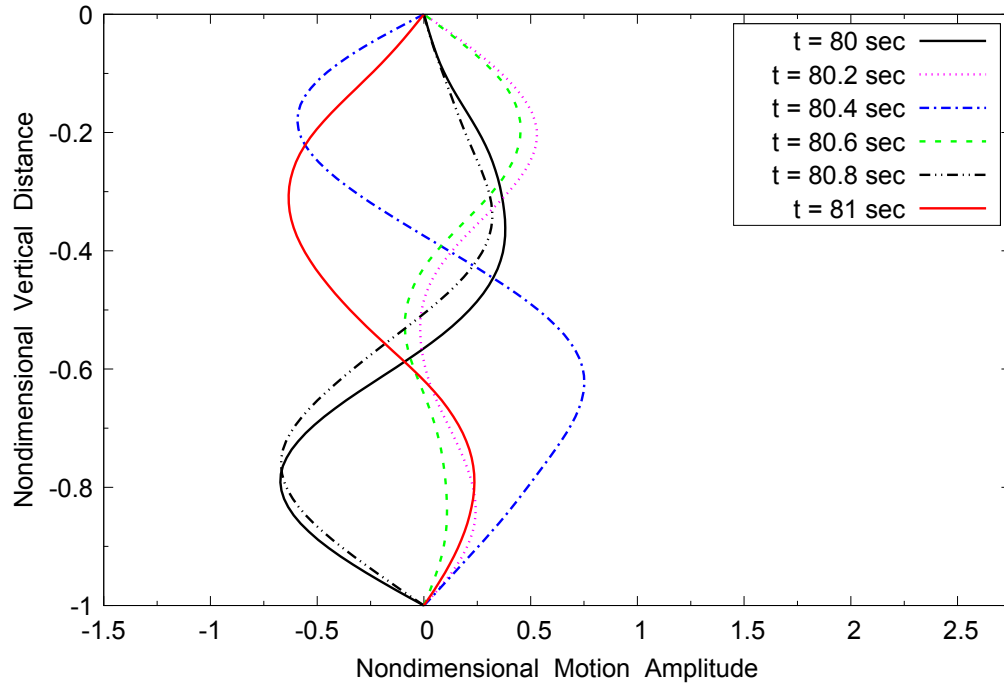
Figure 5.22: Case 3 – Riser profiles at different time instants
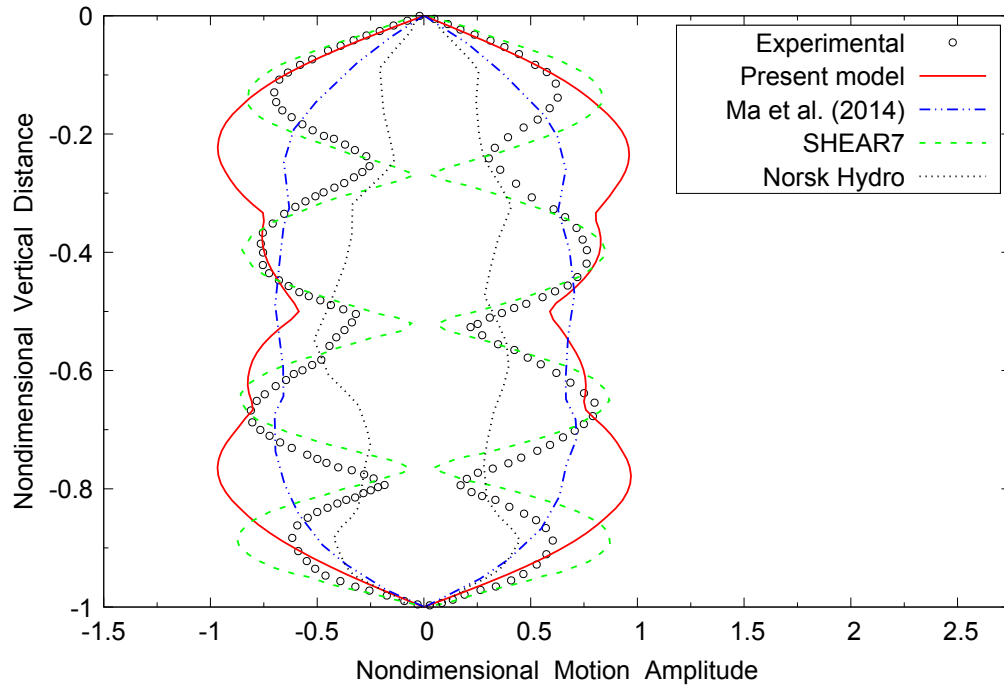


Figure 5.23: Case 3 – Comparison of cross-flow vibration envelope

### 5.2.3 Results for Case 6

Convergence studies have been carried out for Case 6 by using various numbers of elements, 12, 24, 48, 60 and 72 and a number of time steps (0.0002 sec, 0.0001 sec and 0.00005 sec). Figure 5.24 presents the convergence of predicted envelope to the number of elements using the time step of 0.0001 sec for a current velocity of 0.6 m/s. It can be observed that the solutions converge as the number of elements was increased. Figure 5.25 presents the convergence of the predicted envelope for the same current velocity with respect to the time step using 24 elements. It can be seen that the numerical prediction is insensitive to the time step. In the following figures, the results were based on 72 elements and the time step of 0.0001 sec.
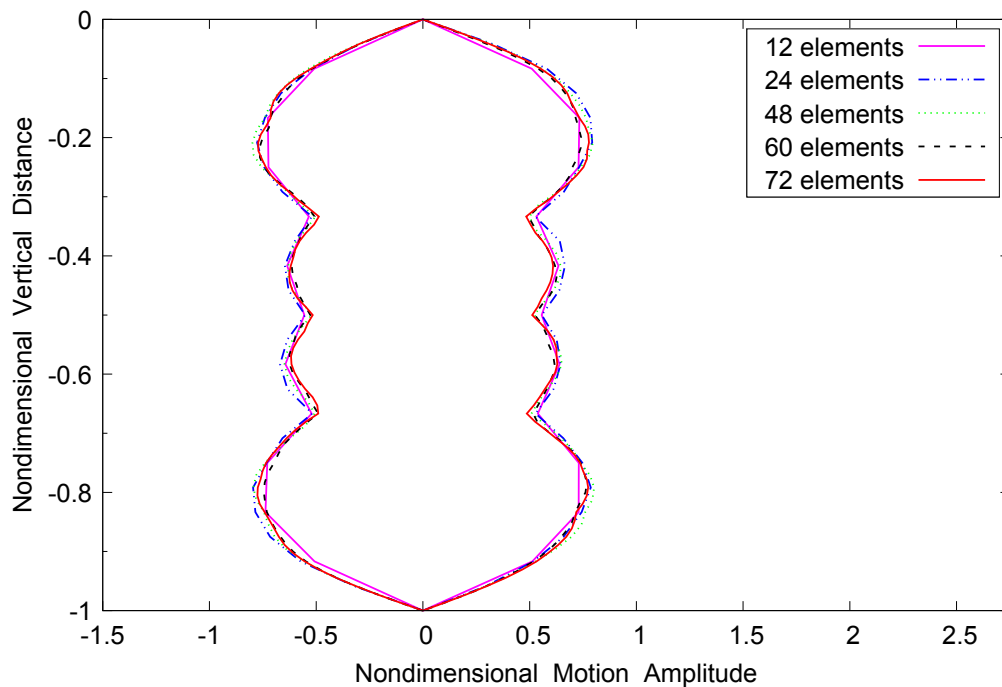


Figure 5.24: Case 6 – Convergence of predicted riser envelope to the number of elements

Figures 5.26, 5.27, and 5.28 present the time series of the transverse displacements at the midpoint, $z = -0.25L$, and $z = -0.75L$, respectively. Different frequency com-
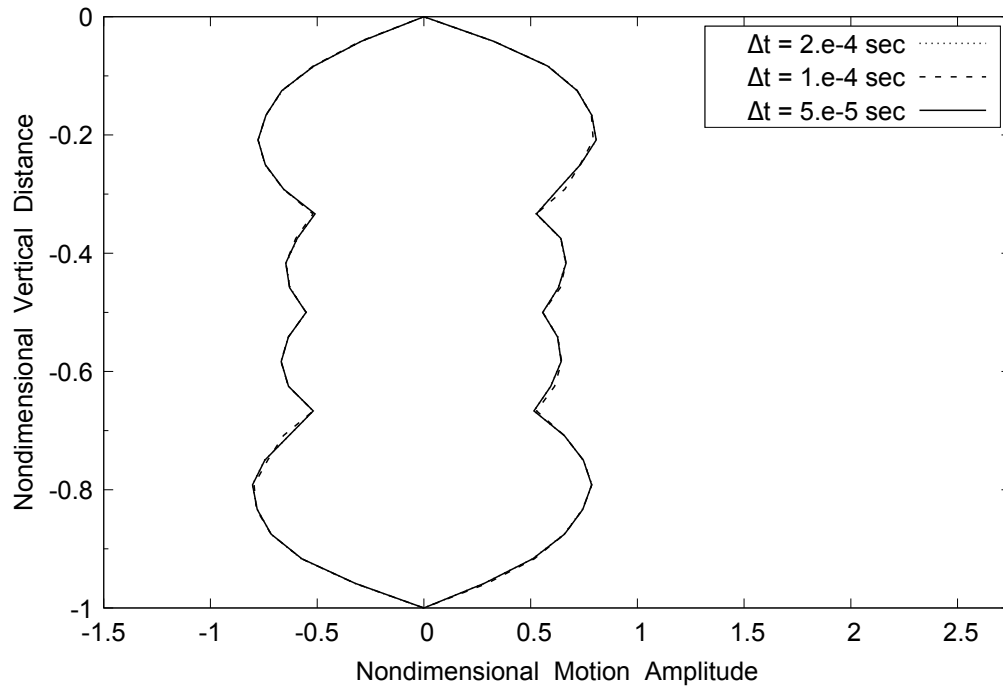
Figure 5.25: Case 6 – Convergence of predicted riser envelope to the time step

ponents can be observed in the time series. A steady state was reached after a transient period. The riser profiles at different time instants are presented in Figure 5.29.

The comparison of the envelopes with other results is given in Figure 5.30. Similar observation can be obtained to that in Case 3.
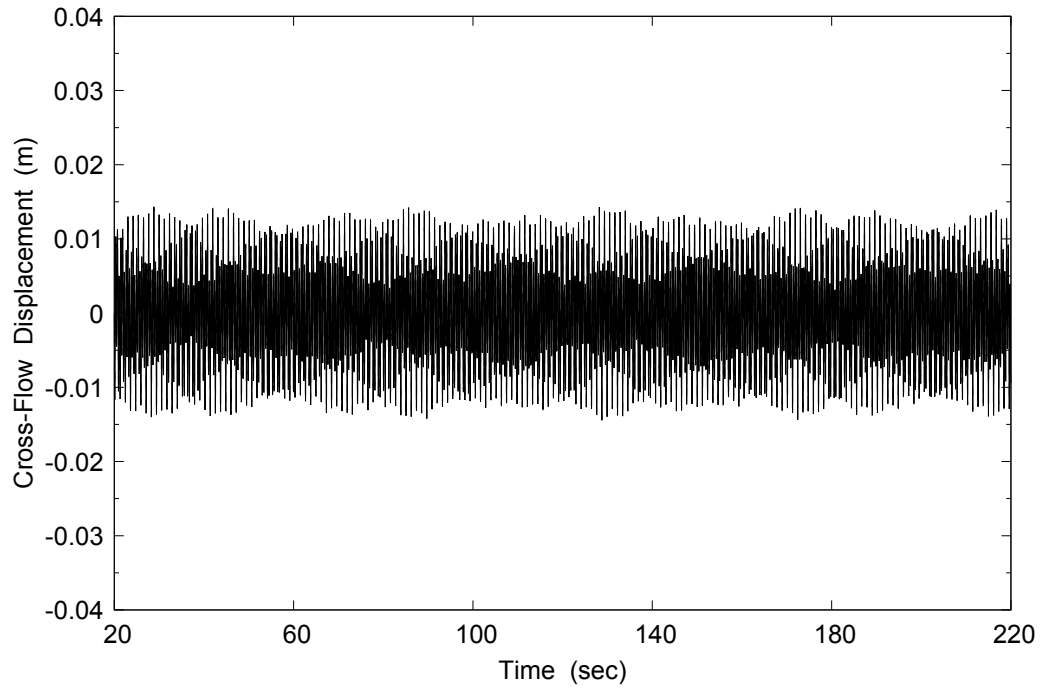
Figure 5.26: Case 6 – Time series of cross-flow motion at the midpoint
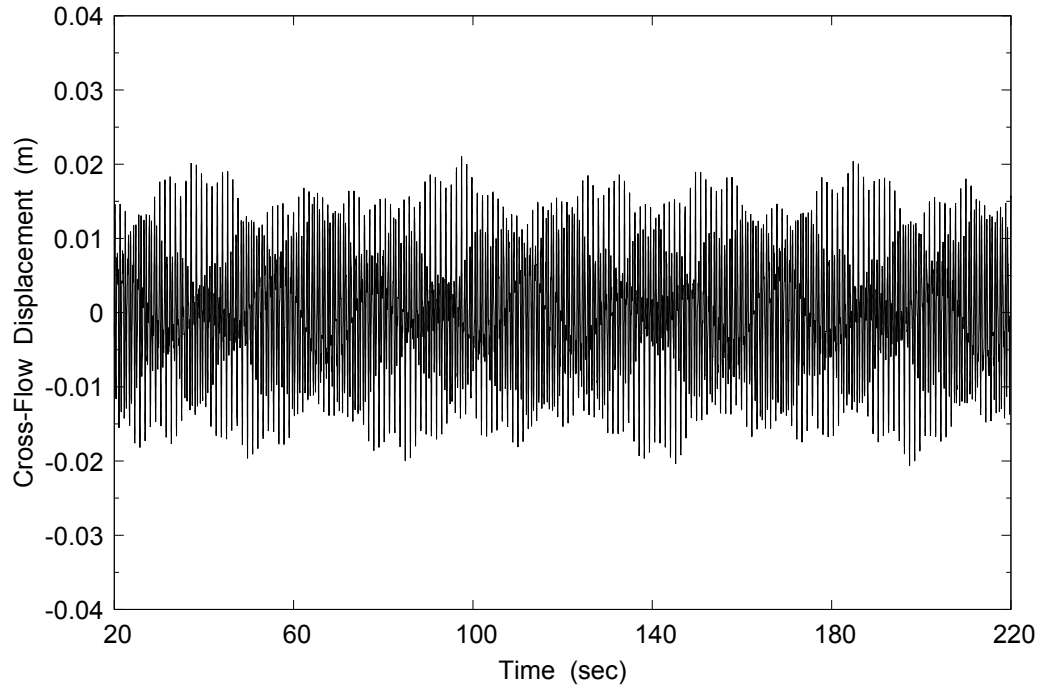


Figure 5.27: Case 6 – Time series of cross-flow motion at $z = -0.25L$
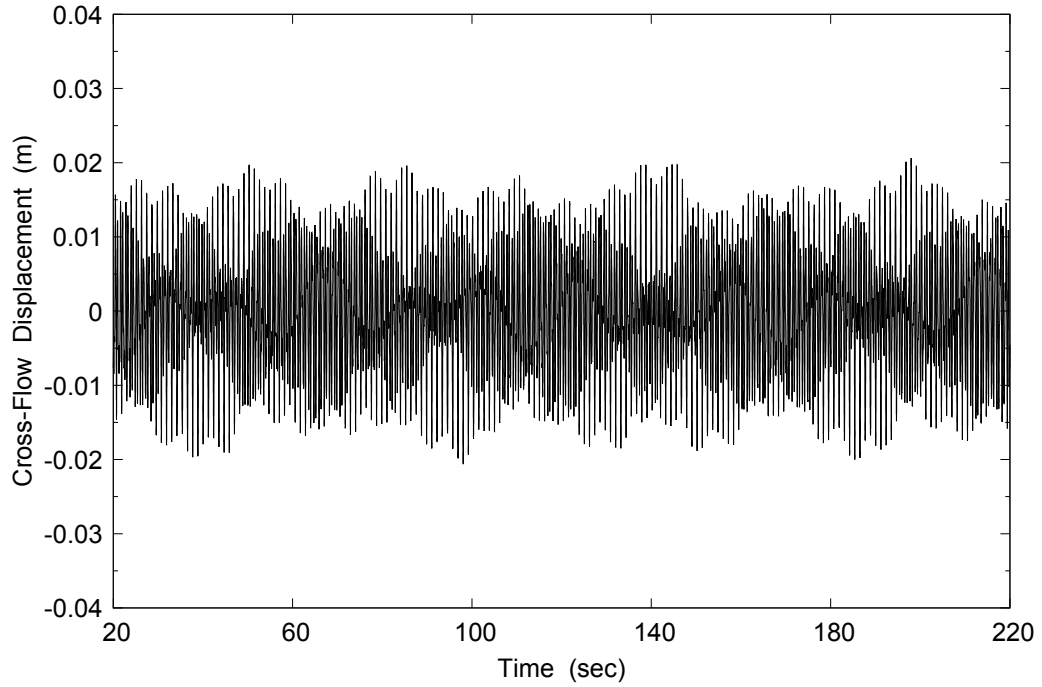
Figure 5.28: Case 6 – Time series of cross-flow motion at $z = -0.75L$
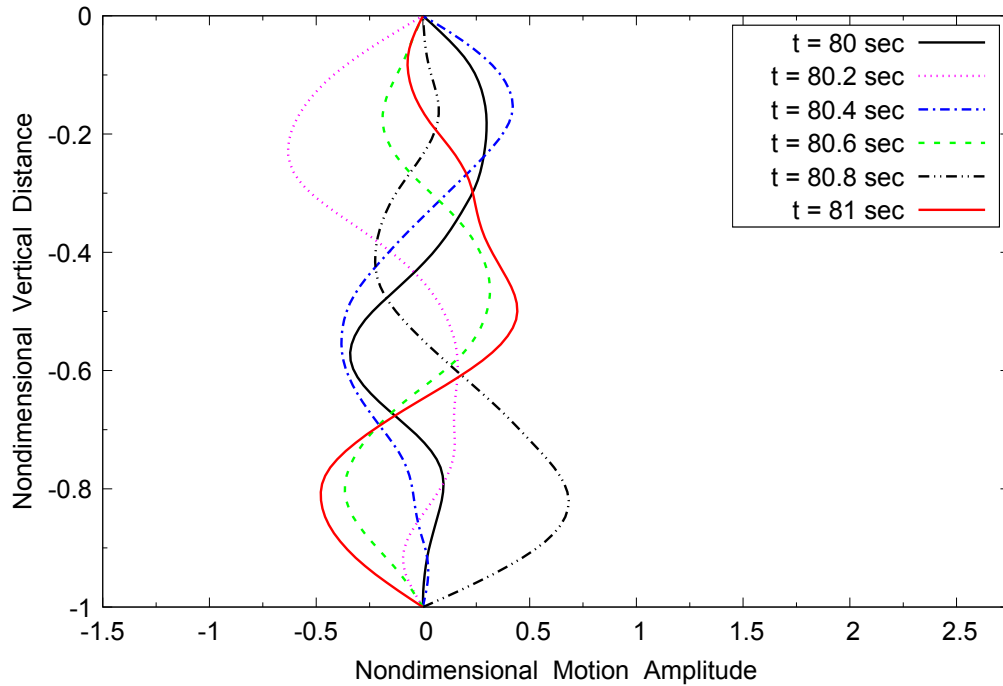


Figure 5.29: Case 6 – Riser profiles at different time instants
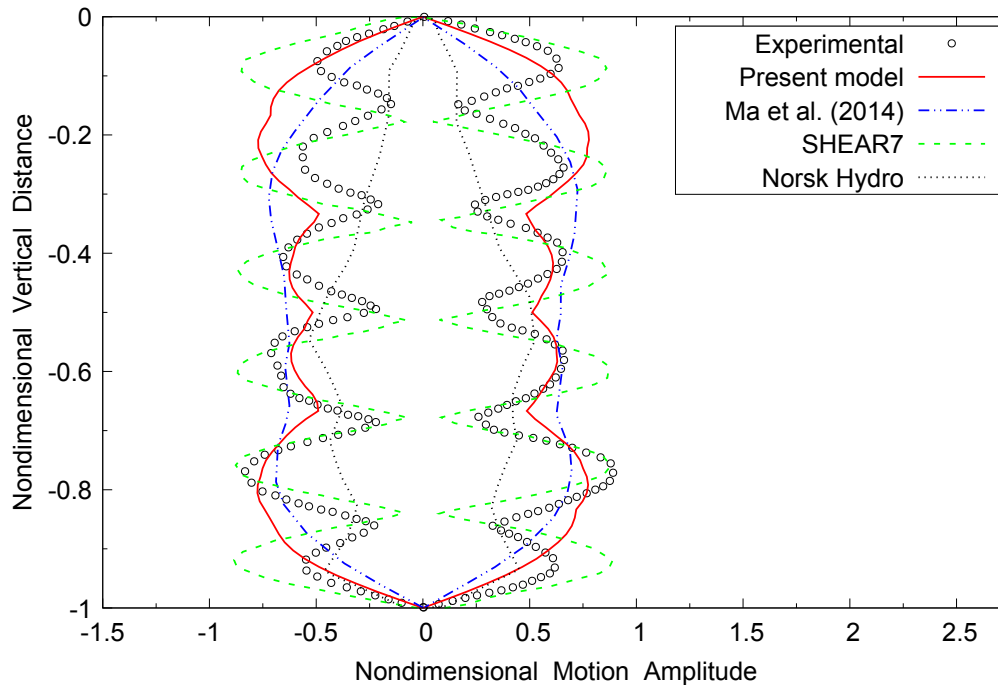
Figure 5.30: Case 6 – Comparison of cross-flow vibration envelope

## 5.2.4 Results for Case 9

Convergence studies have been carried out for Case 9 by using various numbers of elements, 12, 24, 48, 60 and 72 and a number of time steps (0.0002 sec, 0.0001 sec and 0.00005 sec). Figure 5.31 presents the convergence of predicted envelope to the number of elements using the time step of 0.0001 sec for a current velocity of 0.95 m/s. It can be observed that the solutions converge as the number of elements was increased. Figure 5.32 presents the convergence of the predicted envelope for the same current velocity with respect to the time step using 24 elements. It can be seen that the numerical prediction is insensitive to the time step. In the following figures, the results were based on 72 elements and the time step of 0.0001 sec.

Time series of the transverse displacements at the midpoint, $z = -0.25L$, and $z = -0.75L$ are presented in Figures 5.33, 5.34, and 5.35, respectively. The riser
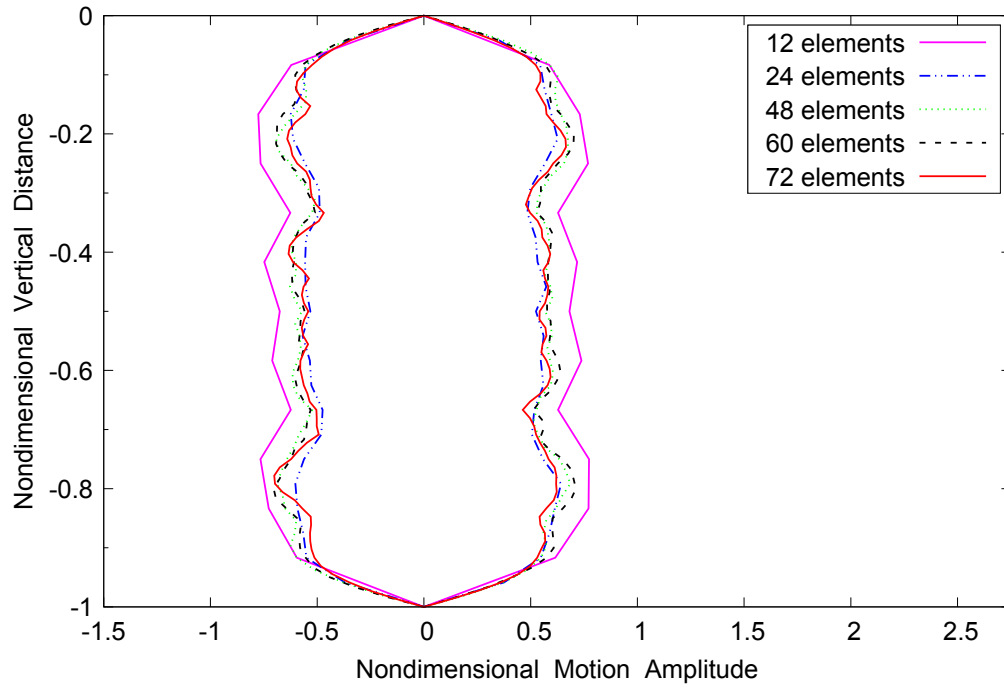
Figure 5.31: Case 9 – Convergence of predicted riser envelope to the number of elements
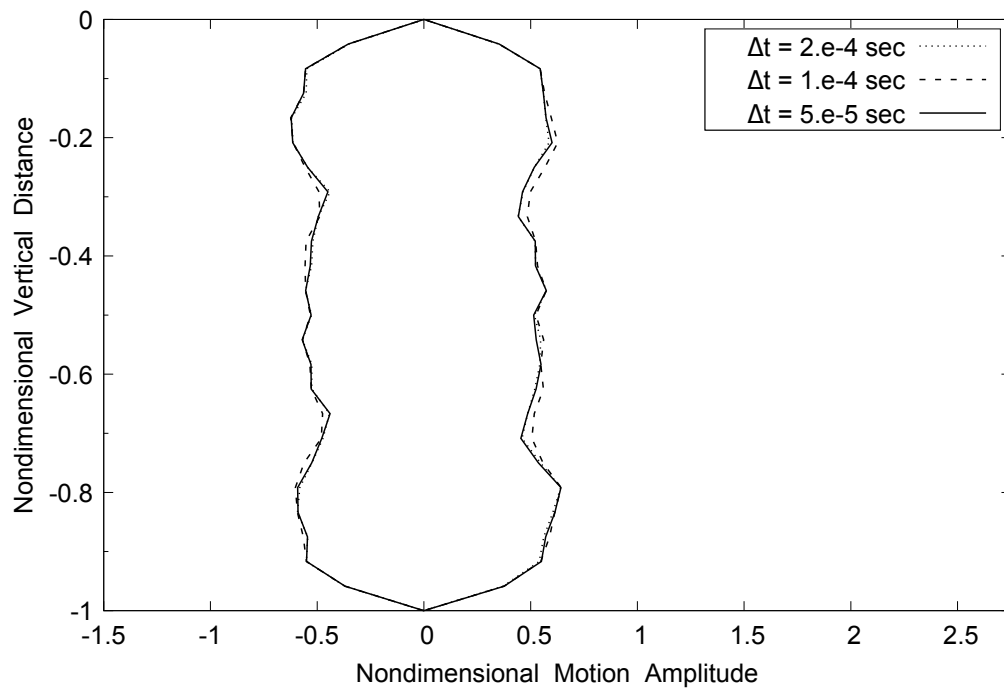


Figure 5.32: Case 9 – Convergence of predicted riser envelope to the time step

profiles at different time instants are presented in Figure 5.36.
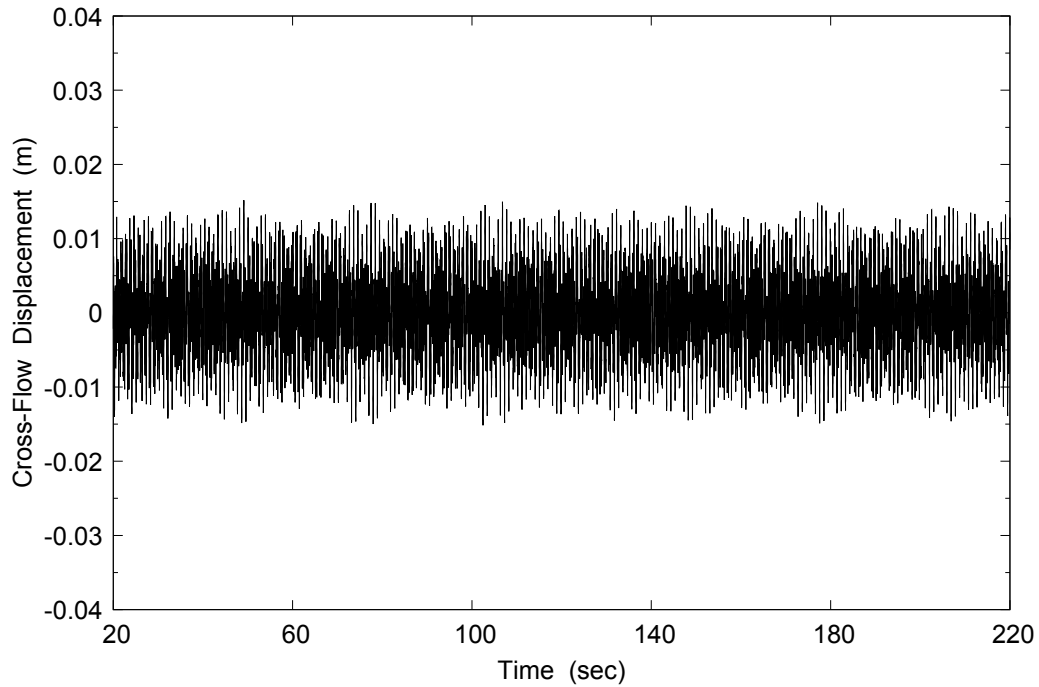


Figure 5.33: Case 9 – Time series of cross-flow motion at the midpoint

Figure 5.37 presents the comparison of the experimental envelope and those by the present method, SHEAR7, Norsk Hydro, and Ma et al. (2014). The previous method by Ma et al. (2014) was not able to capture the modal shapes. The present model can capture the lower modes compared to the experimental measurement but with an underprediction. This may be due to the issue associated with different *Re*. It should be also noted that a loose ball joint at the top or bottom of the riser resulted in decreased stiffness of the system (Chaplin et al., 2005b). This stiffness decrease could lead to higher vibration amplitudes.
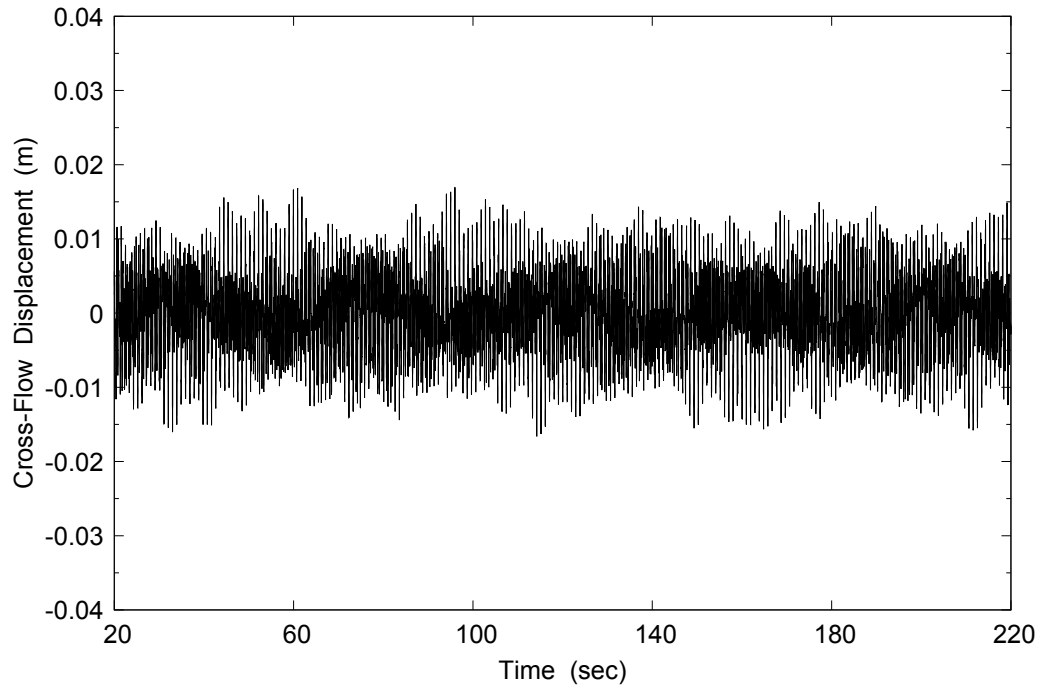
Figure 5.34: Case 9 – Time series of cross-flow motion at $z = -0.25L$
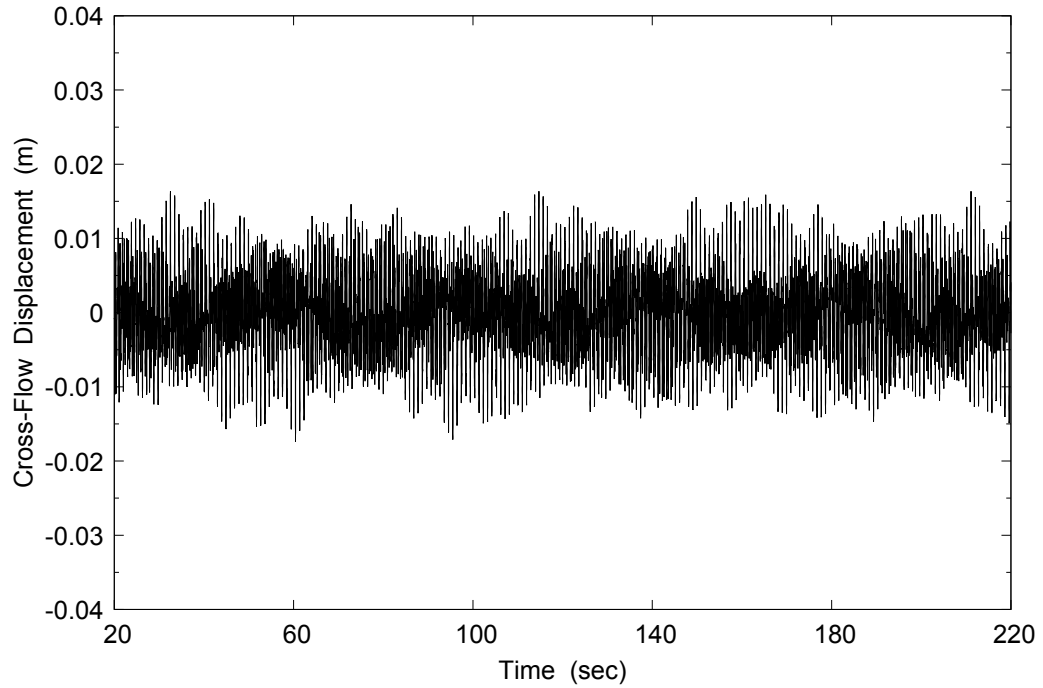


Figure 5.35: Case 9 – Time series of cross-flow motion at $z = -0.75L$
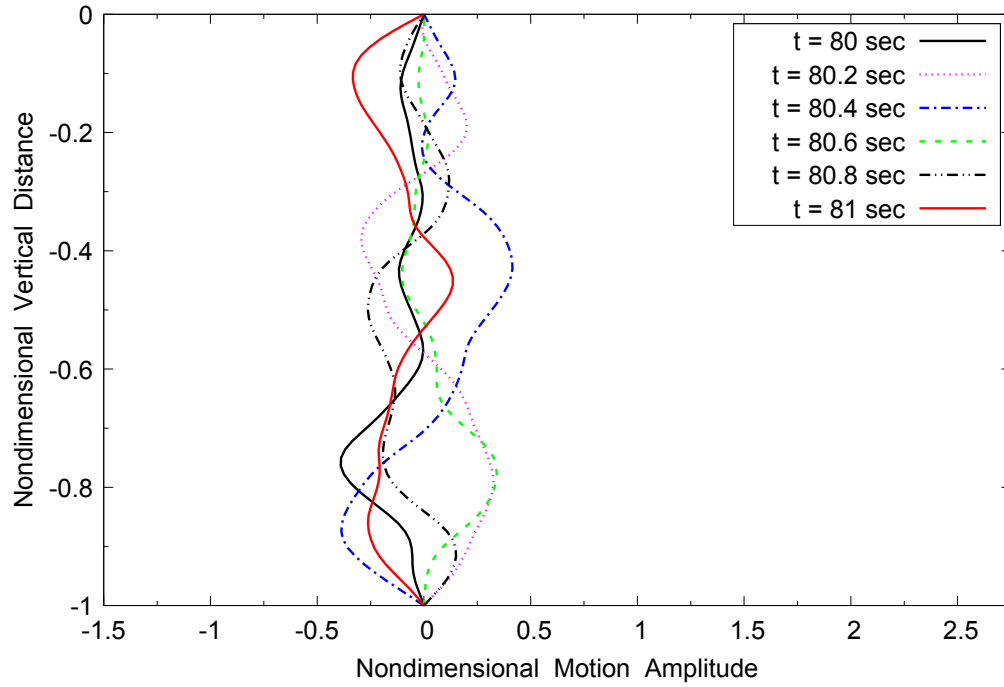
Figure 5.36: Case 9 – Riser profiles at different time instants
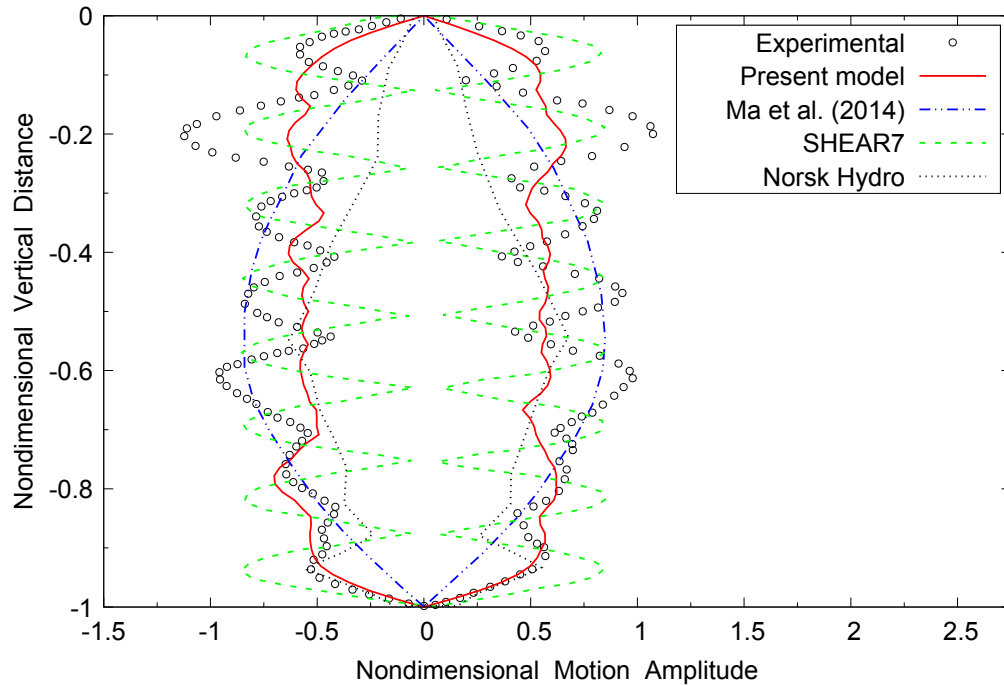


Figure 5.37: Case 9 – Comparison of cross-flow vibration envelope

# Chapter 6

# Conclusions and Recommendations for Future Work

In this thesis, a time-domain model was further developed to predict the vortex-induced vibration (VIV) of marine risers. The structural motion was identified by two nondimensional state variables: amplitude ratio and reduced velocity. Through a zero up-crossing analysis of the cross-flow displacement, the two state variables were obtained to interpolate the hydrodynamic coefficients from a database, which is based on forced oscillation tests of a full-scale riser segment at high Reynolds numbers. Different interpolation methods were investigated, and the study indicated that other higher-order interpolation methods did not lead to better results than those by bilinear interpolation. The interpolated coefficients were then employed to calculate the hydrodynamic forces exerted on the riser.

The VIV correlation along the riser span was assumed by the adjacent elements sharing the motion and forcing characteristics at the common node. For each element, the characteristics at both end nodes were obtained from the progressive zero up-crossing analysis and used in the time-domain computation. The hydrodynamic

excitation and damping were considered inclusively in the lift coefficient in phase with velocity.

The VIV prediction of marine risers were performed by incorporating the time-domain model with MAPS-Mooring, a global-coordinate-based finite element method (FEM) program. The FEM analysis consists of two parts: the riser profile under static equilibrium is first obtained based on a Newton iterative method, and the dynamic response and the tension of the riser are then integrated in the time domain. In the present studies, different time integration schemes were examined for the dynamic analysis of MAPS-Mooring. No improvement was found by using other integration schemes when compared to the original one: a second-order semi-implicit Adams method.

The FEM program was first validated by the mooring line experiments identified in the literature. It was proven to be reliable and robust. Validation studies were then carried out to the FEM scheme with the present VIV model integrated. The current model was applied to predict a rigid riser vibrating transversely to a uniform flow and a top-tensioned flexible riser under VIV in a step current. For the single-mode VIV case, good agreement in nondimensional motion amplitude was observed between the numerical results and the experimental measurements. For the multi-mode VIV case, the lower mode shapes can be captured by the present model and the predicted cross-flow motions were in reasonable agreement with the experimental measurements.

**Recommendations for Future Work**

The present model should be further validated by additional benchmark cases. The model may also be utilized to predict the behaviours of risers with VIV suppression devices by interpolating hydrodynamic coefficients collected from tests in which riser

models are fitted with VIV suppression devices.

A combined frequency-time-domain approach based on the current model may capture the higher harmonics. The present model predicts VIV from one cycle to the next in the time domain; however, the motion cycles further backwards might contain more information on the hydrodynamic forces. Hence, a progressive Fast-Fourier-Transformation analysis of the past multiple cycles could reveal higher frequency components of the external forces, which may be included into the equation of motion.

The present model couples the in-line and cross-flow motions based on force coefficients obtained from pure transverse forced oscillation tests. Allowing the second degree-of-freedom (DOF) would lead to force coefficients different from those obtained from single-mode vibration. In order to better predict 2-DOF VIV, a more sophisticated model needs to be developed. In addition, it is desirable to conduct pure-in-line and coupled-in-line-cross-flow forced oscillation tests to deduce respective hydrodynamic coefficient databases.

Furthermore, the proposed model may be combined with a wake model to predict the VIV interaction and wake-induced oscillation (WIO) between multiple risers. Such wake models empirically describe the wake velocity field of a cylinder. Therefore, the motions of the downstream risers may be simulated based on the current VIV model along with the approximate incoming current velocities at the trajectories of the risers.

# Bibliography

Akima, H. (1978). A Method of Bivariate Interpolation and Smooth Surface Fitting for Irregularly Distributed Data Points. *ACM Transactions on Mathematical Software*, 4(2):148–159.

Anand, N. (1985). *Free Span Vibrations of Submarine Pipelines in Steady and Wave Flows.* PhD thesis, Norwegian Institute of Technology, Trondheim, Norway.

Blevins, R. D. (1990). *Flow-Induced Vibration.* Van Nostrand Reinhold Co., Inc.; New York, NY, USA.

Bridge, C., Willis, N., Sworn, A., and De Wilde, J. (2005). Development of SHEAR7 Lift Curves for VIV Analysis and Application to Single Pipe and Bundle Risers. In *Proceedings of the Offshore Technology Conference.* Offshore Technology Conference.

Chakrabarti, S. (2005). *Handbook of Offshore Engineering.* Elsevier.

Chaplin, J., Bearman, P., Cheng, Y., Fontaine, E., Graham, J., Herfjord, K., Huera Huarte, F., Isherwood, M., Lambrakos, K., Larsen, C., Meneghini, J., Moe, G., Pattenden, R., Triantafyllou, M., and Willden, R. (2005a). Blind Predictions of Laboratory Measurements of Vortex-Induced Vibrations of a Tension Riser. *Journal of Fluids and Structures*, 21(1):25–40.

Chaplin, J., Bearman, P., Huera Huarte, F., and Pattenden, R. (2005b). Laboratory Measurements of Vortex-Induced Vibrations of a Vertical Tension Riser in a Stepped Current. *Journal of Fluids and Structures*, 21(1):3–24.

Chen, X. (2002). *Studies on Dynamic Interaction Between Deep-Water Floating Structures and Their Mooring/Tendon Systems*. PhD thesis, Texas Agricultural and Mechanical University.

Dahl, J. J. M. (2008). *Vortex-Induced Vibration of a Circular Cylinder with Combined In-Line and Cross-Flow Motion*. PhD thesis, Massachusetts Institute of Technology.

Ding, Z., Balasubramanian, S., Lokken, R., and Yung, T. (2004). Lift and Damping Characteristics of Bare and Straked Cylinders at Riser Scale Reynolds Numbers. In *Proceedings of the Offshore Technology Conference*. Offshore Technology Conference.

Finn, L., Lambrakos, K., and Maher, J. (1999). Time Domain Prediction of Riser VIV. In *Proceedings of the Fourth International Conference on Advances in Riser Technologies, Aberdeen, Scotland*.

Fylling, I., Larsen, C., Sødahl, N., Ormberg, H., Engseth, A., Passano, E., and Holthe, K. (1995). RIFLEX – Theory Manual. *SINTEF Report STF70 F95219*.

Garrett, D. (1982). Dynamic Analysis of Slender Rods. *Journal of Energy Resources Technology*, 104(4):302–306.

Gerrard, J. (1966). The Mechanics of the Formation Region of Vortices Behind Bluff Bodies. *Journal of Fluid Mechanics*, 25(02):401–413.

Gopalkrishnan, R. (1993). *Vortex-Induced Forces on Oscillating Bluff Cylinders*. PhD thesis, Massachussets Institute of Technology.

Herfjord, K., Drange, S., and Kvamsdal, T. (1999). Assessment of Vortex-Induced Vibrations on Deepwater Risers by Considering Fluid-Structure Interaction. *Journal of Offshore Mechanics and Arctic Engineering*, 121:207–212.

Hover, F., Techet, A., and Triantafyllou, M. (1998). Forces on Oscillating Uniform and Tapered Cylinders in Crossflow. *Journal of Fluid Mechanics*, 363(1):97.

ISSC (1997). *Proceedings of the 13th International Ship and Offshore Structures Congress: Report of Committee I.2-Loads*, volume 1. Elsevier.

Johanning, L., Smith, G. H., and Wolfram, J. (2007). Measurements of Static and Dynamic Mooring Line Damping and Their Importance for Floating WEC Devices. *Ocean Engineering*, 34(14):1918–1934.

Larsen, C. (2000). Empirical VIV Models. In *Workshop on Vortex-Induced Vibrations (VIV) of Offshore Structures. São Paulo, Brazil.*

Lie, H. (1995). A Time Domain Model for Simulation of Vortex Induced Vibrations on a Cable. *Flow Induced Vibration*, pages 455–466.

Ma, P., Qiu, W., and Spencer, D. (2014). Numerical Vortex-Induced Vibration Prediction of Marine Risers in Time-Domain Based on a Forcing Algorithm. *Journal of Offshore Mechanics and Arctic Engineering*, 136(3):031703.

Mainçon, P. (2011). A Wiener-Laguerre Model of VIV Forces Given Recent Cylinder Velocities. *Mathematical Problems in Engineering*, 2011.

MIT (2007). MIT VIV Data Repository. `http://web.mit.edu/towtank/www/vivdr/datasets.html`.

Morison, J., Johnson, J., and Schaaf, S. (1950). The Force Exerted by Surface Waves on Piles. *Journal of Petroleum Technology*, 2(05):149–154.

Mukundan, H. (2008). *Vortex-Induced Vibration of Marine Risers: Motion and Force Reconstruction from Field and Experimental Data*. PhD thesis, Massachusetts Institute of Technology.

Oakley, O. and Spencer, D. (2004). Deepstar High Reynolds Number Cylinder Test Program. In *Proceedings of Deep Offshore Technology Conference*, volume 4.

Raaijmakers, R. and Battjes, J. (1997). An Experimental Verification of Huse's Model on the Calculation of Mooring Line Damping. In *Proceedings of the 8th BOSS Conference: Behaviour of Offshore Structures*, volume 2, pages 439–452.

Ran, Z. (2000). *Coupled Dynamic Analysis of Floating Structures in Waves and Currents*. PhD thesis, Texas A&M University College Station, TX.

Santillan, S. and Virgin, L. (2011). Numerical and Experimental Analysis of the Static Behavior of Highly Deformed Risers. *Ocean Engineering*, 38(13):1397–1402.

Schewe, G. (1983). On the Force Fluctuations Acting on a Circular Cylinder in Crossflow from Subcritical up to Transcritical Reynolds Numbers. *Journal of fluid mechanics*, 133:265–285.

Shu, S., Seehausen, R., Bledsoe, S., and Powell, T. (2010). Reviewing the State of Deepwater Production Risers. *Offshore*, 70(11).

Sidarta, D. E., Finn, L. D., and Maher, J. (2010). Time Domain FEA for Riser VIV Analysis. In *ASME 2010 29th International Conference on Ocean, Offshore and Arctic Engineering*, pages 793–806. American Society of Mechanical Engineers.

Spencer, D., Yin, H., and Qiu, W. (2007). Development and Verification of a Time-Domain VIV Simulation Tool. In *Proceedings of the 3rd International Workshop on Applied Offshore Hydrodynamics, Rio de Janeiro, Brazil*.

Strouhal, V. (1878). Ueber eine besondere Art der Tonerregung. *Annalen der Physik und Chemie*, 5(10):216–251.

Sumer, B. M. and Fredsøe, J. (1997). *Hydrodynamics Around Cylindrical Structures.* Number 12 in Advanced Series on Ocean Engineering. World Scientific.

Thorsen, M. J., Sævik, S., and Larsen, C. M. (2014). A Simplified Method for Time Domain Simulation of Cross-Flow Vortex-Induced Vibrations. *Journal of Fluids and Structures*, 49:135–148.

Triantafyllou, G. (1998). Vortex Induced Vibrations of Long Cylindrical Structures. In *Proceedings of 1998 ASME Fluids Engineering Division Summer Meeting (FEDSM98). Washington, D.C.*

Triantafyllou, M., Triantafyllou, G., Tein, Y., and Ambrose, B. D. (1999). Pragmatic Riser VIV Analysis. In *Proceedings of Offshore technology conference.* Offshore Technology Conference.

Vandiver, K. and Li, L. (1994). SHEAR7 Program Theoretical Manual. *Department of Ocean Engineering, Massachusetts Institute of Technology.*

Venugopal, M. (1996). *Damping and Response Prediction of a Flexible Cylinder in a Current.* PhD thesis, Massachusetts Institute of Technology.

Williamson, C. and Roshko, A. (1988). Vortex Formation in the Wake of an Oscillating Cylinder. *Journal of fluids and structures*, 2(4):355–381.

Xue, H., Wang, K., and Tang, W. (2015). A Practical Approach to Predicting Cross-Flow and In-Line VIV Response for Deepwater Risers. *Applied Ocean Research*, 52:92–101.

Yin, H. (2007). Nonlinear Analysis of Mooring Lines and Marine Risers. Master's thesis, Memorial University of Newfoundland.

# Appendices

# Appendix A

# Mathematical Formulation

This Appendix provides the mathematical modelling of the time-domain finite element program to predict the statics and dynamics of slender marine structures. The global-coordinate-based, nonlinear finite element method was employed based on the Euler-Bernoulli beam model. More details can be found in the work of Yin (2007).

## A.1  Governing Equations

Figure A.1 illustrates the 3-D coordinate system employed in this study. The *xoy* plane overlaps with the calm free surface with the *z*-axis pointing upwards. The centerline, representing a slender rod, is defined by a position vector $\mathbf{r}(s,t)$, where $s$ is arc length and $t$ is time.

The unit tangent vector, the principal normal vector, and the bi-normal vector can be described as $\mathbf{r}'$, $\mathbf{r}''$, and $\mathbf{r}' \times \mathbf{r}''$, respectively, where the primes denote the partial derivative with respect to $s$. Therefore based on the momentum conservation, the equations of motion for a unit arc length segment of a slender rod can be expressed as:

$$\mathbf{F}' + \mathbf{q} = \rho\ddot{\mathbf{r}} \tag{A.1}$$
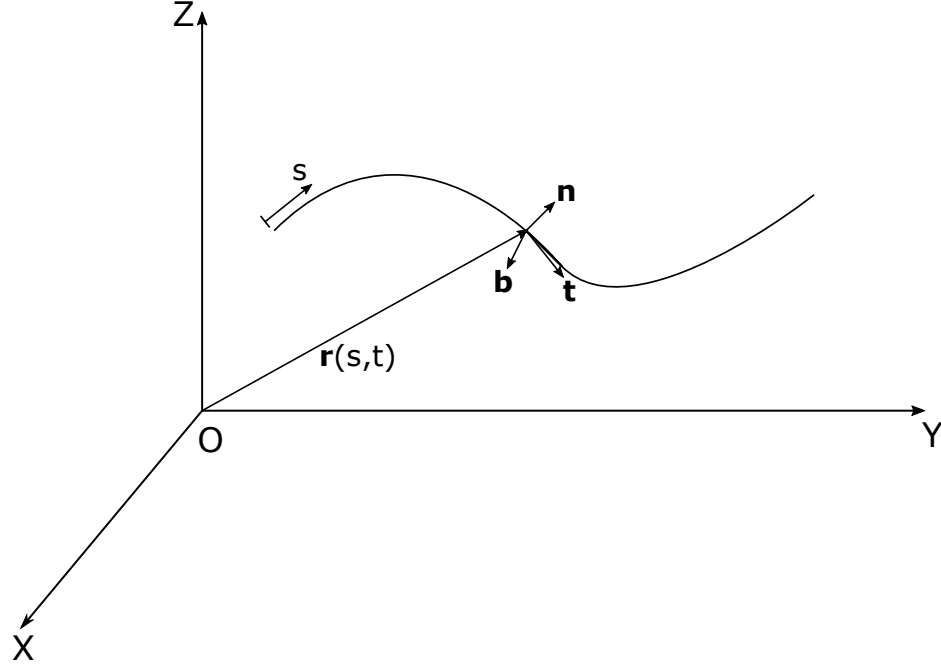
Figure A.1: A slender rod in the global coordinate system

$$\mathbf{M}' + \mathbf{r}' \times \mathbf{F} + \mathbf{m} = \mathbf{0} \tag{A.2}$$

where $\mathbf{F}$ is the resultant force, $\mathbf{M}$ is the resultant moment acting along the centerline, $\mathbf{q}$ is the applied force per unit length, $\rho$ is the mass per unit length of the rod, $\mathbf{m}$ is the applied moment per unit length, and the overdots indicate the differentiation with respect to time.

According to the Bernoulli-Euler beam theory, the bending moment is proportional to the curvature and acts along the bi-normal direction for an elastic rod with equal principal stiffness. Thus the resultant moment can be expressed as:

$$\mathbf{M} = \mathbf{r}' \times EI\mathbf{r}'' + H\mathbf{r}' \tag{A.3}$$

where $EI$ is the bending stiffness and $H$ is the torque. By substituting Equation A.3

into Equation A.2 we obtain:

$$(\mathbf{r}' \times EI\mathbf{r}'' + H\mathbf{r}')' + \mathbf{r}' \times \mathbf{F} + \mathbf{m} = \mathbf{0} \tag{A.4}$$

$$\mathbf{r}' \times (EI\mathbf{r}'')' + \mathbf{r}'' \times EI\mathbf{r}'' + H'\mathbf{r}' + H\mathbf{r}'' + \mathbf{r}' \times \mathbf{F} + \mathbf{m} = \mathbf{0} \tag{A.5}$$

By using the cross-product distributive law over addition and by applying $\mathbf{r}'' \times EI\mathbf{r}'' = 0$ we have:

$$\mathbf{r}' \times [(EI\mathbf{r}'')' + \mathbf{F}] + H'\mathbf{r}' + H\mathbf{r}'' + \mathbf{m} = \mathbf{0} \tag{A.6}$$

Taking the scalar product of Equation A.6 and $\mathbf{r}'$ yields:

$$\mathbf{r}' \cdot \mathbf{r}' \times [(EI\mathbf{r}'')' + \mathbf{F}] + \mathbf{r}' \cdot H'\mathbf{r}' + \mathbf{r}' \cdot H\mathbf{r}'' + \mathbf{r}' \cdot \mathbf{m} = \mathbf{0} \tag{A.7}$$

Note that $\mathbf{r}' \cdot \mathbf{r}' \times [(EI\mathbf{r}'')' + \mathbf{F}] = 0$, $\mathbf{r}' \cdot H\mathbf{r}'' + 0$, and $\mathbf{r}' \cdot \mathbf{r}' = 1$, hence Equation A.7 can be simplified as:

$$H' + \mathbf{r}' \cdot \mathbf{m} = \mathbf{0} \tag{A.8}$$

Since most slender marine structures have circular cross sections, we may assume that there would be no distributed torsional moment $\mathbf{r}' \cdot \mathbf{m}$ caused by hydrodynamic loads. Thus, according to Equation A.8, $H$ is independent of arc length $s$. In addition, the torques along the lines are generally so small that they may be neglected, indicating that both $H$ and $\mathbf{m}$ are zero. Hence, Equation A.6 can be further reduced to:

$$\mathbf{r}' \times [(EI\mathbf{r}'')' + \mathbf{F}] = \mathbf{0} \tag{A.9}$$

Equation A.9 indicates that the vector $(EI\mathbf{r}'')' + \mathbf{F}$ is tangent to the centerline of

the rod. By introducing a scalar function $\lambda(s,t)$, Equation A.9 can be rewritten as:

$$(EI\mathbf{r}'')' + \mathbf{F} = \lambda\mathbf{r}' \tag{A.10}$$

The scalar product of Equation A.10 and $\mathbf{r}'$ is:

$$\lambda = (EI\mathbf{r}'')' \cdot \mathbf{r}' + \mathbf{F} \cdot \mathbf{r}' \tag{A.11}$$

Assuming the bending stiffness $EI$ does not vary with arc length, and by applying $\mathbf{r}''' \cdot \mathbf{r}' = (\mathbf{r}'' \cdot \mathbf{r}')' - \mathbf{r}'' \cdot \mathbf{r}'' = 0 - \kappa^2 = -\kappa^2$, we can reduce Equation A.11 to:

$$\lambda = T - EI\kappa^2 \tag{A.12}$$

where $T$ is the tension in the rod segment and $\kappa$ is the curvature of the centerline.

Substituting Equation A.10 into Equation A.1 gives the governing equation of motion of the rod segment:

$$-(EI\mathbf{r}'')'' + (\lambda\mathbf{r}')' + \mathbf{q} = \rho\ddot{\mathbf{r}} \tag{A.13}$$

Meanwhile, $\mathbf{r}$ must satisfy the inextensibility condition:

$$\mathbf{r}' \cdot \mathbf{r}' = 1 \tag{A.14}$$

If the rod is considered stretchable and the stretch is linear and small, Equation A.14 can be approximated by:

$$\mathbf{r}' \cdot \mathbf{r}' = (1 + \epsilon)^2 \approx 1 + 2\epsilon = 1 + 2\frac{T}{EA} \tag{A.15}$$

$$\frac{1}{2}(\mathbf{r}' \cdot \mathbf{r}' - 1) = \frac{T}{EA} \approx \frac{\lambda}{EA} \tag{A.16}$$

where the scalar function $\lambda$ is the Lagrangian multiplier constrained by the small elongation condition, the strain $\epsilon$ must be small in order to validate Equation A.12 and Equation A.15, and $EA$ is the axial stiffness.

The distributed load $\mathbf{q}$ on the rod consists of the self weight, as well as the hydrostatic and hydrodynamic loads from the ambient fluid, therefore

$$\mathbf{q} = \mathbf{w} + \mathbf{F}^s + \mathbf{F}^d \tag{A.17}$$

where $\mathbf{w}$ is the rod weight per unit length, $\mathbf{F}^s$ is the hydrostatic load per unit length, and , $\mathbf{F}^d$ is the hydrodynamic load per unit length.

The hydrostatic load can be expressed as:

$$\mathbf{F}^s = \mathbf{B} + (P_s A \mathbf{r}')' \tag{A.18}$$

where $\mathbf{B}$ is the buoyancy force per unit length of the rod, $P_s$ is the hydrostatic pressure at rod position $\mathbf{r}$, and the term $(P_s A \mathbf{r}')'$ invokes the pressure gradient between the two ends.

Morrison's equation is employed in approximating the hydrodynamic loads on the slender rod:

$$\begin{aligned} \mathbf{F}^d &= -C_A \ddot{\mathbf{r}}^n + C_M \dot{\mathbf{V}}^n + C_D |\mathbf{V}^n_{rel}| \mathbf{V}^n_{rel} \\ &= -C_A \ddot{\mathbf{r}}^n + \tilde{\mathbf{F}}^n \end{aligned} \tag{A.19}$$

where $C_A$ is the added mass per unit length, $C_M$ is the inertia force per unit length per unit normal acceleration, and $C_D$ is the drag force per unit length per unit normal velocity, $\dot{\mathbf{V}}^n$ is the fluid acceleration and velocity normal to the centerline of the rod, and $\mathbf{V}^n_{rel}$ is the relative fluid velocity normal to the centerline of the rod. Assuming

that the presence of the rod does not perturb the fluid domain, we can compute $\dot{\mathbf{V}}^n$ and $\mathbf{V}^n_{rel}$ by:

$$\dot{\mathbf{V}}^n = \dot{\mathbf{V}} - (\dot{\mathbf{V}} \cdot \mathbf{r}')\,\mathbf{r}' \tag{A.20}$$

$$\mathbf{V}^n_{rel} = (\mathbf{V} - \dot{\mathbf{r}}) - [(\mathbf{V} - \dot{\mathbf{r}}) \cdot \mathbf{r}']\,\mathbf{r}' \tag{A.21}$$

where $\mathbf{V}$ and $\dot{\mathbf{V}}$ are the absolute velocity and acceleration of the water particles, respectively.

The normal velocity and acceleration of the rod, $\dot{\mathbf{r}}^n$ and $\ddot{\mathbf{r}}^n$, can be obtained by deducting the tangent components from the total vectors:

$$\dot{\mathbf{r}}^n = \dot{\mathbf{r}} - (\dot{\mathbf{r}} \cdot \mathbf{r}') \cdot \mathbf{r}' \tag{A.22}$$

$$\ddot{\mathbf{r}}^n = \ddot{\mathbf{r}} - (\ddot{\mathbf{r}} \cdot \mathbf{r}') \cdot \mathbf{r}' \tag{A.23}$$

The rod equation of motion in vector form can be obtained by combining Equation A.13, Equation A.17, Equation A.18, and Equation A.19:

$$\rho\ddot{\mathbf{r}} + C_A\ddot{\mathbf{r}}^n + (EI\mathbf{r}'')'' - (\tilde{\lambda}\mathbf{r}')' = \tilde{\mathbf{w}} + \tilde{\mathbf{F}}^d \tag{A.24}$$

where

$$\tilde{\mathbf{w}} = \mathbf{w} + \mathbf{B} \tag{A.25}$$

$$\tilde{\lambda} = \lambda + P_sA \tag{A.26}$$

Substituting $\lambda = T - EI\kappa^2$ into Equation A.26 yields:

$$\tilde{\lambda} = (T + P_sA) - EI\kappa^2 = \tilde{T} - EI\kappa^2 \tag{A.27}$$

## A.2  Finite Element Formulation

The dependent variables, $\mathbf{r}(s,t)$ and $\lambda(s,t)$, can be determined by solving Equation A.13 and Equation A.16 in combination with initial and boundary conditions. By rewriting Equation A.24 and Equation A.16 in Einstein notation, we can obtain:

$$-\rho \ddot{r}_i - C_A \ddot{r}_i{}^n - (EIr_i'')'' + (\tilde{\lambda}r_i')' + \tilde{\omega}_i + \tilde{F}_i^d = 0 \tag{A.28}$$

$$\frac{1}{2}(r_n' r_n' - 1) - \frac{\lambda}{EA} = \frac{1}{2}(r_n' r_n' - 1) - \frac{\tilde{\lambda} - P_s A}{EA} = 0 \tag{A.29}$$

where the subscripts range from 1 to 3 for the 3-D problem. This results in a set of 12 second-order partial differential equations and 3 algebraic equations. In order to solve the system of equations numerically, a finite element scheme has been employed, which is given below.

The variables, $r_i(s,t)$ and $\tilde{\lambda}(s,t)$, along an element length of $L$ may be approximated by:

$$r_i(s,t) = A_k(s)U_{ik}(t) \qquad i = 1,2,3, \quad k = 1,2,3,4 \tag{A.30}$$

$$\tilde{\lambda}(s,t) = P_m(s)\tilde{\lambda}_m(t) \qquad m = 1,2,3 \tag{A.31}$$

where $A_k$ and $P_m$ are the shape functions, $U_{ik}$ and $\tilde{\lambda}_m$ are the coefficients to be determined, and $0 \leq s \leq L$.

By applying Galerkin's method to obtain the weak form of Equation A.28 over the element length, we have:

$$\int_0^L \delta r_i[-\rho \ddot{r}_i - C_A \ddot{r}_i{}^n - (EIr_i'')'' + (\tilde{\lambda}r_i')' + \tilde{w}_i + \tilde{F}_i^d]ds = 0 \tag{A.32}$$

Since $\delta r_i$ and $\delta U_{il}(t)$ are arbitrary, Equation A.32 becomes:

$$\delta U_{il}(t) \int_0^L A_l[-\rho \ddot{r}_i - C_A \ddot{r}_i^n - (EIr_i'')'' + (\tilde{\lambda} r_i')' + \tilde{w}_i + \tilde{F}_i^d]ds = 0 \qquad (A.33)$$

$$\int_0^L A_l[-\rho \ddot{r}_i - C_A \ddot{r}_i^n - (EIr_i'')'' + (\tilde{\lambda} r_i')' + \tilde{w}_i + \tilde{F}_i^d]ds = 0 \qquad (A.34)$$

Integrating the terms in Equation A.34 by parts yields:

$$\int_0^L [A_l(\rho \ddot{r}_i + C_A \ddot{r}_i^n) + A_l'' EIr_i'' + A_l' \tilde{\lambda} r_i' - A_l(\tilde{w}_i + \tilde{F}_i^d)]ds$$
$$= EIr_i'' A_l'|_0^L + [\tilde{\lambda} r_i' - (EIr_i'')']A_l|_0^L \qquad (A.35)$$

The two terms on the RHS of Equation A.35 represent the natural boundary conditions of an element. After assembling the elemental equations, all internal moments and forces will cancel out with those of the adjacent elements except the two at both ends of the global line. These two boundary conditions will be dictated by the global boundary conditions applied at the anchor and the fairlead.

Since the highest order of the derivative on $\mathbf{r}$ is *third* in Equation A.35, the interpolating function should be thrice differentiable. In addition, the highest order of the derivatives is *second* inside the integral. Hence, the overall approximation of $\mathbf{r}$ should be $C^1$-continuous. Based on these requirements, the Hermite cubic shape functions have been used in interpolating $\mathbf{r}$. Meanwhile, the $C^0$-continuous quadratic Lagrangian shape functions have been selected in $\tilde{\lambda}$ interpolation.

The coefficients, $U_{ik}$ and $\tilde{\lambda}_m$, and the shape functions, $A_k$ and $P_m$, are defined as:

$$
\begin{aligned}
U_{i1} &= r_i(0,t) & U_{i2} &= Lr_i'(0,t) \\
U_{i3} &= r_i(L,t) & U_{i4} &= Lr_i'(L,t) \\
\tilde{\lambda}_1 &= \tilde{\lambda}(0,t) & \tilde{\lambda}_2 &= \tilde{\lambda}(\frac{L}{2},t) & \tilde{\lambda}_3 &= \tilde{\lambda}(L,t)
\end{aligned}
\qquad (A.36)
$$

$$
\begin{aligned}
A_1 &= 1 - 3\xi^2 + 2\xi^3 \\
A_2 &= \xi - 2\xi^2 + \xi^3 \\
A_3 &= 3\xi^2 - 2\xi^3 \\
A_4 &= -\xi^2 + \xi^3 \\
P_1 &= 1 - 3\xi + 2\xi^2 \\
P_2 &= 4\xi(1 - \xi) \\
P_3 &= \xi(2\xi - 1)
\end{aligned}
\tag{A.37}
$$

where $\xi = s/L$.

Equation A.36 denotes the physical meanings of the elemental quantities to be determined, i.e. the deflections, the slopes, and the effective line tensions at both ends and the effective line tension at the midpoint of an element.

By substituting Equation A.30 and Equation A.31 into Equation A.35 and integrating the equation term by term, we can obtain the following discretized form of the elemental equation of motion:

$$
(M_{ijlk} + M_{ijlk}^a)\ddot{U}_{jk} + (K_{ijlk}^1 + \tilde{\lambda}_n K_{nijlk}^2)U_{jk} - F_{il} = 0
\tag{A.38}
$$

where

$$
M_{ijlk} = \int_0^L \rho A_l A_k \delta_{ij} ds
\tag{A.39}
$$

$$
M_{ijlk}^a = C_A\left[ \int_0^L A_l A_k \delta_{ij} ds - \left( \int_0^L A_l A_k A_s' A_t' ds \right) U_{it} U_{js} \right]
\tag{A.40}
$$

$$
K_{ijlk}^1 = \int_0^L EI A_l'' A_k'' \delta_{ij} ds
\tag{A.41}
$$

$$
K_{nijlk}^2 = \int_0^L P_n A_l' A_k' \delta_{ij} ds
\tag{A.42}
$$

$$
F_{il} = \int_0^L A_l(\tilde{w}_i + \tilde{F}_i^d) ds
\tag{A.43}
$$

where $\delta_{ij}$ is the Kronecker delta function, and the subscripts $i, j = 1, 2, 3$, and $l, k, s, t = 1, 2, 3, 4$. Note that the elemental natural boundary conditions (the RHS of Equation A.35) are not included in Equation A.38.

Similarly, applying Galerkin's method to the stretch condition Equation A.16 yields:

$$\int_0^L P_m[\frac{1}{2}(r'_n r'_n - 1) - \frac{\tilde{\lambda} - P_s A}{EA}]ds = 0 \tag{A.44}$$

where hydrostatic pressure, $P_s$, can be approximated by interpolating pressures at both ends and the midpoint of the element using shape functions that are the same to $P_m$ in Equation A.37:

$$P_s = P_t P_{st}, \qquad t = 1, 2, 3 \tag{A.45}$$

Combining approximating relations Equation A.30, Equation A.31, and Equation A.45 with Equation A.44 leads to:

$$G_m = A_{mil} U_{kl} U_{ki} - B_m - C_{mt} \tilde{\lambda}_t + C_{mt} A P_{st} = 0 \tag{A.46}$$

where

$$A_{mil} = \frac{1}{2} \int_0^L P_m A'_i A'_l ds \tag{A.47}$$

$$B_m = \frac{1}{2} \int_0^L P_m ds \tag{A.48}$$

$$C_{mt} = \frac{1}{EA} \int_0^L P_m P_t ds \tag{A.49}$$

where the subscripts $k, m, t = 1, 2, 3$, and $i, l = 1, 2, 3, 4$.

## A.3   Static Analysis Procedure

The inertia term in Equation A.38 is neglected in static analysis. Therefore, the governing equations of rod become:

$$R_{il} = (K^1_{ijlk} + \tilde{\lambda}_n K^2_{nijlk})U_{jk} - F_{il} = 0 \tag{A.50}$$

$$G_m = A_{mil}U_{kl}U_{ki} - B_m - C_{mt}\tilde{\lambda}_t + C_{mt}AP_{st} = 0 \tag{A.51}$$

where $F_{il}$ includes all static forces such as gravity, the drag load due to the steady current, and other applied static forces on the line.

The iterative Newton's method is employed to solve the nonlinear equations. By expanding Equation A.50 and Equation A.51 about an assumed solution or the solution from the current $n$th iteration into Taylor series and neglecting the higher order terms, we get:

$$R^{(n+1)}_{il} = R^{(n)}_{il} + \frac{\partial R_{il}}{\partial U_{jk}}(\Delta U_{jk}) + \frac{\partial R_{il}}{\partial \tilde{\lambda}_n}(\Delta \tilde{\lambda}_n) = 0 \tag{A.52}$$

$$G^{(n+1)}_{m} = G^{(n)}_{m} + \frac{\partial G_m}{\partial U_{jk}}(\Delta U_{jk}) + \frac{\partial G_m}{\partial \tilde{\lambda}_n}(\Delta \tilde{\lambda}_n) = 0 \tag{A.53}$$

which can be expressed in a matrix form as:

$$\begin{pmatrix} K^{t0(n)}_{ijlk} & K^{t1(n)}_{iln} \\ D^{t0(n)}_{mjk} + D^{t0(n)}_{mt} & D^{t1(n)}_{mn} \end{pmatrix} \left\{ \begin{matrix} \Delta U_{jk} \\ \Delta \tilde{\lambda}_n \end{matrix} \right\} = \left\{ \begin{matrix} -R^{(n)}_{il} \\ -G^{(n)}_{m} \end{matrix} \right\} \tag{A.54}$$

where

$$\frac{\partial R_{il}}{\partial U_{jk}} = K^{t0(n)}_{ijlk} = K^1_{ijlk} + \tilde{\lambda}^{(n)}_n K^2_{nijlk} \tag{A.55}$$

$$\frac{\partial R_{il}}{\partial \tilde{\lambda}_n} = K^{t1(n)}_{iln} = K^2_{nijlk}U^{(n)}_{jk} \tag{A.56}$$

$$D_{mjk}^{t0(n)} = \int_0^L P_m A_k' A_q' ds U_{jq}^{(n)} \tag{A.57}$$

$$D_{mt}^{t0(n)} = \frac{\partial}{\partial U_{jk}}(C_{mt} A P_{st}^{(n)}) \tag{A.58}$$

$$D_{mn}^{t1(n)} = \int_0^L (-\frac{1}{EA} P_m P_n) ds \tag{A.59}$$

$$R_{il}^{(n)} = (K_{ijlk}^1 + \tilde{\lambda}_n^{(n)} K_{nijlk}^2) U_{jk}^{(n)} - F_{il} \tag{A.60}$$

$$G_m^{(n)} = A_{mil} U_{kl}^{(n)} U_{ki}^{(n)} - B_m - C_{mt} \tilde{\lambda}_t^{(n)} + C_{mt} A P_{st}^{(n)} \tag{A.61}$$

where the ranges of the subscripts are:

$$i, j, m, n, r, t = 1, 2, 3, \qquad l, k, p, q = 1, 2, 3, 4$$

There are 15 linear algebraic equations for each element at each iteration; however, the subscript arrangement in the above equations is inconvenient for a numerical solution. In order to overcome this, the order of the state variables $U_{il}$ and $\tilde{\lambda}_m$ is rearranged as:

$$\text{DOF of } U_{il} = \begin{bmatrix} 1 & 2 & 9 & 10 \\ 3 & 4 & 11 & 12 \\ 5 & 6 & 13 & 14 \end{bmatrix} \qquad \text{for } i = 1, 2, 3 \quad l = 1, 2, 3, 4$$

$$\text{DOF of } \tilde{\lambda}_m = \begin{bmatrix} 7 & 8 & 15 \end{bmatrix} \qquad \text{for } m = 1, 2, 3 \tag{A.62}$$

Equation A.54 at the $n$th iteration can be expressed as:

$$[K^{(n)}]\{\Delta y\} = \{F^{(n)}\} \tag{A.63}$$

where $K^{(n)}$ is the stiffness matrix, $\{y\}$ contains the degrees-of-freedom of an element:

$$\{y\} = [U_{11}, U_{12}, U_{21}, U_{22}, U_{31}, U_{32}, \tilde{\lambda}_1, \tilde{\lambda}_2, U_{13}, U_{14}, U_{23}, U_{24}, U_{33}, U_{34}, \tilde{\lambda}_3]^T \qquad \text{(A.64)}$$

and the symbol $\Delta$ refers to taking the difference between two consecutive iterations. $F^{(n)}$ is the force vector:

$$\{F^{(n)}\} = [ -R_{11}^{(n)}, -R_{12}^{(n)}, -R_{21}^{(n)}, -R_{22}^{(n)}, -R_{31}^{(n)}, -R_{32}^{(n)}, -G_1^{(n)}, -G_2^{(n)}, -R_{13}^{(n)}, -R_{14}^{(n)},$$
$$-R_{23}^{(n)}, -R_{24}^{(n)}, -R_{33}^{(n)}, -R_{34}^{(n)}, -G_3^{(n)}]^T$$

$$\text{(A.65)}$$

The locations of the stiffness coefficients in matrix $K^{(n)}$ can be determined based on the aforementioned rearrangements. For example, the term $K_{1234}^{t0}$ in Equation A.54 ($i = 1, l = 3, j = 2, k = 4$) is located at row 9 and column 12 in $K^{(n)}$, and $K_{231}^{t1}$ ($i = 2, l = 3, n = 1$) is located at row 11 and column 7 in $K^{(n)}$.

The global stiffness matrix is assembled from the anchor node to the fairlead node in an ascending order. This assembling process leads to a system of $8 \times (N + 1) - 1$ equations, where $N$ is the number of total elements in the line. By reducing the global stiffness matrix to a banded matrix with a bandwidth of 29, the system of equations Equation A.63 can be efficiently solved by Gaussian elimination with back substitution. The state variables are then updated by $y^{(n+1)} = y^{(n)} + \Delta y$ and are used to re-evaluate $K^{(n+1)}$ and $F^{(n+1)}$ for solving $\Delta y$ again. This iterative procedure continues until $\Delta y$ is smaller than a user-defined tolerance.

## A.4 Dynamic Analysis Procedure

In dynamic analysis, the governing equations, Equation A.38 and Equation A.46, are integrated in time-domain. Equation A.38 can be rewritten in the following form:

$$\hat{M}_{ijlk}\ddot{U}_{jk} = -(K^1_{ijlk} + \tilde{\lambda}_n K^2_{nijlk})U_{jk} + F_{il} \tag{A.66}$$

$$= -F^1_{il} - F^2_{il} + -F_{il} = \hat{F}_{il}$$

where

$$\hat{M}_{ijlk} = M_{ijlk} + M^a_{ijlk} \tag{A.67}$$

The second-order differential equation, Equation A.66, can be converted to a system of two first-order differential equations:

$$\dot{U}_{jk} = V_{jk} \tag{A.68}$$

$$\hat{M}_{ijlk}\dot{V}_{jk} = \hat{F}_{il} \tag{A.69}$$

In order to integrate Equation A.68 from $(n)$th to $(n+1)$th time step, a combined second-order explicit-implicit integration scheme is employed. The mass term, $\hat{M}_{ijlk}$, and the applied external load term, $F_{il}$, are integrated based on the second-order Adams-Bashforth method, while the terms $U_{jk}$, $F^1_{il}$, and $F^2_{il}$ are integrated by the second-order Adams-Moulton scheme.

The term $G_m^{(n+1)}$ in the small stretch condition, Equation A.46, can be approximated by the first-order Taylor series expansion at $n$th time step:

$$0 = 2G_m^{(n+1)} \approx 2G_m^{(n)} + 2\frac{\partial G_m^{(n)}}{\partial U_{jk}}\Delta U_{jk} + 2\frac{\partial G_m^{(n)}}{\partial \tilde{\lambda}_n}\Delta \tilde{\lambda}_n$$

$$= 2G_m^{(n)} + 2K^2_{mijlk}U_{il}\Delta U_{jk} + 2D^{t1(n)}_{mn}\Delta \tilde{\lambda}_n \tag{A.70}$$

Consequently, Equation A.38 and Equation A.70 can be expressed in a matrix form similar to that formulated in static analysis:

$$\begin{pmatrix} \hat{K}_{ijlk}^{t0(n)} & \hat{K}_{iln}^{t1(n)} \\ \hat{D}_{mjk}^{t0(n)} & \hat{D}_{mn}^{t1(n)} \end{pmatrix} \begin{Bmatrix} \Delta U_{jk} \\ \Delta \tilde{\lambda}_n \end{Bmatrix} = \begin{Bmatrix} \hat{R}_{il}^{(n)} \\ \hat{G}_m^{(n)} \end{Bmatrix} \tag{A.71}$$

where

$$\Delta U_{jk} = U_{jk}^{(n+1)} - U_{jk}^{(n)} \tag{A.72}$$

$$\Delta \tilde{\lambda}_n = \tilde{\lambda}_n^{(n+\frac{1}{2})} - \tilde{\lambda}_n^{(n-\frac{1}{2})} \tag{A.73}$$

$$\tilde{\lambda}_n^{(n-\frac{1}{2})} = \frac{1}{2}(\tilde{\lambda}_n^{(n)} + \tilde{\lambda}_n^{(n-1)}) \tag{A.74}$$

$$\hat{K}_{ijlk}^{t0(n)} = \frac{2}{\Delta t^2}(3\hat{M}_{ijlk}^{(n)} - \hat{M}_{ijlk}^{(n-1)}) + K_{ijlk}^1 + \tilde{\lambda}_n^{(n-\frac{1}{2})} K_{nijlk}^2 \tag{A.75}$$

$$\hat{K}_{iln}^{t1(n)} = 2K_{nijlk}^2 U_{jk}^{(n)} \tag{A.76}$$

$$\hat{D}_{mjk}^{t0(n)} = 2K_{mijlk}^2 U_{il} \tag{A.77}$$

$$\hat{D}_{mn}^{t1(n)} = 2D_{mn}^{t1(n)} \tag{A.78}$$

$$\hat{R}_{il}^{(n)} = \frac{2}{\Delta t}(3\hat{M}_{ijlk}^{(n)} - \hat{M}_{ijlk}^{(n-1)}) + (3F_{il}^{(n)} - F_{il}^{(n-1)}) - 2K_{ijlk}^1 U_{jk}^{(n)} - 2\tilde{\lambda}_n^{(n-\frac{1}{2})} K_{nijlk}^2 U_{jk}^{(n)} \tag{A.79}$$

$$\hat{G}_m^{(n)} = -2G_m^{(n)} \tag{A.80}$$

where the superscripts refer to time steps and the ranges of the subscripts are:

$$i, j, m, n = 1, 2, 3, \qquad l, k = 1, 2, 3, 4$$

The degrees-of-freedom of the state variables of an element are rearranged and solved based on the same rules as those employed in static analysis, namely Equa-

tion A.62 and Equation A.64, together with Equation A.81 and Equation A.82 below:

$$[\hat{K}^{(n)}]\{\Delta y\} = \{\hat{F}^{(n)}\} \tag{A.81}$$

where $\hat{K}^{(n)}$ is the global stiffness matrix in dynamic analysis, and the global force vector in dynamic analysis $\hat{F}^{(n)}$ is:

$$
\begin{aligned}
\{\hat{F}^{(n)}\} = [&\hat{R}_{11}^{(n)}, \ \hat{R}_{12}^{(n)}, \ \hat{R}_{21}^{(n)}, \ \hat{R}_{22}^{(n)}, \ \hat{R}_{31}^{(n)}, \ \hat{R}_{32}^{(n)}, \ \hat{G}_{1}^{(n)}, \ \hat{G}_{2}^{(n)}, \ \hat{R}_{13}^{(n)}, \ \hat{R}_{14}^{(n)}, \\
&\hat{R}_{23}^{(n)}, \ \hat{R}_{24}^{(n)}, \ \hat{R}_{33}^{(n)}, \ \hat{R}_{34}^{(n)}, \ \hat{G}_{3}^{(n)}]^{T}
\end{aligned}
\tag{A.82}
$$

## A.5 Boundary Conditions

Note that so far the RHS of Equation A.35, the elemental natural boundary conditions, in the static and dynamic formulations has not been dealt with. During the assemblage of all elements, the internal natural boundary conditions vanish except the two end nodes of the global line, which will be determined from global boundary conditions. Under different scenarios, both ends of the line in each of the three dimensions can be clamped, free, elastically supported, or applied with concentrated loads. These boundary conditions can be modelled as the connections to linear translational and rotational springs with different stiffness to be included in the static and dynamic analyses. The generalized global stiffness matrix, $K^{(n)}$, the vector of degrees-of-freedom, $\Delta y$, and the generalized vector of forces, $F^{(n)}$, in Equation A.63 may have to be modified according to different global boundary conditions at both ends of the line.

### Clamped End

For an end clamped in a certain direction, the essential boundary conditions, namely the deflection and the slope in that direction, are both zero.

In the program, the anchor node is numbered as the first node of the first element in the line. Therefore, the anchor point fixed in $x$-direction indicates that $\Delta y(1)$ and $\Delta y(2)$ are zero. This can be achieved by resetting all the stiffness coefficients in the first and second row and column of $K^{(n)}$ to zero and by resetting $F^{(n)}(1)$ and $F^{(n)}(2)$ to zero. Then the stiffness coefficients $K^{(n)}(1,15)$ and $K^{(n)}(2,15)$ (banded global stiffness matrix) in static analysis and the stiffness coefficients $K^{(n)}(1,1)$ and $K^{(n)}(2,2)$ (full square global stiffness matrix) in dynamic analysis are reset to one, respectively.

**Free End**

If an end node is free along one axis, then the nodal natural boundary conditions in that direction are prescribed as zero. Since the elemental natural boundary conditions are excluded from the static and dynamic formulations, no modification is required on $K^{(n)}$, $\Delta y$, or $F^{(n)}$ in Equation A.63 for both analyses.

**Hinged End**

For an end hinged in one direction, the deflection and the moment at that end in the same direction will be zero.

Compare a hinged end to its fixed counterpart. If the anchor point becomes hinged along the $x$-axis, then the stiffness coefficients in the first row and the first column of $K^{(n)}$ are prescribed as zero, and $F^{(n)}(1)$ is constrained to zero as well. In addition, $K^{(n)}(1,15)$ in static analysis and $K^{(n)}(1,1)$ in dynamic analysis are reset to one.

**Elastically-Supported End**

If the end is supported on linear springs, translational and/or rotational, in certain directions, then $K^{(n)}$, $\Delta y$, $F^{(n)}$ in Equation A.63 will be modified by the spring

restoring forces and/or moments, which are functions of the corresponding degrees-of-freedom.

For instance, if the anchor node is attached to a linear translational spring with a stiffness of $K_{spring}$ along the $x$-direction. Therefore in static analysis, Equation A.52, establishing the relationship between the difference of the degree-of-freedom $U_{11}$ and the reaction force $-R_{11}$, will be rewritten as:

$$\frac{\partial \check{R}_{11}}{\partial U_{jk}}(\Delta U_{11}) + \frac{\partial \check{R}_{11}}{\partial \tilde{\lambda}_n}(\Delta \tilde{\lambda}_n) = -\check{R}_{11}^{(n)} \tag{A.83}$$

where

$$\frac{\partial \check{R}_{11}}{\partial U_{jk}} = K_{1111}^{t0(n)} + K_{spring} \tag{A.84}$$

$$\check{R}_{11}^{(n)} = R_{11}^{(n)} - K_{spring} \cdot [U_{11} - Refanchor(1)] \tag{A.85}$$

and the vector $Refanchor(3)$ stores the $x$, $y$, and $z$ coordinates of the anchor position where the spring is at its original length.

In dynamic analysis, since the spring forces and/or moments are considered as external forces and/or moments, they are integrated from $n$th to $(n+1)$th time step by the second-order Adams-Bashforth scheme:

$$\begin{aligned}
\int_{t^{(n)}}^{t^{(n+1)}} F_{spring} dt &= \int_{t^{(n)}}^{t^{(n+1)}} K_{spring} \cdot [U_{11} - Refanchor(1)] dt \\
&\approx \frac{\Delta t}{2} K_{spring} \cdot 3[U_{11}^{(n)} - Refanchor(1)] - [U_{11}^{(n-1)} - Refanchor(1)] \\
&= \frac{\Delta t}{2} K_{spring} \cdot [\Delta U_{11}^{(n)} + 2U_{11}^{(n)} - 2Refanchor(1)] \tag{A.86}
\end{aligned}$$

where $\Delta U_{11}^{(n)}$ is the known difference of the degree-of-freedom between the $n$th and $(n-1)$th time steps. The last two terms in the brackets of Equation A.86 remain on the RHS to modify $-R_{11}^{(n)}$. $\frac{\Delta t}{2}$ will be cancelled out during arithmetic manipulation,

and the superscripts refer to time step.

**End Node Under Concentrated Loads**

For an end node under a known concentrated force or moment (may vary with time but not with the state variables), the load is incorporated into $-R_{il}^{(n)}$ in Equation A.60 at the $n$th iteration in static analysis. It is then integrated by the second-order Adams-Moulton method and added to $\hat{R}_{il}^{(n)}$ in Equation A.79 at the $n$th time step in dynamic analysis.

**End Element Under Distributed Loads**

A distributed force or moment applied along the end elements can be dealt with similarly to the wet weight $\tilde{w}_i$ and the hydrodynamic force $\tilde{F}_i^d$ in the term $F_{il}$ in Equation A.38. This implies that the distributed loads are multiplied by the shape functions $A_l$ and integrated over the element length $L$. Sequentially, the loads are integrated by the second-order Adams-Moulton scheme since the loads are known at all time steps.

**Sea Bottom**

The sea bottom was assumed to be flat, elastic, and impenetrable in the program. The sea floor was modelled as a linear spring carpet in static analysis and as a distributed linear spring-damper system in dynamic analysis. The distributed spring support force in the vertical direction can be described as:

$$q^{spring} = \begin{cases} \dfrac{w}{R}\{R - (r_3 - Z_{btm})\}, & \text{if } R - (r_3 - Z_{btm}) > 0 \\[2mm] 0, & \text{if } R - (r_3 - Z_{btm}) \leqslant 0 \end{cases} \tag{A.87}$$

where $w$ is the wet weight per unit length of the line, $R$ is the outer diameter, $r_3$ represents the $z$-coordinates of all nodes, and $Z_{btm}$ is the $z$-coordinate of the sea

bottom.

The sea floor support force was included in the line equation of motion in a way similar to that of an end element under distributed loads, namely:

$$\int_0^L q^{spring} A_l(s)ds = \mu_{lm}\{\frac{w}{R}(R + Z_{btm})\}|_m - \gamma_{lkm}U_{3k}\{\frac{w}{R}\}|_m \qquad \text{(A.88)}$$

where

$$\mu_{lm} = L \int_{\xi_1}^{\xi_2} A_l P_m ds \qquad \text{(A.89)}$$

$$\gamma_{lkm} = L \int_{\xi_1}^{\xi_2} A_l A_k P_m ds \qquad \text{(A.90)}$$

and the integration bounds of nondimensional arc length, $0 \leqslant \xi_1 < \xi_2 \leqslant 1$, represent the portion of the line element that contacts the sea floor.

In dynamic analysis, the sea floor friction was modelled as a distributed linear damper system:

$$q^{damper} = \begin{cases} C_f\mu_f\dfrac{r'}{|r'|}, & \text{if } R - (r_3 - Z_{btm}) > 0 \\ \\ 0, & \text{if } R - (r_3 - Z_{btm}) \leqslant 0 \end{cases} \qquad \text{(A.91)}$$

where

$$C_f = \begin{cases} -1, & \text{if } V_t > C_V \\ \\ -\dfrac{V_t}{C_V}, & \text{if } V_t \leqslant C_V \\ \\ 1, & \text{if } V_t < C_V \end{cases} \qquad \text{(A.92)}$$

where $V_t$ is the tangent velocity of the line, $C_V$ is the tolerance of the tangent velocity, and $\mu_f$ is the dynamic friction coefficient of the sea bottom.

Therefore in dynamic analysis, the term resulted from the dynamic friction of the

sea floor was added to the RHS of Equation A.66

$$\int_0^L q^{spring} A_l(s)ds = \mu_{lm}C_f\mu_f\{w\frac{r'}{|r'|}\}|_m \tag{A.93}$$

The coefficients, $\mu_{lm}$ and $\gamma_{lkm}$, for elements around the touch down point vary with time because of the sea floor boundary condition. Thus, $\mu_{lm}$ and $\gamma_{lkm}$ were evaluated at every time step for the portion of the element that lies on the sea bottom.

# Appendix B

# Bilinear Interpolation of The DeepStar Database

Figure B.1 illustrates one interpolation grid, $ABCD$, on a 2-D Cartesian plane. Given four known function values, $f(x_1, y_1)$, $f(x_2, y_1)$, $f(x_2, y_2)$, and $f(x_1, y_2)$, at four tabulated data points, $A$, $B$, $C$, and $D$, the objective is to find the bilinearly-interpolated function value, $f(x, y)$, at the point $P$.

The function values, $f(x, y_1)$ and $f(x, y_2)$, at the intermediate points, $Q_1$ and $Q_2$, are first approximated by:

$$
\begin{aligned}
f(x, y_1) &\approx \frac{x_2 - x}{x_2 - x_1} f(x_1, y_1) + \frac{x - x_1}{x_2 - x_1} f(x_2, y_1) \\
f(x, y_1) &\approx \frac{x_2 - x}{x_2 - x_1} f(x_1, y_2) + \frac{x - x_1}{x_2 - x_1} f(x_2, y_2)
\end{aligned}
\tag{B.1}
$$

The value $f(x, y)$ at the point $P$ is then interpolated by:

$$
f(x, y) \approx \frac{y_2 - y}{y_2 - y_1} f(x, y_1) + \frac{y - y_1}{y_2 - y_1} f(x, y_2)
\tag{B.2}
$$

where $f(x, y_1)$ and $f(x, y_2)$ are plugged in from Equation B.1.
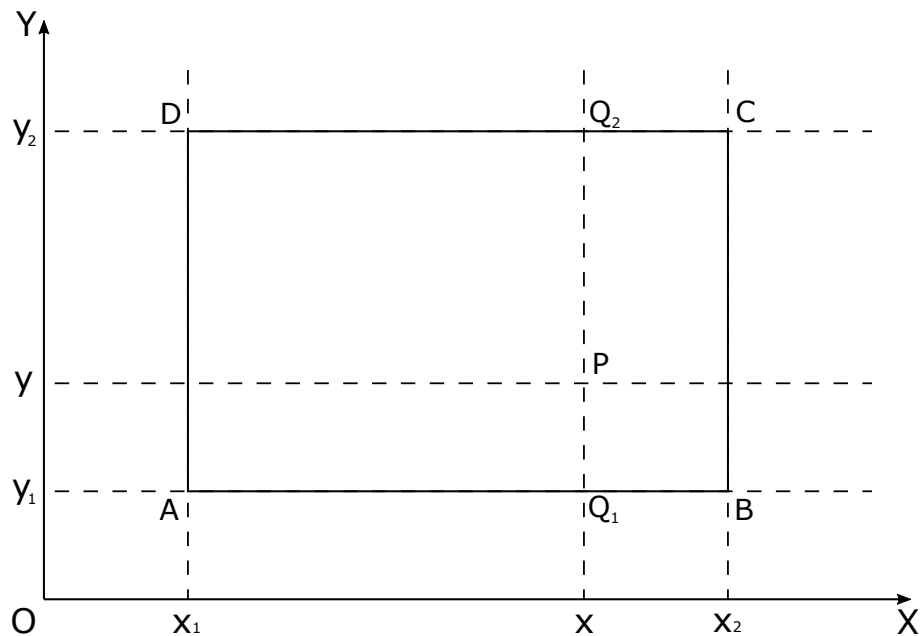
Figure B.1: Bilinear interpolation grid

In the case of interpolating the DeepStar database, the $OX$-axis represents the state variable, $V_r$, while the $OY$-direction stands for the state variable, $A^*$. After the state variables are obtained from the zero up-crossing analysis of the last VIV cycle, a searching algorithm will determine the grid on which the point $(A^*, V_r)$ is located. The hydrodynamic coefficients for the current VIV cycle are then approximated by calling the bilinear interpolation subroutine.